Growth and Modeling of ZnO and the Characterization of Epitaxial Thin Films by means of Synchrotron Radiation

A Comprehensive Study of Synthesis, Characterization and Modeling of Selected Model Structures

Michael Getz B. Sc.

Master Thesis at the Department of Chemistry under the Program: Materials, Energy and Nanotechnology

UNIVERSITY OF OSLO

May 30th 2012

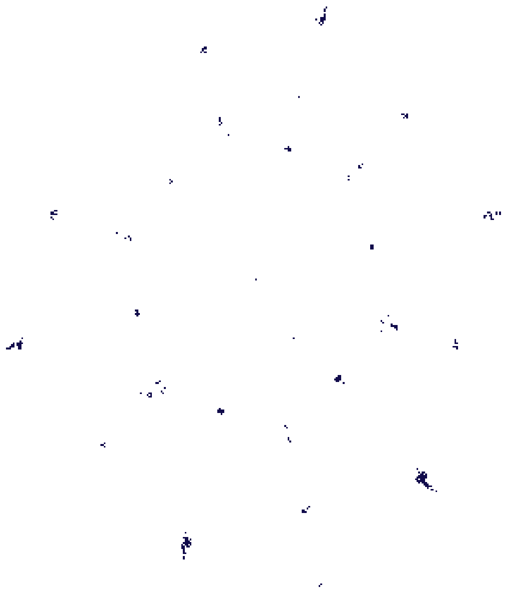

2012

Growth and Modeling of ZnO and the Characterization of Epitaxial Thin Films by means of Synchrotron Radiation – *A Comprehensive Study of Synthesis and Characterization and Modeling of Selected Model Structures*

Michael Getz B. Sc.

http://www.duo.uio.no/

Trykk: Reprosentralen, Universitetet i Oslo

Abstract

ZnO is a promising material that recently attracts wide interest due its outstanding properties that make it suitable for applications in short wavelength optoelectronic devices as well as high temperature electronics. Producing pure large single crystals of ZnO is however very difficult. This study presents successful growth of up to 3 mm ZnO single crystals, grown by the chemical vapour transport method and the characterization of these crystals, using optical microscopy, X-ray diffraction and scanning electron microscopy.

The polar (0001) and (000-1) surfaces of ZnO in oxygen and zinc rich atmospheres have also been thoroughly investigated using *ab initio* calculations to predict the structures for varying coverage of oxygen and zinc on the two different surfaces.

Finally, a method for characterizing nanometer sized thin films using a six-axis goniometer at the BM01A beam line at the ESRF in France has also been developed. The goniometer allows for high flexibility, which is useful for thin film characterization. By mounting the thin film sample like a single crystal and using X-rays with low incident angles, it has been possible to reproduce previously obtained information about the selected samples, although in more detail and in a more efficient manner, due to the high brilliance X-rays available at the synchrotron, and the large area CCD-detector accessible at the beam line.

Details about the experimental setup as well as results for a model system, a Co_3O_4 thin film on a α-Al_2O_3 substrate, will be presented among other systems of interest. Various substrates used for thin film deposition and their suitability for SXRD characterization has also been investigated, proving for instance that the phonon scattering in silicon results in broad diffuse scattering that overshadows thin film reflections and consequently complicates characterization of thin films.

Preface

This master thesis has been produced at the Inorganic Chemistry section of the Department of Chemistry at the University of Oslo, under the supervision of Helmer Fjellvåg and Ola Nilsen. The work was started in January 2011 and ended in May 2012.

The work covers synthesis, modeling and characterization of various model systems, and may be considered to consist of three main parts, although everything is related to some degree. There will consequently be a separation between these where it is deemed natural.

I wish to thank my supervisors Helmer Fjellvåg and Ola Nilsen for giving me the opportunity and means to carry out this study and for letting me work with the things that interest me the most. I wish to thank Ola Nilsen in particular for revising the thesis, and pointing out possible improvements. I also want to thank Ponniah Vasjeeston for the time he spent teaching me to use Material Studios and for helping with the DFT calculations, and also the staff at SNBL for their help with the experiments, and in particular Dmitry Chernyshov for his assistance with both development of the thin film setup and with analyzing the obtained results. Special thanks goes to my friends Henrik Sønsteby and Petter Simonsen for making the time spent on this work so enjoyable, and Henrik Sønsteby in particular for the many fruitful scientific discussions in addition to the great collaboration during the time spent in Grenoble and with the transport experiments, and Petter Simonsen for many interesting discussions about DFT and ZnO.

Finally I wish to thank my family for supporting me and giving me the means to commit myself fully to studying and following the path I want, and my better part Marit Norderhaug for being there for me when I needed it and continuously believing in me.

Blindern, May 2012

Michael Getz

Abbreviations

AFM – Atomic Force Microscope

ALD – Atomic Layer Deposition

APS – Advanced Photon Source

BM – Bending Magnet

CCD – Charge-Coupled Device

CTR – Crystal Truncation Rod

CVT – Chemical Vapour Deposition

DND – Double Numerical plus *d*-function

ESRF – European Synchrotron Radiation Facility

ESEM – Environmental Scanning Electron Microscopy

ETD – Everheart-Thornley Detector

fcc – face centered cubic

FWHM – Full Width at Half Maximum

GGA – General Gradient Approximation

GISAXS – Gracing Incidence Small Angle X-ray Scattering

hcp – hexagonal close packed

LCAO – Linear Combination of Atomic Orbitals

LDA – Local Density Approximation

LFD – Large Field Detector

LSD (LSDA) – Local Spin Density Approximation

MD – Molecular Dynamics

ML – Monolayer

PBE – Perdew Burke Ernzerhof

PW – Plane Waves

PW91 – Perdew Wang 1991

RGA – Residual Gas Analyzer

SEM – Scanning Electron Microscope

SNBL – Swiss Norwegian Beam Lines

SSD – Solid State Detector

SXRD – Synchrotron X-Ray Diffraction

TCO – Transparent Conducting Oxide

TF-theory – Thomas Fermi-theory

XPS – X-ray Photoelectron Spectroscopy

XRD – X-Ray Diffraction

XRF – X-ray Fluorescence

Table of Contents

1 Introduction

Since the invention of the first semiconductor transistor in 1947, the semiconductor industry has grown at incredible pace. Even though the first semiconductor transistor was made from germanium, silicon became the material of choice due to better stability at higher temperatures. This is also the reason why silicon is preferred over GaAs, which has a direct band gap and better electron transport and optical properties than silicon and would result in extremely fast devices. In many ways silicon is a poor choice of transistor, but the lack of a good substitute makes it persist even today. In order to advance semiconductor technology further, investigation of alternative materials and their growth and processing techniques is essential.

Zinc oxide has a large direct band gap which makes it transparent for visible light, in addition to high electron mobility, that makes it suitable for high power and high temperature electronic devices as well as short wavelength optoelectronics (*1*). It already shows promising applications within the solar cell industry, thin film transistors, light emitting diodes and biosensors, and is probably the material which will replace the highly expensive indium tin oxide as a transparent conducting oxide (TCO) for all flat screen electronic devices. There is however, a lot about ZnO that remains to be understood in order to develop applications further; in particular better understanding of the surface as well as various interfaces could lead to ground breaking discoveries. One such interesting interface is the one between ZnS and ZnO, especially with respect to solar cells. Producing sufficiently large and chemically pure single crystal substrates of ZnO in an efficient way still remains a challenge. The melting point of ZnO is close to 2000 °C, and thus obtaining crystals by methods like liquid phase epitaxy is exceedingly demanding (*2*). Hydrothermal methods may be used in order to avoid this problem; however the synthesis requires the use of a KOH/LiOH mineralizer in order to increase the solubility of ZnO in water (*3*). This, in turn, causes ZnO substrates grown by this method to contain large amounts of Li and K impurities, which segregate to the surface and make epitaxial growth difficult.

Chemical vapour transport (CVT) is a method that in theory should produce exceptionally pure single crystals of both ZnO and ZnS at reasonable temperatures, but the process is fairly slow and it can take up to several months to produce sufficient sized single crystals (*4*).

Studying the surfaces and interfaces of ZnO and ZnS can be done in numerous ways. At the Swiss-Norwegian Beam Lines (SNBL) at the European Synchrotron Radiation Facility (ESRF) in Grenoble, it is possible to do X-ray diffraction using a synchrotron light source. The combination of very high intensity and resolution which only X-rays can provide can be used to study surface and interfaces. At the SNBL however, the focus is primarily on single crystal diffraction, and to do this they use a flexible six-axis goniometer. This should make it possible to develop a setup in which it is possible to get diffraction from very few nanometres of film, and with the right software this could be used to find growth directions, texture of the film surface, or be used to characterize nanosized domains in the film, as well as fine details about the crystallinity. Most of this information can be obtained using other techniques like transmission electron microscopy (TEM), though the possibility for *in-situ* experiments in addition to the unmatched resolution available at the synchrotron, opens up a wide range of possibilities that are impossible with other techniques that either require vacuum or have other limitations. The minimal amount of sample preparation needed in addition to the fact that the technique is non-destructive for inorganic samples is also a great benefit. Developing a well functioning setup for studying thin films at a synchrotron, could thus have a significant impact on the thin film community and could contribute with understanding the growth of epitaxial thin films on various substrates.

In order to obtain a better understanding of surfaces, as well as what to expect when characterizing them, calculations can be a great asset. The polar Zn-terminated (0001) and O-terminated (000-1) faces are two of the most common face terminations of wurtzite ZnO and are known to have a slightly different electronic structure, which leads to different physical and chemical properties. As previously reported in detail for GaN, polarity is one of the most important factors for film growth, impurity incorporation, and device performance (*5*), and this, in addition to the ZnO(0001) and ZnO(000-1) being among the most common face terminations, is the motivation to study exactly these surfaces. Analyzing both surfaces in the presence of oxygen and zinc atmospheres is of interest and could show possible surface or interface structures when depositing ZnO on the surface, and can also be used to understand the growth of ZnO under these conditions. The most important condition for epitaxial growth has previously been found to be the surface structure of the substrate and how this matched the structure of the deposited thin film (*6*). While a ZnO crystal has a lot of other face terminations that also could be of interest with respect to growth, the calculations done in this study are purely focused on the ZnO(0001) and ZnO(000-1) faces.

1.1 Motivation, Goals and Methods

The use of thin films deposited on a bulk material has resulted in a long range of applications, with examples being Cr coatings used on plastic parts for automobiles in order to impart hardness, metallic luster and protection against ultraviolet light, or TiN coatings on cutting or drilling tools to offer hardness and low friction. By using thin films, it is often possible to achieve the same functionality as a bulk material, but at a significantly reduced cost and weight (*7*). In order to reduce costs and improve properties and functionality of thin film devices, the understanding of the growth process and which methods produce the best films is essential. This is the underlying motivation for growing substrates for thin film deposition, studying the polar surfaces of ZnO and for developing a technique for analyzing thin films by means of synchrotron X-ray diffraction.

The goal of this study has hence been to grow high quality single crystals substrates of ZnO and ZnS, with main focus on ZnO, using the chemical vapour transport reactions. Another goal has been to use density functional theory to analyze the polar surfaces of ZnO in vacuum, oxygen and zinc atmospheres in order to find possible surface structures at various coverages of these adsorbates. The most important goal has been to establish collaboration with the SNBL, in order to find a way to routinely analyze thin films in the future using synchrotron radiation, and to do measurements on epitaxial thin films grown by the Inorganic Chemistry group at the University of Oslo.

2 Theory

This chapter will give the theoretical insight needed in order to understand the methods used and the results obtained in this study. The theory of transport reactions, synchrotron radiation and *ab initio* calculations will be thoroughly explained and relevant information about surface chemistry as well as each characterization technique used in this study will be addressed. The chapter will begin with a presentation of the most important materials in this study.

2.1 Properties of ZnO and ZnS

ZnO crystallizes in the wurtzite crystal structure (Figure 1) at ambient conditions and belongs to the space group $P6_3mc$, which is characterized by two interconnecting sub lattices of Zn^{2+} and O^{2-} (*1*). Each Zn ion is tetrahedrally coordinated to the O ions and vice-versa. The tetrahedral coordination gives rise to polar symmetry along the hexagonal axis which is responsible for the piezoelectric properties of ZnO as well as *spontaneous polarization*[1]*(8)*. Cutting the crystal perpendicular to the *c* axis always results in a Zn terminated (0001) surface on one side of the crystal and an O terminated (000-1) surface on the other. These polar surfaces have different physical and chemical properties (*9*). The tetrahedral coordination of the compound also suggests covalent sp^3 hybridization. The bonding between zinc and oxygen however, is largely ionic, and thus ZnO lies on the borderline of being classified as a covalent and ionic compound.

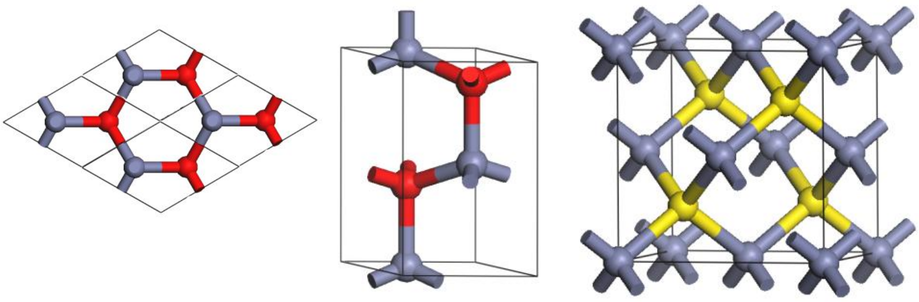

Figure 1: The wurtzite structure of ZnO (left and middle) and the zinc blende structure of ZnS (right). The O atoms are red, while the S atoms are yellow.

---

[1] Spontaneous polarization is an effect that amplifies any initial bias in spin polarization, so that the electrons of an atom spontaneously change into either of two spin polarized states (parallel or anti parallel to an applied magnetic field.

ZnO can also crystallize in the cubic zinc blende type structure, but this phase is only stable when grown on a cubic substrate. ZnS could be such a substrate as it crystallizes in the zinc blende (also known as sphalerite) structure type at ambient conditions (right in Figure 1). Both ZnO and ZnS are wide band gap materials with band gaps of 3.4 (*1*) and 3.68 (*10*) respectively. This makes them transparent to visible light. By doping ZnO or ZnS with group III elements like In^{3+}, Al^{3+} or Ga^{3+}, both may exhibit *n*-type conductivity as these dopants act as donors by substituting for Zn^{2+} (*11*). They retain their transparency after the doping and consequently they are therefore called transparent conducting oxides (TCO). In addition, the large *refractive index*[2] of ZnO and ZnS (2.00 (*12*) and 2.57 (*13*) respectively), make them suitable for antireflective coatings on solar cells and light emitting diodes.

The lattice parameters of hexagonal ZnO are a = 3.2465 Å and c = 5.2030 Å (*14*), while cubic ZnS has a lattice constant of a = 5.4040 Å (*15*).

2.2 Chemical Vapour Transport (CVT)

Chemical vapour transport (CVT) is a method for growing crystals that has proven to be a reliable way to synthesize high quality single crystals even below the melting or sublimation point (*16*). The technique, which is also found in nature was first discovered by Schäfer (*17*), and can be used to produce oxides as well as most of the chalcogenides and pnictides and is also used for purification and determination of thermodynamic properties.

The basic principles of the technique lie in the volatilization of a material which reacts with a gaseous species at a certain temperature T_1 in order to produce a low-volatile chemical intermediate. This intermediate diffuses to an area with temperature T_2 and decomposes back into the starting materials due to the temperature dependence of the chemical equilibrium involved (*4*).

The typical way to do this is to place either a sealed or open ampoule in a furnace with a temperature gradient. The ampoule is either filled with a gas that works as a transport agent, or contains some highly volatile powder, which will undergo sublimation before the experiment temperature is reached. The polycrystalline starting material is placed in one end

---

[2] The refractive index is a dimensionless number that describes how electromagnetic radiation propagates through a specific medium.

of the ampoule and will then be heated to a temperature T_1 together with the transport agent and react to form a new chemical intermediate. This unstable intermediate will travel to other end of the ampoule to a temperature T_2 and decompose back to the starting materials. By properly adjusting the temperature gradient, it is possible to avoid nucleation at the growing seeds and create large single crystals. In general a transport reaction can be written as:

$$A(s) + B(g) \Leftrightarrow AB(g) \qquad \text{Eq. 1}$$

A solid A reacts with a gas B at a certain temperature T_1 and forms the gas AB. The gas then diffuses to an area with temperature T_2 and decomposes back to A and B. An example can be seen in Figure 2.

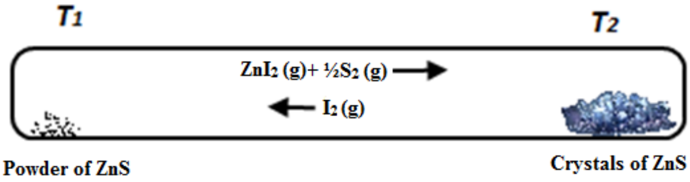

Figure 2: The principle behind chemical vapour transport explained with the ZnS as an example. Powder of ZnS reacts with I_2 and gets transported to the area with a temperature T_2.

2.2.1 Physical Chemistry of Transport Reactions

To understand the physical chemistry of transport reactions, a system with one solid and one or more gaseous component and with all components in chemical equilibrium with each other is considered. If there is a small perturbation from the chemical equilibrium at a certain place in the system, so that the solid would have smaller free energy in this area, it would migrate to this place via the gas phase until equilibrium is established again. The simplest way to cause local perturbations on a system is by imposing a temperature gradient (*4*). By examining a simple case with four components, which in general applies to the transport of metal chalcogenides by halogens, the following equilibrium is considered:

$$ZnS\,(s) + I_2\,(g) \leftrightarrow ZnI_2\,(g) + \tfrac{1}{2}S_2\,(g). \qquad \text{Eq. 2}$$

The easiest way to experimentally do a transport experiment, is to use a sealed ampoule with the polycrystalline feed material, like ZnS, together with some small amount of I_2 for transport in one end. If the source end of the ampoule is kept at 1000°C and the other at 750°C, ZnS will be transported via the vapour phase and deposit at the cold end due to the temperature dependence of the reaction above. The I_2 is not spent in the process, but will diffuse back to the hot end and react with more ZnS and continue the transport until all ZnS has been transported over to the colder end. Thus a tiny amount of transport agent is enough to transport practically unlimited amounts of solid (*4*).

There are several parameters that govern a transport reaction. Most important is the chemical potential difference $\Delta\mu$ between the source and the sink, which is a function of the temperatures at these respective locations i.e. T_1 and T_2, as well as the change in free energy ΔG and the concentration of the transporter C_T. For practical purposes the sign of the heat ΔH is important as it can be used to indicate whether the transport will go from hot to cold or vice versa. More specifically we can find the direction of transport by looking at the Gibbs equation at chemical equilibrium, i.e. $\Delta G = 0$.

$$\Delta G_0 = \Delta H_0 - T\Delta S_0 = -RT \ln K, \qquad \text{Eq. 3}$$

where R is the universal gas constant, ΔH_0 is the standard enthalpy, ΔS_0 is the standard entropy and K is the equilibrium constant. The following can be derived using Eq. 3 (Appendix I).

$$\left[\frac{\partial \ln K}{\partial T}\right] = \frac{\Delta H_0}{RT^2} \qquad \text{Eq. 4}$$

The equation implies that transport will go from hot to cold if $\Delta H > 0$, i.e. for endothermic reactions where K increases with temperature, while for $\Delta H < 0$ the reaction will go from cold to hot (*4*).

An additional important factor is the equilibrium constant. By plotting the change in chemical potential against the change in enthalpy with entropy change ΔS as a parameter, Schäfer found that for a transport reaction to take place, the equilibrium constant needs to be in the order of unity, i.e. $K \approx 1$(*17*). It is when the equilibrium constant is at this value that the change in partial pressure of the involved species will exhibit the largest effect, and small changes in partial pressure will consequently result in large changes in the equilibrium constant. If there is no change in partial pressure, there can be no transport; however a large change in partial pressure may result in efficiently grown crystals. With too high growth rates the crystal quality will however be poor, and thus an evaluation of growth rates against crystal quality needs to be considered when deciding on the temperature gradient of the experiment.

The mechanism for conducting the gas from one end of the tube to the other has a large impact on the efficiency of the transport. Transport by diffusion only is slow, and can happen if the tube is narrow and if the pressure inside the tube is low. At higher pressures convection will be the method of transport; however with too much convection in the tube, the transport will also be slow as the transported material could get transported back again before it has time to decompose back to the starting materials and instead gets circulated in the tube. If the reaction involves a change in mole numbers, and if the reaction rate at both sides is fast enough to maintain a constant pressure inside the tube, the mechanism for transport will be laminar flow[3]. Which mechanism it will be, depends mainly on the concentration of the transport agent and the geometry of the tube as these have direct impact on the pressure. In most cases though, there is usually an overlap between all these mechanisms and determining the exact mechanism at each temperature along the temperature gradient is very complicated.

2.2.2 The Growth of Crystals by CVT

Transport reactions in general yield polycrystalline materials consisting of intergrown crystallites (*4*). In order to obtain the highest quality crystals, the transported mass must be carefully controlled. If the transport is too fast, the growing crystal cannot accommodate all the incoming atoms and supersaturation will increase until additional nucleation takes place and the crystal quality becomes poor. Controlling how much mass is transported is done by changing the temperature difference. By lowering ΔT, the transport velocity will decrease, however crystal growth will be very slow if kept at the initial optimal temperature difference for the duration of the experiment. For optimal growth rates, the temperature difference should be increased as the crystal grows, as the surface area of the crystal becomes larger and will be able to digest more feed material.

In order to acquire as pure crystals as possible, the choice of transport agent is important. In principle it may be chosen from thermodynamic data; however some transport agents will also be able to transport certain impurities. By choosing the correct transport agent it’s possible to avoid the impurities that have the most impact on the crystal. The transport agent itself will most likely also create defects in the structure, for this reason it is common to use transporters with larger size than the transported atoms so that they don’t fit well into the

---

[3] The gas flow is purely parallel to the tube walls.

crystal structure. Halogens are thus ideal transporters for most metals as they are both large and volatile.

2.3 Surface Chemistry

The termination of a crystal, i.e. the formation of a surface causes a deviation from the perfect periodicity of the bulk, which in turn changes the electronic structure of at the surface. This sometimes gives rise to very complicated surface structures that often are difficult to describe. W. Pauli had a popular saying that he used on several occasions:

> *"God made solids, but surfaces were the work of Devil!"*

Working with surfaces is quite messy as there are all sorts of atoms that may adsorb and cause changes to the properties and growth of the surface. Knowing the surface of a material is however important in order to understand how it will react or to understand its catalytic properties, as all reactions begin at the surface. In addition the growth of the material depends a lot on the surface structure and the thermodynamics at the surface.

As surfaces structures can be considered as being two dimensional, the number of possible Bravais lattices is reduced from the fourteen possible Bravais lattices in three dimensions to only the five Bravais lattices shown in Figure 3. Note that an actual surface rarely is two dimensional and that the atoms do not need to be in the plane of the unit cell.

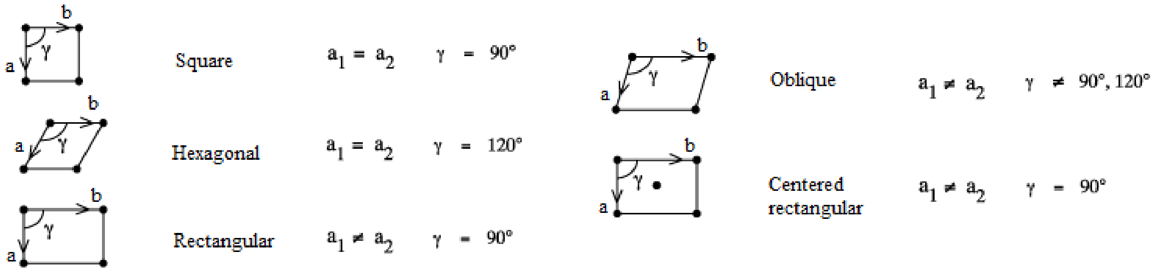

Figure 3: The two dimensional Bravais lattices

Atoms at a surface have lower coordination than in the bulk and thus are usually less stable. In order to compensate for this, the surface relaxes, i.e. the bond length between the first and second layer decreases due to higher bond order. The distance between the second and third on the other hand often expands in order to compensate the contraction between the first layers. Surface crystallographic studies have shown that virtually all surfaces relax in vacuum

(*18*). The effect is weaker for close packed structures, but still generates several layers into the bulk. A similar effect can be seen when growing epitaxial thin films, as the first layer will usually have lattice constants that are slightly strained in order to adapt to the substrate lattice. If the difference in lattice constants is too large, the film will however not be able grow epitaxially. A relevant example is the growth of GaN which is difficult as there are few hexagonal substrates to grow on (*19*). ZnO however is an ideal substrate as the lattice mismatch between these two compounds is only 1.8 % and the first layers of GaN will thus have a slight increase in lattice constants before they gradually return to their bulk values as more layers are grown. After enough layers are grown, the substrate may be removed, although for solar cell applications for instance, it might be useful to keep it and grow other compounds like $In_{1-x}Ga_xN$ on top of GaN again in order to create a multilayered solar cell that can be used to absorb other wavelengths.

For covalent structures, the loss of nearest neighbors at the surface is difficult to compensate and this usually results in an atomic structure that is fundamentally different from the structure one would expect if the bulk structure terminated abruptly at the surface. This is called surface reconstruction, and can lead to very complicated surface structures. In order to name the surface structure, a specific notation is used. If the two dimensional projection of the unit cell of the bulk and the unit cell of the surface is identical, the surface structure is referred to as a (1×1) and is called a *substrate structure*. The substrate structure on the (111) surface on platinum is thus designated Pt(111)-(1×1). The (111) refers to the Miller indices (*hkl)* of this surface, which are defined as the reciprocal value of where a crystal plane intercepts the main crystallographic axis of the solid. In this way it is thus possible to uniquely define any crystallographic surface.

If a surface structure if formed in the presence of an adsorbed gas and is characterized by a unit cell, which is identical to the unit cell of the substrate, the surface structure is denoted (1×1)-S, where S is the chemical symbol or formula for the adsorbate.

The surface structures are frequently characterized by unit cells that are integral multiples of the substrate unit cell. If the vectors that span the surface unit cell are twice as large as the bulk cell, it is designated (2×2). The unit cell may also be rotated compared to the substrate cell. If every other lattice site on a square is unique, then a $p(\sqrt{2} \times \sqrt{2})R45^\circ$ structure is formed (Figure 4), where *p* stands for primitive, which means that this is the simplest unit cell it is possible to use in order to describe the structure. In most cases this is taken for granted and the *p* is usually left out, however in this case, the structure can be denoted as *c*(2×2), where *c* stands for *centered*, as it can be viewed as a (2×2) surface structure with an extra atom in its centre. If it is possible to describe a surface structure without rotating it relative to the substrate, this is usually preferred, even if it no longer has a primitive unit cell. This notation thus is able to cover quite a range of different surface structures as long as it is in the registry of the substrate unit cell. When the dimensions of the surface until cell is not an integer multiple of the bulk unit cell, the notation is not easily applicable and can not be used to describe the cell. This is usually only observed at high coverages for weakly adsorbing adsorbates as the adsorbate-adsorbate interactions become of the same magnitude as the adsorbate-substrate interactions and thus the substrate structure has less impact on the surface structure.

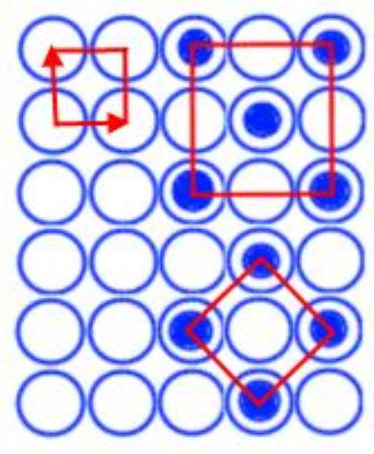

Figure 4: The *fcc*(100)-*p*(√2 × √2)*R*45° surface structure with corresponding unit cell shown to the bottom right. Top left shows the unit cell of the underlying bulk, while top right shows the alternative unit cell of the surface called *fcc*(100)-*c*(2 × 2).

2.4 Characterization Techniques

2.4.1 X-Ray Diffraction (XRD)

In order to see things that are smaller than the wavelength of visible light, electromagnetic radiation with higher energies are needed. For diffraction studies, only wavelengths in the range of a few angstroms are used as this wavelength is comparable to the size of atoms. Electromagnetic radiation with this wave length are called X-rays and have typical photon energies in the range of 100 eV – 120 KeV, however only the short wavelength X-rays, called hard X-rays, are used for diffraction experiments as these are ideal for probing the structural arrangement of atoms and molecules in most materials.

X-rays are generally produced either by X-ray tubes or synchrotron radiation (will be treated separately in chapter 2.4.2). In X-ray tubes the X-rays are generated by accelerating electrons from a heated filament across a high voltage field and bombard a metal anode, typically copper or molybdenum (*20*). When electrons from the beam collide with the solid, they are slowed down and this loss in energy results in radiation called *Bremsstrahlung* radiation. In addition some of the electrons with high energy will knock out inner shell electrons in atoms, which will cause an ionization process in which an X-ray photon with a characteristic energy of the material is emitted.

The produced X-rays can be focused down on a sample and the X-rays will interact with the electrons of the atoms in the sample. When X-ray photons collide with electrons, some of them will be deflected away from their original path, just like a billiard ball bouncing off another. If the wavelength of X-rays that were scattered remains unchanged, i.e. the X-ray photon did not lose any energy; the process is elastic and is called *Thompson Scattering (21)*. These are the X-rays that are measured in diffraction experiments, as they are characteristic for each chemical compound and carry information about the electronic distribution in the material. Not all the scattering processes are elastic however, and inelastic scattering processes are called *Compton Scattering*, which will appear as noise in the resulting intensity distribution.

If the atoms in the sample are arranged in a periodic fashion, as in crystals, the diffracted waves will consist of sharp interference maxima with the same symmetry as in the distribution of atoms. The resulting diffraction pattern thus makes it possible to deduce the atomic distances in the material. Amorphous materials on the other hand have little or no apparent periodicity and will scatter X-rays randomly with no evident peaks in the resulting intensity distribution.

Bragg's Law

The reason why the peaks in the diffraction pattern are related the atomic distances can be shown by considering an incident X-ray beam interacting with atoms arranged in a periodic manner as shown in Figure 5 (*22*).

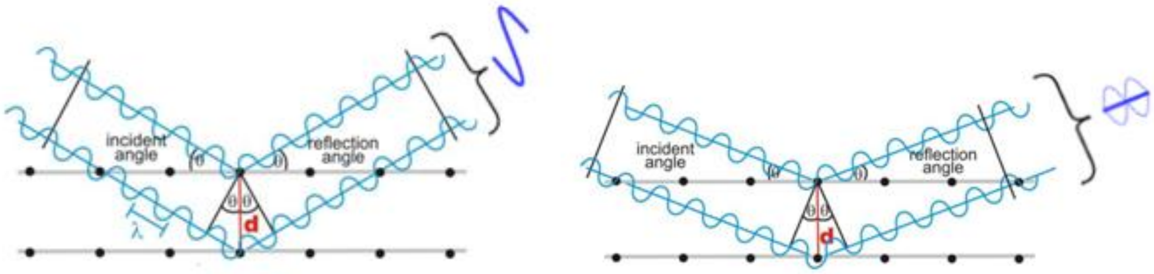

Figure 5: Left image shows constructive interference of reflected waves, while right shows destructive interference. This is the principle behind Bragg's law (*22*).

The atoms are represented by the black spheres in the figure and can be viewed as forming different sets of planes in the crystal. Depending on which direction the crystal is viewed from, there will be different planes perpendicular to the viewing direction and the distance *d* between certain planes is a characteristic trait of the material. The left side of Figure 5 shows the condition for diffraction. By looking at the additional distance the lower incident X-ray with wavelength λ, and with a scattering angle of θ must travel compared to the upper one in order to achieve constructive interference, a general condition for diffraction can be found using simple geometry:

$$2dsin\theta = n\lambda. \qquad \text{Eq. 5}$$

This is Bragg's Law, and can be satisfied only for wavelengths $\lambda \leq 2d$. In the equation, *n* is an integer representing the order of the diffraction peak. Each plane only reflects 10^{-3} to 10^{-5} of the incident radiation and thus 10^3 to 10^5 planes may contribute to the formation of the Bragg-reflected beam in a perfect crystal.

Most regular diffractometers use Bragg-Brentano geometry, which means that the angle between the detector and sample, and the sample and the incoming beam is the same. This ensures that only the photons that are in phase and diffract at the same angle as the one between the beam and the sample are detected.

While the geometric derivation of Bragg's Law, where it is assumed that atoms diffract X-rays, just as etched grating diffracts light, quickly yields the desired Bragg expression, the analogy is inadequate to explain the results of an X-ray diffraction experiment. A better analogy is to consider a large perfectly still lake in which posts of different shapes and sizes stick out of the water in a periodic array and are used as supports for piers of a dock for instance. If a series of waves impinge on these posts, there will be a pattern of the reflected waves propagating out in the lake. By studying this pattern, it should be possible to work out the pattern of the posts underneath the dock. This analogy describes the challenge a crystallographer faces when trying to unravel the structure of a crystal by using diffraction techniques. A more general derivation of the diffraction conditions can be found in Appendix IV.

Peak Broadening

In most diffraction experiments, it is mainly the position of the peaks in a diffraction profile and to some extent the relative intensities that are of interest. Analyzing the shape of the peak may however yield some additional information. The width of the peak, defined as the full width at half maximum (FWHM), is for instance increased as the crystalline domains are decreased (*23*). This can easily be seen in a powder diffraction pattern, where the rings become broader as 2θ is increased. By using Fourier techniques it is possible to analyze the whole shape of the diffraction peaks in order to obtain a distribution of crystallite sizes. Strain caused by crystalline defects, stacking faults or concentration gradients will also cause a broadening of the peaks, and determining the effect strain has on the FWHM is usually difficult as both strain and crystallite size contribute to the broadening in addition to instrumental broadening. The instrumental broadening is a result of several factors, and at a synchrotron depends mainly on the following; the focused X-ray spot on the sample having a certain radius, the beam not being perfectly monochromated, the angular aperture on the detector, axial divergence, and any misalignment in slit systems and the diffractometer. A synchrotron uses highly expensive optics in order to reduce instrumental broadening to a minimum, and any misalignments are usually accounted for in the software used for data reduction. Broadening from the sample is not however, and for thin film measurements this can be a problem. If the thin film is not perfectly aligned under rotation, i.e. the diffracted X-rays from the same crystal planes do not hit the exact same spot on the detector, there will be a broadening of the peak which needs to be accounted for in order to be able to determine crystallite sizes.

2.4.2 Synchrotron X-Ray Diffraction (SXRD)

A synchrotron is similar to a cyclotron in the way that it accelerates charged particles and forces them to go in a ring by utilizing magnetic fields. Unlike cyclotrons though, particles are not sent on colliding paths, but are instead bunched together and are sent collectively around in a ring. A schematic diagram is shown in Figure 6 (*24*).

When charged particles are accelerated, they emit electromagnetic waves. This is because the field lines around a charged particle are accelerated as well, but since the speed of light c is finite, the field lines far away do not accelerate at the same time as the ones close to the particle. Close to a charged particle, the field lines are directed radially toward the particle, further away though, the field lines still point toward the point the charged particle would be had it not been accelerated. In the area between this, there is a distortion and this distortion, traveling at the speed of light is what is called electromagnetic waves (*25*). The magnitude of the field distortion is proportional to the acceleration of the particle, and this is one of the reasons for why a synchrotron is formed like a ring. There are linear particle accelerators, but the degree of actual acceleration in these is very low as the particles travel close to the speed of light in the first place and thus only a small acceleration may take place. By using *bending magnets* to change the direction of the velocity $\boldsymbol{v}$, which can be done in a synchrotron, the centripetal acceleration $\boldsymbol{a}$ is given by:

$$\boldsymbol{a} = \frac{\boldsymbol{v}^2}{\boldsymbol{r}}, \qquad \text{Eq. 6}$$

which means that the emitted radiation intensity is very large. This is because the velocity in a certain direction may go from zero to very high in a very short amount of time. The extreme velocity of the charged particles, results in a very high photon flux and intensity, and this is useful in order to increase the signal to noise ratio as well as reduce the broadening of the Bragg peaks in XRD experiments. Figure 6 shows a schematic diagram of a synchrotron radiation facility and the shape of the electromagnetic radiation radiating from an electron. The radiation is shaped as a narrow cone, which lies tangent to the ring, much like the light of a flashlight going around in a circular motion. While fundamentally this theory is valid for any charged particle, a synchrotron uses electrons and in some cases positrons. The energy required to accelerate an electron close to the speed of light is several orders of magnitude lower than a proton for instance, and for radiation purposes this is consequently a lot more efficient.

Around the synchrotron there are several types of radiation sources apart from bending magnets. The most common in addition to bending magnets are *undulators* and *wiggler magnets*, and most of the other sources are more specialized versions of these.

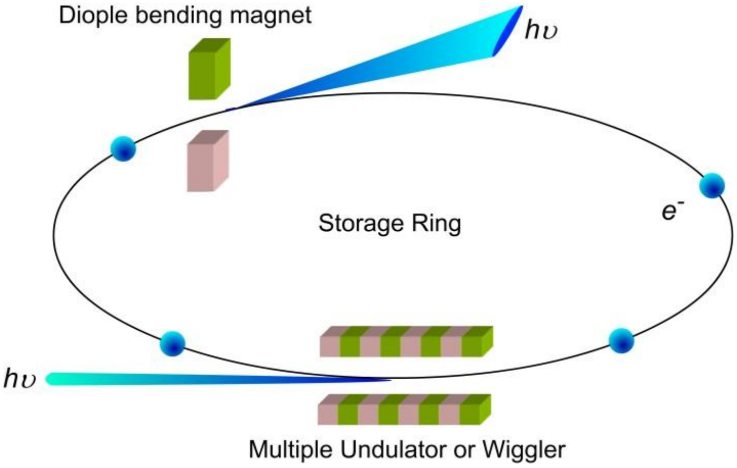

Figure 6: Schematic diagram of a synchrotron radiation accelerator (*24*), *hv* signifies photon source, while e^- are electron bunches stored in the ring.

The first generation synchrotrons only used bending magnets, which gives of a very broad range of wavelengths, similar to a light bulb giving off white light which contains a lot of different wavelengths. This has some advantages and is still used a lot today, and by using monochromators it is possible to select the desired wavelength needed for a certain experiment.

Undulators are more modern insertion devices that are found on straight sections of a synchrotron facility (*21*). They differ from bending magnets in the way that they have a magnetic structure which alternates between north and south, so as the electron goes through, it will experience a Lorentzian $\boldsymbol{v} \times \boldsymbol{B}$ force, where $\boldsymbol{v}$ is the speed of the electron and $\boldsymbol{B}$ is the magnetic field which is horizontal to the motion of the electron. This causes the electrons that pass through to oscillate laterally, which means that it is accelerating very rapidly and the resulting radiation has a much higher *brightness*[4] than a bending magnet and comes out in an even narrower cone. The horizontal oscillation also causes the radiation to become strongly polarized, and this has a large effect on how the samples need to be measured. The

---

[4] Brightness is a measure of how many photons pass through a certain area within a certain time. The brightness at a synchrotron can be as high as 10^{20} photons/sec/mm^2.

wavelength of the emitted radiation is equal to the undulator period λ_P, divided by the particle energy Υ due to relativistic Lorentz contraction, which happens because the electrons are traveling close to the speed of light. In addition, from a stationary laboratory view, all the electromagnetic radiation appears to be moving in the general direction of the electron. This results in a further reduction of the wavelength by a factor of 2Υ, due to the *Doppler effect*[5]. The resulting electromagnetic wave length λ for electrons traveling at velocities approaching the speed of light is thus defined the following way:

$$\lambda = \frac{\lambda_P}{2\Upsilon^2} \qquad \text{Eq. 7}$$

The undulator period length is in the order of centimeters, and when reduced by a factor of $2\Upsilon^2$ (10^{-6}-10^{-8}), the electromagnetic waves emitted will be in the vacuum ultraviolet and X-ray regime. The Lorentz and Doppler effect is much weaker when observed from an angle that is not in the direct path of the moving electrons, and thus the shortest wavelengths are only obtained over only a very few radians. The spectral resolution is proportional to the number of undulator periods and its wavelength can be shifted by changing the magnetic field. When the number of undulator periods is increased, the Fourier transform, which will give a frequency distribution of the produced waves, will become sharper and this is what results in a higher spectral resolution.

A wiggler magnet is very similar to an undulator in the way that it utilizes a similar alternating magnetic structure, but while an undulator usually has around 50-100 of these magnets, a wiggler has a lot fewer, typically ten or less. The magnetic field however is a lot stronger and the acceleration of the electron is even higher than in an undulator, which means that the photon energies are higher, but the resulting radiation has a lower brightness as the radiation cone is much broader. A comparison of the generated radiation from the different synchrotron light generators is shown in Figure 7.

Undulators are in general more flexible than bending magnets, as by changing the magnetic field, which in practice is done by changing the distance between the opposing magnets in the undulator, the critical photon energy may be varied to fit experimental needs. The critical

---

[5] Doppler effect happens when the source of waves is moving toward an observer. Each successive wave will be emitted from a position closer to the observer than the previous wave, and consequently the frequency is increased.

photon energy can be derived from the Heisenberg uncertainty principle and gives the spread in photon energy. It is defined as the energy where half the photons have less energy and the other half has more energy, as shown in Figure 8 by the dividing line in the spectrum.

Bending magnets define the geometry of the storage ring, and so the magnetic field cannot be changed unless one changes the geometry of the entire ring as well. This results in a fixed critical photon energy.

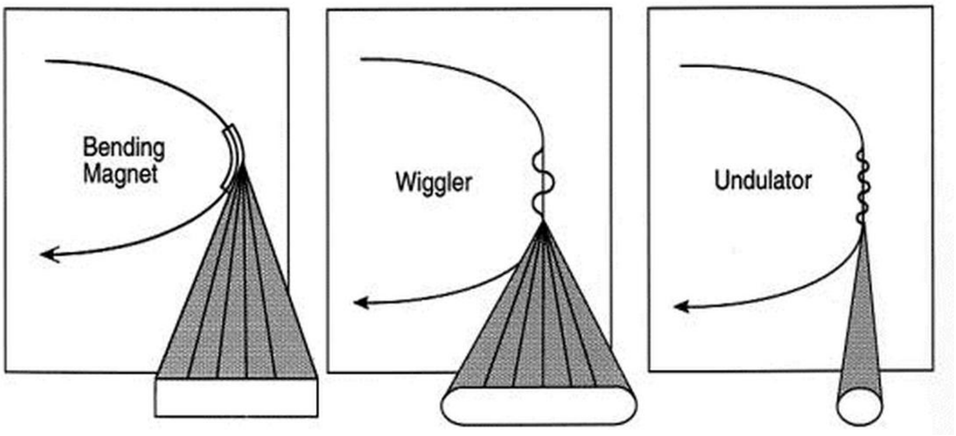

Figure 7: Schematic of three sources used for synchrotron light generation (*26*). The bending magnet utilizes the geometry of the ring and the centripetal accelleration is very high, resulting in large photon energies. The wiggler and undulator differ due to the angle of the horizontal oscillations, which is much larger for a wiggler, resulting in a much broader radiation cone and thus lower brightness, but the stronger magnetic fields yield higher photon energies.

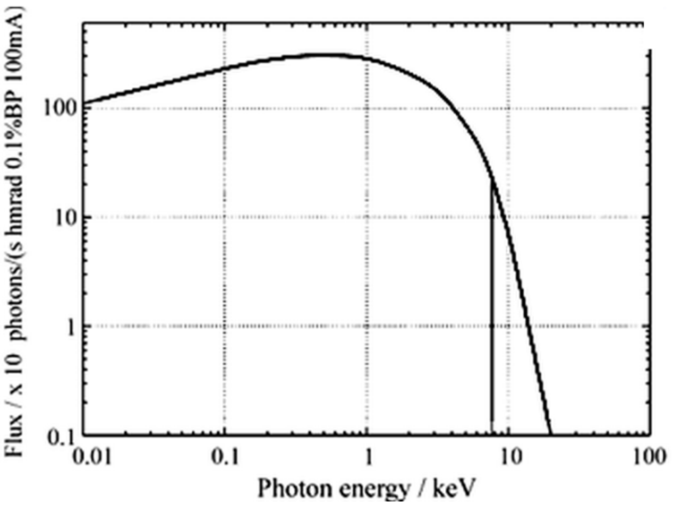

Figure 8: The photon flux emitted by a typical synchrotron light source. The vertical line indicates the critical photon energy used for a typical small angle X-ray scattering experiment at the Brazilian synchrotron light source (*27*).

Solving the Structure with SXRD

A technique called X-ray crystallography is a standard technique used for solving crystal structures, and is used at most synchrotron beam lines around the world (*21, 28, 29*). The technique uses integrated intensities of the diffraction peaks in order to reconstruct the electron density map within the unit cell in the crystal. This is done by Fourier transforming the diffraction intensities with appropriate phase assignment. However, in order to achieve high accuracy reconstruction, a high degree of completeness in diffraction data is necessary and consequently all possible reflections are measured multiple times in order to reduce systematic and statistical error. This is most efficiently done by using an area detector which can collect data from a lot of angles. Doing this on a regular diffractometer however, would take a lot of time, and high intensity X-ray sources, such as synchrotron radiation is needed in order to reduce the time needed to collect data efficiently. For this work, a six-axis goniometer with a large area *charge coupled device* (CCD)-detector was employed. The CCD is able to convert incoming photons into electron charges which can be used to produce high quality images.

One of the main troubles within X-ray crystallography is referred to as the *phase problem*. This problem arises from the fact that the diffraction data contains information only on the amplitude (which is correlated to the intensity) and not the phase of the structure factor. The phase of the structure factor can be used to reconstruct the electron density of the crystal, which is needed in order to solve complex structures like proteins (*30*). The geometric structure factor F_{hkl} can be written as:

$$F_{hkl} \propto \sum_{j=1}^{n} f_j \cdot e^{2\pi i(hx_i + ky_i + lz_i)}, \qquad \text{Eq. 8}$$

where f_j is the form factor, which holds information about the electronic properties of the atoms. A derivation of F_{hkl} can be found in Appendix IV. The second term depends on the atomic positions and is used to find the structure. Experimentally the intensity of a reflection is measured, and this is given by the Eq. 9:

$$I_{hkl} = |F_{hkl}|^2 \cdot LP \cdot A. \qquad \text{Eq. 9}$$

LP is a combined geometry and polarization factor which depends on the particular experimental setup, while A is an absorption correction factor which may be applied. These equations show that only the scalar magnitude of F_{hkl} (i.e. $|F_{hkl|}$) can be determined experimentally and not the complex scattering factor itself. In order to obtain information of the phases, additional phasing experiments can be done.

2.4.3 Scanning Electron Microscope (SEM)

The SEM utilizes electrons in order to scan a surface to obtain information about the phase contrast, topography and morphology of the sample. Electrons from a filament are accelerated down to the sample through a lens system which focuses the beam to a spot of a chosen size. The spot has the shape of a droplet and penetrates a few nanometers down in the sample and is what governs the resolution of the obtained images. When the electron beam hits the sample it will generate X-rays as well as elastically and inelastically scattered electrons, and these can be detected by various detectors.

The inelastically scattered electrons are called secondary electrons, as they are a result of collisions between the electrons from the beam and electrons from the sample surface. Electrons from the electron beam that collide with electrons further down than the electron mean free path are not detected, as these do not have the energy required to escape from the surface. Thus secondary electrons are signals that only give information from a depth corresponding to the mean free path of the electrons in the sample, and the contrast of the generated image is consequently very sensitive to the topography. Concave areas on the surface will appear brighter as more electrons will be able to escape the sample surface from this region. An Everheart-Thornley detector (ETD), which employs a Faraday cage in order to separate the high energy from the low energy electrons (<50 eV), is used in order to detect the secondary electrons.

The elastically scattered electrons are called backscattered electrons as they are a result of electrons from the beam that get deflected by the positively charged cores of the atoms in the sample. A separate detector, called solid state detector (SSD), is used for the backscattered electrons. The energies of these electrons are much higher than the secondary electrons due to the inelastic scattering and thus give information from deeper down in the sample than the secondary electron do. The probability of an elastic scattering event is however quite small and thus the intensity of the backscattered electrons is much lower. The images are used to reveal various phases in the sample. The heavier elements have a more positively charged core, which causes more of the electrons to become backscattered. Heavier elements will consequently appear brighter on the resulting image. In addition, the image can also reveal some topography of the sample, as more electrons will hit the detector from faces that are aligned towards the detector and thus will exhibit a brighter contrast. The topographical contrast is however not as good as the one obtained by the ETD.

There are a few sample requirements for the use of SEM. As the sample is loaded into a vacuum chamber, vacuum sensitive samples are a challenge. The sample also needs to be stable while being subjugated to an electron beam. Carbon rich samples may for instance have burn marks on the scanned areas. Insulating samples will generally charge up by the electron beam as the electrons are not being conducted away. The image will become brighter as the electron beam charges up the sample, until it becomes impossible to obtain images. This can however be remedied by using a low-vacuum mode in which water vapour is pumped into the lower parts of the chamber in order to conduct the electrons away. This has a consequence for the resolution, and a different detector, called a large-field detector (LFD) is employed in order to obtain information from the secondary electrons, which is positioned closer to the sample than the ETD (*31*). This mode is found in most SEM models used at the present and is called environmental scanning electron microscopy (ESEM).

A SEM is usually also equipped with an X-ray detector which can be used to find the composition at a certain point in the sample. Different types of detectors are used in different models; however the SEM used in this study employs an energy dispersive X-ray detector (EDS), which consists of a semiconducting crystal that creates an electron-hole pair when hit by X-rays. The energy needed in order to create the pair is characteristic for a specific element and the resulting charge pulse can be used to get quantitative information about the elemental composition in the area which is being investigated. Elements lighter than boron can however not be detected and the sensitivity is slightly reduced for elements lighter than sodium (*32*).

2.4.4 Atomic Force Microscopy (AFM)

The atomic force microscope (AFM) is a characterization technique used to scan the surface of a material and obtain a high quality image of the topography. Like other scanning probe microscopes it utilizes a sharp tip to raster a surface. The tip is mounted on a flexible cantilever so that when the tip experiences a force from the surface, the cantilever will bend (*33*). In order to observe this, a laser is pointed at the top of the cantilever and the reflection is monitored on a photodiode detector. Usually the detector is split into four quadrants and the laser is positioned so that it reflects to the middle of these. When forces act on the tip, the reflected laser beam will shift and this shift is used to give a 3D-image of the surface by plotting the laser deflection against the tip position.

In order to control the cantilever, the AFM uses a piezoelectric position control system, similar to the one used in scanning tunneling microscopes. By applying opposite signed voltages on ± *x* and *y* quadrants relative to the inner tube, the tube scanner (Figure 9) will deflect along *x* or *y*. Applying the same voltage on all four quadrants results in *z*-motion.

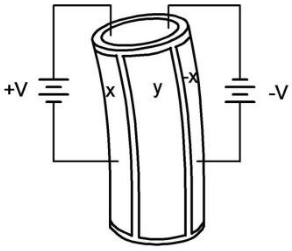

Figure 9: The tube scanner used to control the AFM cantilever (*34*).

When the microscope operates in constant force mode, i.e. the force is kept constant by adjusting the height of the tip above the sample; part of the signal obtained from the sample goes back to the piezotube. This is then used to adjust the *z*-position of the cantilever in order to avoid that the tip comes in direct contact with the sample, possibly damaging the tip.

The AFM can be used in a large variety of modes, however only tapping mode has been used in this work. In this mode the cantilever oscillates at or near its *resonant frequency*[6] by using a piezoelectric crystal (*33*). As the tip approaches the surface, the amplitude will decrease due to the forces acting on the tip and this is used to measure the features of the surface. Tapping mode enables phase imaging, which can be used to give an indication about the energy dissipation between the tip-sample interactions. This image is very sensitive to elastic properties as well as crystallinity of the sample as crystalline objects exhibit brighter contrast than the amorphous ones (*33*). In this way the phase image can give important structural information that is hidden in the topographical image.

The resolution of the image depends largely on the tip, the sharper the tip, the higher the resolution. It is pointless to scan particles with smaller size than the tip radius. In addition the images obtained will not give a true representation of the sample morphology if the sample is

---

[6] Resonant frequency refers to when the cantilever oscillates with the highest possible amplitude.

very rough. Due to the nature of the control system, the AFM-scan is unable to show crevasses and corners correctly as illustrated in Figure 10.

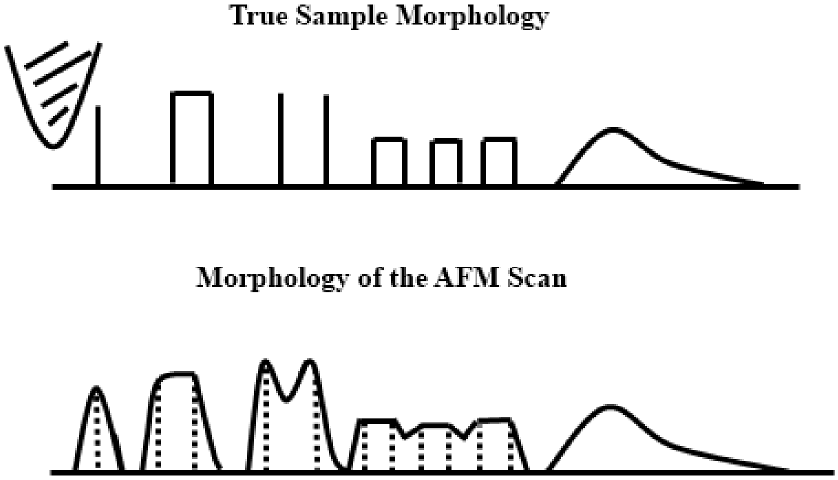

Figure 10: Illustration of the mechanics of the AFM. The resolution of the image depends on the size of the tip. A porous surface may appear flat if the pore dimensions are an order smaller than the AFM tip for instance.

2.4.5 Ellipsometry

Ellipsometry is an optical non-destructive technique used for characterizing dielectric properties of interfaces and thin films. The principle behind the technique can be described as when a beam of polarized light is reflected or transmitted through a film or interface, there will be a polarization transformation (*35*). Linearly polarized light, when reflected from a surface, will become elliptically polarized if there are interfaces present in the sample, which is the case in thin films. This information can be used to find the optical constant, absorbance as well as the thickness of the film and is done by varying these parameters and solving the Fresnel equations (*36*). The calculated values that match experimental data best provide the optical constants and thickness parameters of the sample. The technique can thus be used to find information about layers that are thinner than the wavelength of the probing light, down to a single atomic layer.

Various types of light can be used in order to obtain different information about the sample; ultraviolet is however most commonly used. Figure 11 shows how the light is sent through a polarizer, which eventually causes the light to be elliptically polarized in order to reflect linearly off the surface. The compensators are optional, but can be used to modify the phase or polarization of the light if needed. The reflected light is sent through a second polarizer, which is called an analyzer and then sent to the detector which measures the change in linear and parallel polarization.

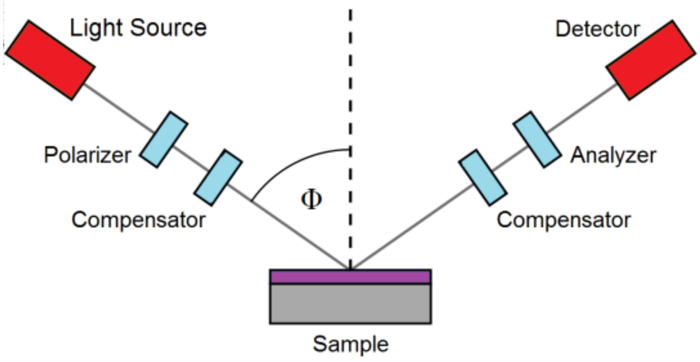

Figure 11: Schematic setup of an ellipsometry experiment

2.5 *Ab Initio* Calculations

2.5.1 Quantum Mechanical Background

Models are commonly used in physics to extract the essence of complicated problems, and most often uses idealized systems to represent the most important properties. The real world though, is rarely as ideal as the models that are made and in some cases this becomes a problem as it hinders understanding of the real physics underlying the problem. As one goes down to atomic levels and below, this problem becomes particularly troublesome, due to both the large number of particles in real systems, as well as the need to use quantum mechanics at this level (*37*).

At the University of Oslo there has been a long tradition to study such problems, with Egil Hylleraas being among the first in the field to study atomic physics. In 1929 he was the first to calculate the energy levels in helium precisely enough to state that quantum mechanics is valid also in systems with more than one electron (*38*).

The field practically stopped its development until computer hardware and software was developed, and in 1998 Kohn was awarded the Nobel Prize in chemistry for the development of DFT.

2.5.2 The Many-Body Problem

The energy, E, of a system can be found by solving the Schrödinger equation and can be used to describe the correlation between atoms in a system completely. Particles are described by a wave function, Ψ .

$$\hat{H}\Psi = E\Psi \qquad \text{Eq. 10}$$

The Hamilton operator $\hat{H}$ consists of kinetic energies T and potential energies V:

$$\hat{H} = T_N(\mathbf{R}) + T_e(\mathbf{r}) + V_{Ne}(\mathbf{R}, \mathbf{r}) + V_{ee}(\mathbf{r}) + V_{NN}(\mathbf{R}) \qquad \text{Eq. 11}$$

The first two parts describe the kinetic energy of the nuclei and the electrons and their positions **R** and **r** respectively. The last parts describe the potential energies between the nuclei and the electrons, the electron-electron interactions and the interaction between the nuclei respectively. The potential between the nuclei and the electron V_{Ne}, couples the equations and make them non-linear. This makes it extremely complicated to find an exact solution, even for a small number of atoms.

In order to decouple the equation it is possible to use the Born-Oppenheimer approximation. It uses the fact that the mass of a proton roughly 1800 times larger than the mass of an electron, and this implies that the electrons move so much faster than the nuclei, that their movement can be considered mutually independent. This is practically done by assuming the nuclei to be stationary and the electrons to move in a field set up by the nuclei. On the other hand, when we want to describe the movements of atoms, we suppose that the electronic structure is able to instantaneously respond to this movement. The result is that it is possible to separate the equation into one electronic and one nuclear. The electronic equation disregards the nuclear movement completely and thus the equation can be broken down to:

$$\hat{H}_e\Psi_e(\mathbf{r}) = (T_e(\mathbf{r}) + V_{Ne}(\mathbf{R}, \mathbf{r}) + V_{ee}(\mathbf{r}))\,\Psi_e(\mathbf{r}) = E_e(\mathbf{R})\,\Psi_e(\mathrm{r}). \qquad \text{Eq. 12}$$

The coordinates of the nuclei **R**, are parameters in the equation and the coupling between nuclei and electrons is thus removed.

There is still one important remaining problem however. The electrons are still coupled to each other through the term $V_{ee}(\mathbf{r})$, and further simplification is needed in order to solve the Schrödinger equation efficiently. There are different approaches to this problem, but a common way is to replace V_{ee} by an effective background potential in which every electron is placed. This reduces the Hamiltonian to a sum of one particle operators and this makes it possible to perform calculations.

2.5.3 Density Functional Theory

Density functional theory (DFT) is basically based on two papers, the first by Hohenberg and Kohn in 1964, and the second one by Kohn and Sham in 1965 (*39*). The method described by Hohenberg and Kohn differs from previous quantum mechanical calculations by the fact that it doesn’t try to solve the full wave function, which is still is considered impossible to solve exact for atoms with more than one electron. Instead Hohenberg and Kohn tried to find the ground state by using the electron density as a function of an energy functional[7]. They proved that only one electron density can ever correspond to a certain energy and thus by finding the electron density that gives the lowest energy it is possible to find the exact ground state energy of the system. While the theorems originally only were proven for the ground state, it has later been shown that DFT is also valid for excited states although this is mostly used in what is called time-dependent DFT (*40*). In order to obtain results valid at more than 0 K, molecular dynamics (MD) may be employed. This simulates temperature and introduces vibrations in the selected atoms for a certain time and is done by numerically solving Newton’s equations of motion for a system of interacting particles. Long MD runs do however not give reliable results as cumulative errors in the numerical integration significantly affect the results.

The Hohenberg-Kohn Theorems

The Thomas-Fermi theory (TF theory), which was presented in 1927 marked the beginning of rudimentary DFT. It was a model where the kinetic energy is expressed by the electron density function, while repulsion and interactions were calculated in a classical manner (*41*). The theory was useful for describing qualitative trends, like total energies of atoms, but was almost of no use when it came to systems containing valence electrons, which is normally the case in chemistry and material science. As an example, it did not lead to any chemical binding. There was however one thing that picked Kohn’s interest. The theory considered

---

[7] A functional is like a function, except that instead of inserting a variable like *x*, as you would in a function, you instead insert a function like *f(x)* in a functional.

interacting electrons moving in an external potential $V(\boldsymbol{r})$ and implied a very simple one to one relation between this and the electron density distribution $\rho(\boldsymbol{r})$. Since Schrödinger theory was expressed in terms of $\Psi(\boldsymbol{x}_1, \boldsymbol{x}_2, ..., \boldsymbol{x}_N)$ and TF-theory in terms of $\rho(\boldsymbol{r})$, it was unclear how to establish a connection between them. So the question was if it in principle was possible to describe the electronic ground state completely in terms of $\rho(\boldsymbol{r})$. This hypothesis is the fundament for modern DFT and is what lead to the Hohenberg-Kohn theorems.

If one considers wave function for all N electrons of a material, i.e. $\Psi(\boldsymbol{x}_1, \boldsymbol{x}_2, ..., \boldsymbol{x}_N)$, all the observables are determined by the external potential from the nuclei $V_{ext}(\boldsymbol{r})$ and the number of nuclei N. The first of Hohenberg and Kohn's theorems then state that one instead can use the electron density $\rho(\boldsymbol{r})$ as the primary variable.

Theorem: The ground state density $\rho(\boldsymbol{r})$ of a bound system of interacting electrons in some external potential $V_{ext}(\boldsymbol{r})$ determines this potential uniquely.

The number of electrons N can easily be found by simple integration of the electron density:

$$N = \int \rho(\boldsymbol{r}) d(\boldsymbol{r}) \qquad \text{Eq. 13}$$

The implication of this theorem is consequently that both N and $V_{ext}(\boldsymbol{r})$ are determined by $\rho(\boldsymbol{r})$ and in principle all observables of the system have been found, i.e. they are *functionals* of the electron density, and for this the theory has been called *density functional theory*.

The ground state energy can now be written as a functional of ρ:

$$E[\rho] = T[\rho] + V_{ne}[\rho] + V_{ee}[\rho] = \int \rho(\boldsymbol{r}) V_{ext}(\boldsymbol{r}) d\boldsymbol{r} + F[\rho], \qquad \text{Eq. 14}$$

where $F[\rho] = T[\rho] + V_{ee}[\rho]$. So far no assumptions have been made, and F is thus a universal functional of ρ. This means that if F can be found, it would be possible to use the equation on any system consisting of fermions in an external potential. A method for finding F is to use the variation principle, which is based on finding an upper limit for the ground state given a Hamiltonian operator, H, and a well behaved trial wave function, φ that satisfies the boundary conditions of the Hamiltonian.

$$\langle \varphi | H | \varphi \rangle \geq E_0 \qquad \text{Eq. 15}$$

E_0 is the lowest energy eigenvalue of H, and by improving the trial function it is possible to find the lowest possible energy for the given Hamiltonian.

Hohenberg and Kohn developed the theory further and eventually proved that it is possible to use the variation principle with a trial function for the electron density instead of the wave function, which confirmed that the variation principle would give the correct ground state energy with an electron density functional. The second Hohenberg-Kohn theorem proves that the energy E which is found is actually the lowest energy when the system is in its ground state.

The Kohn – Sham Equations

The Hohenberg-Kohn theorems are of no practical use before at least a crude approximation of F can be made. This problem was solved by Kohn and Sham in 1965 and resulted in a system for finding the electron density which is used in all programs using DFT today (*39*).

In order to arrive at the Kohn-Sham equations, one starts with that the N-particle wave function $\Psi(\boldsymbol{x}_1, \boldsymbol{x}_2, \ldots, \boldsymbol{x}_N)$ can be represented as N one-particle wave functions $\psi_k(\boldsymbol{r})$. This yields the following equations, called the Kohn-Sham equations:

$$V_{eff}(\boldsymbol{r}) = V_{ext}(\boldsymbol{r}) + V_{XC}(\boldsymbol{r}) + \int \rho(\boldsymbol{r}') \frac{e}{4\pi\varepsilon_0|\boldsymbol{r} - \boldsymbol{r}'|} d^3r' \qquad \text{Eq. 16}$$

The equation contains the given external potential $V_{ext}(\boldsymbol{r})$, the exchange-correlation potential $V_{XC}(\boldsymbol{r})$, which will be explained later, as well as the Coulomb potential. By using this potential in the one-particle wave function, the following equation is obtained:

$$(\nabla_k^2 + V_{eff}(\boldsymbol{r}))\psi_k(\boldsymbol{r}) = \epsilon_k(\boldsymbol{r})\psi_k(\boldsymbol{r}), \qquad \text{Eq. 17}$$

which is not coupled to the previous equation and consequently straightforward to solve in most cases. The effective potential $V_{eff}(\boldsymbol{r})$ depends on ρ, so the equations may not be solved directly. First an expression for ρ must be found. Kohn and Sham simply found an estimate for the ground state density by summing up all the N non-interacting one-particle orbitals:

$$\rho(r) = \sum_{k=1}^{N} |\psi_k(r)|^2 \qquad \text{Eq. 18}$$

This can now be used to find the effective potential and solve the one-particle equations in order to find a new electron density, which usually is more accurate than the one that was found using the non-interacting atoms. The new electron density can then be used to solve the equation again and this can be done until self consistency is reached, i.e. the input density and the density you obtain after solving the equations is the same. Until now, only the Born-Oppenheimer approximation has been used, and so this should then give nearly the exact ground state density, if no other approximations needed to be done. There is however one last thing which needs to be approximated, which is the exchange-correlation potential $V_{XC}(\mathbf{r})$. Exchange-correlation refers to two kinds of interactions between electrons.

Exchange potential is the potential that is created by the exchange force between two identical fermions due to symmetry requirements. In essence this means that an antisymmetric wave function is required, which can be solved by constructing the Slater determinant, which always changes sign when two particles are exchanged. This is used in Hartee-Fock theory by replacing the N-particle wave function with an $N \times N$ Slater determinant and results in N coupled equations that can be solved iteratively in a self-consistent way. The problem, however, is that this does not account for correlation effects. Correlation effects arise due to the fact that the probability of finding an electron at a certain position depends on the position of other electrons. If an electron a is at a position $\mathbf{r}_a$, and an electron b moves from $\mathbf{r}_b$ to $\mathbf{r}_b'$, this will affect the electron density at $\mathbf{r}_a$ and as a result the probability of finding a at $\mathbf{r}_a$. While it can be shown that the sum of exchange and correlation potentials is a universal functional, only depending on the electron density, the functional itself has not yet been found, and probably never will be and thus it needs to be approximated.

Approximations to the Exchange-Correlation Potential

In order for Kohn and Sham to check the power of their equations, they needed an approximation to the exchange-correlation potential, as they realized that finding an exact expression would be out of their reach. The assumption they made was that the exchange-correlation contribution is the contribution that would arise from a uniform free electron gas having the same density. In other words, the local electron density was set as constant, which made calculations much easier (*39*, *42*). This is called the local density approximation (LDA). Since the exchange contribution of a uniform electron gas had already been calculated by Enrico Fermi in 1930, they could test their results right away. At this point they neglected correlation, but in LDA today very accurate values for correlation based on quantum mechanical Monte-Carlo is employed, giving a fairly good description of materials with slowly varying electron density. In general LDA underestimates the exchange and correlation contributions (which are repulsive), resulting in increased bond strength, which again leads to too small lattice constants or bulk moduli.

For systems with spin polarization, like the O_2-molecule, a generalization to LDA, called the local spin-density approximation (LSD or LSDA) can be done (*43*, *44*). This approximation employs two electron density functionals instead of one, i.e. one for each spin density.

While LSD gives very accurate results in some cases, it generally is a crude approximation and it is hardly reasonable to assume that the electron density is locally constant. This is especially true when *d*- or *f*-electrons are involved, but applies more or less in all cases. A better approach is to take gradients of the electron density into account. This could be simply done by using a Taylor expansion on the electron density. This however is not very successful, as the small region around each electron that is inaccessible due to the Pauli repulsion is not treated correctly this way. A better way is to write the exchange-correlation potential as a generalized functional of the electron density and the gradients of the electron density:

$$E_{XC}^{GGA} = \int d^3 r f[\rho(\boldsymbol{r}), \nabla\rho(\boldsymbol{r}), \ldots]. \qquad \text{Eq. 19}$$

This is called the generalized gradient approximation (GGA) (*45*).

There are two main approaches to finding GGA functional. One method is to parameterize the functional and to optimize the parameters by comparing large number of materials to experimental results. By increasing the number of parameters and using more experimental results, it is possible to continuously improve the functionals. This gives exceptional good results for atoms and molecules, but in most cases poor results when transferred to solid state.

The other method is called *ab-inito*, which means that only fundamental principles are used. There are several fundamental principles that lead to different functionals, and different approaches are used. One principle is correct behavior in the low and high density regions, while another is that the functional should converge towards LDA for slow varying densities. A popular requirement is a correct description of the exchange hole, which is a result of attraction between identical bosons and repulsion between identical fermions (*37*, *46*). The most common functionals are PW91 (*47*) and PBE (*45*), and PW91 is what is used in this work. These functionals are not very successful on atoms and molecules, but have shown very good results for solid state. Two problems with GGA is that bond strengths are generally calculated to be too weak instead of too strong as in LDA, and the band gap is usually underestimated.

Basis Functions

The iterative self-consistency cycle uses the wave function of the electrons. In order to produce the best functions, the best possible basis set is needed. The basis set functions are used to make linear combinations, which means that the larger the basis set is, the better the approximation will be. Having a large basis set will however slow the calculations down, and so a compromise is usually needed in order to achieve the best results compared to the amount of work done. One of the main advantages of doing calculations is the possibility of trying a lot of possibilities in a fairly short amount of time, and so the efficiency of the calculations should always be considered. Some basis functions are also more suitable than others for certain problems. In general it is possible to view the electrons of a solid from two different sides. Electrons near the core do not participate in bonding of atoms and may be regarded as belonging to a particular atom. Electrons in the conduction band or taking part in chemical bonding may on the other hand be regarded as nearly free. This causes problems with band structure calculations. The potential from the nucleus is very large close to the core and is very similar to that of atomic orbitals. Between the atoms however, the potential is rather weak. In addition, the potential around the nucleus is spherical, while everywhere else only crystal symmetry matters. In order to describe both these areas there are two main types of basis functions, atomic basis functions which consists of linear combination of atomic orbitals (LCAO), and plane waves (PW). LCAO is best suited to describe atoms and molecules, while PW are infinite in extension and are best to describe solid state materials. There is however no strict rule and several programs use for instance LCAO in order to introduce one dimensional structures like strings or tubes or two dimensional surfaces. A third possibility is to use a combination of these, which is employed in linearized augmented plane wave (LAPW). An increasing amount of programs however employ pseudopotentials, which solves the problem of strongly oscillating functions around the nuclei by describing this area with a weaker pseudopotential. The wave function close to the nucleus is then incorrect, but outside a certain radius, both the wave function and the potentials are correct. This reduces the number or plane waves needed dramatically, but the calculated energy is not correct. In most cases though, only the relative energy is of interest and thus this is of no consequence.

2.6 DFT Calculations for Solid Surfaces

In order to study a surface the ideal model would be a slice of material that is infinite in two dimensions, but finite along the direction normal to the surface. The most common way to do this is shown in Figure 12. By creating a supercell with an inserted vacuum layer above the atoms in the lower portion of the supercell, the repeating cell in all three directions will be a series of stacked slabs that are infinite in the *x* and *y* directions but span only a few layers in the *z* direction.

When using such a slab model, it is important that the vacuum layer separating the slab is large enough, in order for the electron density of the material to tail off to zero in the vacuum space. This has the effect that the bottom of the slab has no effect on the top of the next slab. Most codes are not designed for surfaces and having a large vacuum layer is thus quite time consuming computationally, but some codes like DMol-3 are able to understand vacuum layers and thus sharply reduce the time needed for surface calculations.

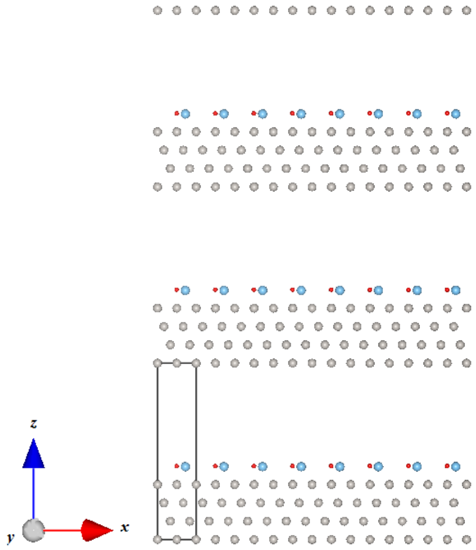

Figure 12: Two dimensional image of a four layer slab of Pt (grey) with TiO_2 adsorbed to the surface. Note that the *y* axis is pointed away from the reader. The supercell is shown in the lower left corner. Repeating this unit cell in all directions results in a slab which is infinite in the *x* and *y* direction and is separated from the next slab by a vacuum layer in the *z* direction. This method is called the slab model and is used in order to simulate surfaces.

The thickness of the slab is also important for surface calculations. In general thicker slabs will give a more accurate result but increases computational time drastically with each layer and thus finding the smallest slab size where the lowest layers are close to the bulk configuration will save a lot of computational time. Finding the needed vacuum and slab thickness can be done by doing calculations and varying these until the change in energy or the property of interest is converged to a certain threshold needed for the type of material being investigated.

2.6.1 Calculation of Surface Energies

The surface energy of a specific surface, usually denoted as σ, is the energy required to cleave the bulk in order to create the specific surfaces. Since two surfaces are created when a crystal is cleaved, the surface energy will be the energies of both these surfaces (*48*). The surface energy from a DFT calculation can thus be found using:

$$\sigma = \frac{E_{slab} - E_{bulk}}{2A}, \qquad \text{Eq. 20}$$

where E_{slab} is the total energy of the slab model for the surface while E_{bulk} is the total energy for the same number of atoms in the bulk and A is the area of one of the surfaces.

3 Prior Art

This section will treat previous work relevant to this study. There are three main parts, which each require their own fundament and consequently this chapter will address each part on its own. Previous methods used to grow ZnO and ZnS single crystals will be presented first, followed by previous X-ray diffraction techniques used for the characterization of the thin films, while *ab intio* calculations done on the polar surfaces of ZnO will be treated at the end of this chapter.

3.1 The Growth of ZnO and ZnS Single Crystals

In order to produce large single crystal substrates of ZnO for deposition Avrutin (*3*) claims that there are three techniques that are currently viable commercially, i.e. hydrothermal (*49-51*), melt grown (modification of the Bridgeman technique) (*52*) and the seeded chemical vapour transport growth (*53-56*). The best method for large scale production has been achieved using hydrothermal methods, which uses water as a polar solvent that forms metastable products with the ZnO solute. In order to enhance the solubility of ZnO in water, a KOH/LiOH mineralizer must be used. This causes a fairly large amount of K and especially Li to be incorporated in the crystal, which is a significant problem for the use of hydrothermally grown ZnO as substrates as they segregate to the surface and deter epitaxial growth (*3*).

Large growth rates in the range of several millimetres per hour can be achieved with the Czochralski and Bridgeman methods, but few materials can withstand temperatures up to 1975 °C, which is required to melt ZnO. Shultz et al. (*52*) demonstrated however that it is possible using an iridium crucible as this material has a sufficiently low oxidation rate at these temperatures. At 1000-1200 °C however, the oxidation rate of iridium is intolerable, and the crucible will be destroyed if heated to this temperature in an oxygen atmosphere. The problem was however brilliantly circumvented by using a CO_2 atmosphere. At elevated temperatures, CO_2 dissociates through the reaction:

$$CO_2 \Rightarrow CO + \tfrac{1}{2}O_2. \qquad \text{Eq. 21}$$

At 1000 °C the oxygen pressure resulting from the dissociation of CO is low enough to avoid oxidation of iridium, but at 1975 °C however, the oxygen pressure is high enough to keep the ZnO melt stable. The impurity composition with this technique has however not been reported in sufficient detail. Cracks resulting from thermal expansion mismatch between the Ir crucible and the ZnO are also known to happen using this technique.

Of all the methods to grow ZnO wafers, chemical vapour transport is the method that by far yields the least amount of residual impurities. This enables homoepitaxial growth on ZnO substrates grown by CVT without fear of impurities diffusing from the substrate to the film. Table 1 shows glow discharge mass spectrometry data for three ZnO single crystals grown by seeded chemical vapour transport by (*3*). The only significant impurity stems from Si, which is due to contamination from the quartz ampoule.

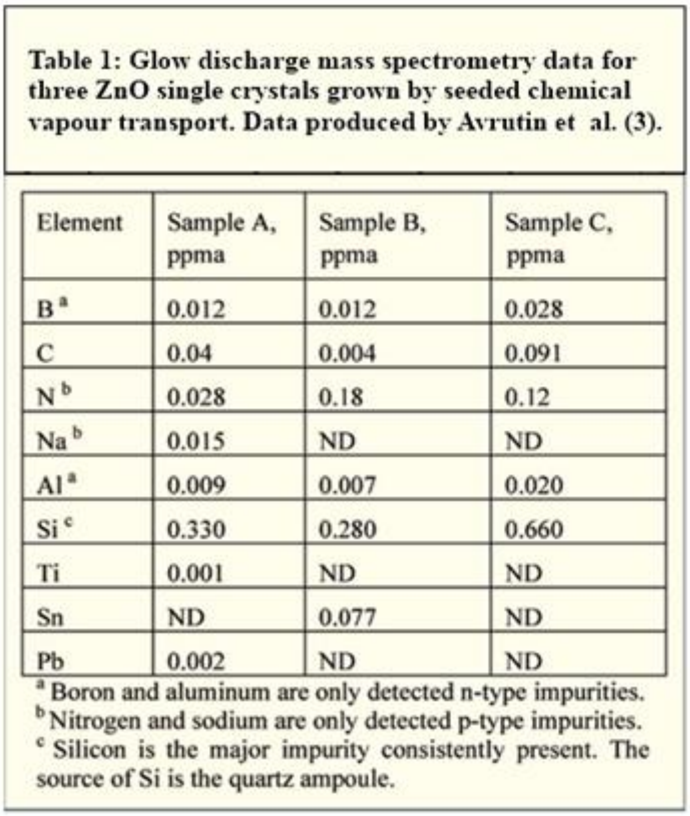

Table 1: Glow discharge mass spectrometry data for three ZnO single crystals grown by seeded chemical vapour transport. Data produced by Avrutin et al. (3).

Element	Sample A, ppma	Sample B, ppma	Sample C, ppma
B [a]	0.012	0.012	0.028
C	0.04	0.004	0.091
N [b]	0.028	0.18	0.12
Na [b]	0.015	ND	ND
Al [a]	0.009	0.007	0.020
Si [c]	0.330	0.280	0.660
Ti	0.001	ND	ND
Sn	ND	0.077	ND
Pb	0.002	ND	ND

[a] Boron and aluminum are only detected n-type impurities.
[b] Nitrogen and sodium are only detected p-type impurities.
[c] Silicon is the major impurity consistently present. The source of Si is the quartz ampoule.

The major drawback with CVT is low growth rates, which results in higher production costs. In order to produce single crystals of 1 cm^3 after 40 days, Ntep et al. used chlorine and carbon as transport agent, a source temperature of 1000 °C and a growth temperature difference of ΔT of 30 °C (*55*).

Mycielski et al. produced polycrystalline ZnO with growth rates of about 1-2 mm per day using a mixture of H_2 + C + H_2O as transport agent. The source temperature was held at about 1100-1150 °C, with the growth taking place in the cooler end of the ampoule at a temperature around 50 °C lower (*2*). The resulting crystals all had a red colour which is suggested could be a result of using carbon as the transport agent as this may reduce the Zn atoms, which in turn results in large concentration of oxygen vacancies. Red coloured ZnO crystals have also been reported by other groups using carbon as transport agent (*57*).

Shiloh and Gutman obtained fairly large growth rates of 15 mg/hr cm^2 when using NH_4Cl as transport agent when growing ZnO single crystals (*53*). NH_4Cl dissociates to NH_3 + HCl, and NH_3 dissociates in turn to N_2 and H_2. Both H_2 and HCl can be used to transport ZnO as described in section 4.1.

The traditional way to grow ZnS single crystals, has been using chemical vapour transport with iodine as transport agent (*58*); however NH_4Cl has also been reported as a possible transport agent and works in the same way as with ZnO (*59*).

3.2 Thin Film X-ray Diffraction

X-ray diffraction of crystalline thin films is difficult using regular Bragg-Brentano geometry as only the planes parallel to the surface will diffract. This means that only few specific (*hkl*) peaks show up, while other Bragg peaks will not show up according to Ma et al. (*60*). Usually a few reflections is enough to index the film and determine growth directions, although finer details about crystallinity, and residual strain is difficult to obtain. Another problem is that every plane only diffracts between 10^{-3}-10^{-5} of the incoming photons. This means that the diffracted photons will mostly be a result of diffraction from the substrate, while the intensity resulting from thin film diffraction will sometimes be too low to discern from noise if the intensity of the beam is not high enough. Several methods have previously been employed to overcome these problems however.

An obvious way to increase the intensity of diffraction peaks from the thin film is to use very low incident angles of the beam, as this gives the photons a longer path through the film and consequently more planes will contribute to the diffraction. At low enough angles, the incoming beam will be totally reflected however and will no longer penetrate into the sample. In grazing incidence small angle X-ray scattering (GISAXS), the angle of the incident beam is set so the beam is totally reflected from the surface, followed by a small angle diffraction of the thin film (*61*). This can for instance be used to characterize the nanostructure of the film, like islands formed in the initial stages of thin film growth or the pore structure in porous thin films (*62*). While not strictly necessary, these measurements are generally done at synchrotron radiation facilities in order to obtain the most accurate results.

In sector 12ID-B at the Advanced Photon Source (APS) in Argonne (USA), *in situ* atomic layer deposition of ZnO has been carried out using a six-circle diffractometer by Fong et al. (*63*). A schematic of the setup is shown in Figure 13. The same setup is used in order to perform total reflection measurements. The incident angle on the substrate is set to 0.1 ° in order to optimize the signal from the ultrathin film for the XRD measurements. For the X-ray Fluorescence (XRF) an incident angle of 1 ° was used. The setup was employed in order to find out how ZnO grows on Si. With this setup they were able to determine growth rates as well as the growth mechanism that governs the growth.

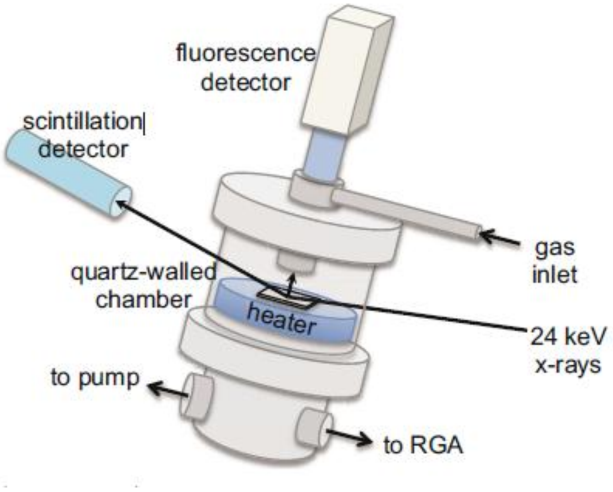

Figure 13: Schematic illustration of experimental setup used for *in situ* ALD X-ray studies at the APS by Fong et al. (*63*). The sample is positioned in an ALD chamber which has 2 mm thick quartz walls. 24 keV X-rays are used to penetrate these walls. The diffraction is measured using a Cyberstar scintillation detector and a fluorescence detector is positioned normal to the sample. A residual gas analyzer (RGA) is used to monitor gas exchange.

Thin film synchrotron X-ray diffraction using a six axis goniometer has previously also been done by Mo et al. at the ESRF (*64*), although details on the setup have not been described. In this study, diffuse scattering from the thin films were used to obtain information about the magnetic domain sizes in the thin film while being subjected to a strong electrical field.

W. Knaepen et al. (*65*) studied the solid state reaction between a 30 nm thin film of iridium on various silicon substrates with a combination of *in situ* X-ray diffraction, laser light and sheet resistance measurements. The experiments were carried out at the X20C beam line of the National Synchrotron Light Source at Brookhaven National Laboratory. The samples were heated from 100 °C to 1200 °C in a purified helium atmosphere using ramp anneals at a fixed rate of 0.3, 1, 3, 9 and 27 °C/s. In addition to an XRD spectra, the setup provided information about resistivity and surface roughness of the films through simultaneous acquisition of sheet resistance and laser light scattering measurements. Details about experimental setup are however not provided.

3.3 *Ab initio* calculations of the of the ZnO(0001) and ZnO(000-1) Surfaces in various Atmospheres

Since the ZnO(0001) surface is Zn-terminated, while the ZnO(000-1) surface is O terminated, the *c* axis becomes strongly polarized, and this makes calculations slightly more complicated and consequently the amount of modeling done on the system has been limited in previous years (*66*-*69*). As functionals are constantly improved and more experimental results become available, more accurate results are continuously being published on these systems, and even more publications have become available on the topic after the initiation of this work.

A problem arising when modeling the polar surfaces of ZnO is unrealistically strong contraction. Sung-Ho Na and Chul Hong Park suggested keeping the middle layers fixed in order to prevent this (*67*), which gives results in good agreement with experiments for the O terminated surface, but not for the Zn terminated one, where experiments show a slight outward relaxation of the topmost atoms (*70, 71*).

Zhang et al. (*66*) did DFT calculations on the ZnO(0001) and ZnO(000-1) surfaces in vacuum and found that neither surface reconstructs (i.e. (1×1) surfaces), but that both surfaces tend to relax inward. The contraction of Zn terminated surface was calculated to be much smaller than the O terminated one and the surface energies were calculated to be slightly higher for the O terminated surface than the Zn terminated one. They use a six layer slab model where layer five and six are held fixed.

Na et al. (*67*) did surface energy calculations that are comparable with the energies found by Zhang. et al. (under the assumption that Zhang et al. has a misprint in the choice of units of the surface energy). However they did not calculate a specific surface energy for each surface, as they expected the energy of each surface to be half of the energy required to cleave the crystal due to the similar geometry of these surfaces.

In the presence of hydrogen Ito et al. (*5*) have calculated that the O terminated surface is more stable than the Zn terminated one. The most stable configuration of hydrogen on the O terminated surface was found at ½ ML coverage of hydrogen, while for the Zn terminated one, the most stable configuration was calculated to be at ¾ ML coverage.

During the extent of this work, there have been several publications on these surfaces; however to the author’s knowledge there are no reports of these surfaces in Zn atmosphere.

4 Experimental

4.1 The Growth of ZnO and ZnS Single Crystals

Chemical vapour transport was selected as the method for synthesizing ZnO and ZnS single crystal substrates. This method requires relatively low temperatures and still produces the crystals with the least amount of impurities. Data from Table 1 show that the only significant impurity to be expected is silicon from the ampoule walls.

For the transport agent, there were several criteria that were considered. Traditionally iodine has served as a transport agent for both growth of ZnO and ZnS, however due to its high vapour pressure, sealing an ampoule with iodine can be a complicated process and there have been numerous reports of growth of both ZnO and ZnS with chemicals that are easier to handle due to lower vapour pressure at room temperature as well as lower toxicity. NH_4Cl is one such compound as it is also a powder at room temperature and is basically harmless. In addition it has previously been reported to result in high growth rates of ZnO (*53*). Upon heating it acts as HCl and NH_3 (which in turn decomposes to N_2 and H_2), which reacts with ZnS in the following ways (*53, 59*):

$$ZnS(s) + 2HCl(g) \leftrightarrow ZnCl_2(g) + H_2S(g) \qquad \text{Eq. 22}$$

$$ZnS(s) + \frac{2}{3}\mathrm{NH}_3(g) \rightarrow Zn(g) + \frac{1}{3}\mathrm{N}_2 + H_2S(g). \qquad \text{Eq. 23}$$

The last reaction is not reversible, however the transport continues with the following reaction:

$$Zn(g) + H_2S(g) \leftrightarrow ZnS + H_2. \qquad \text{Eq. 24}$$

This way hydrogen may be considered the transport agent for ZnS in this case.

The reaction with ZnO similarly yields:

$$ZnO(s) + 2HCl(g) \leftrightarrow ZnCl_2(g) + H_2O(g) \qquad \text{Eq. 25}$$

$$ZnO(s) + \frac{2}{3}\mathrm{NH_3}(g) \rightarrow Zn(g) + \frac{1}{3}\mathrm{N_2} + H_2O(g). \qquad \text{Eq. 26}$$

The reaction in Eq. 26 then continues analogous to Eq. 24.

Ampoules were prepared using quartz tubes with wall thickness of 2 mm and an inner diameter of 15 mm. The lengths of the ampoules are ~15 cm, so the total volume of an ampoule is ~26.5 cm^3. The quartz tubes were first sealed in one end using a hydrogen torch and the other ends were sealed at a later point after the correct amounts of reactants were placed in the ampoule.

A measure that was taken in order to obtain as chemically pure crystals as possible and to avoid the Si contamination, which is the only significant impurity expected for growth of ZnO and ZnS by chemical vapour transport, was to coat the quartz ampoules with zinc in order to produce amorphous Zn_2SiO_4 which is stable up to high temperatures or possibly ZnO, which also would prevent silicon impurities. This should thus ensure that there are no significant impurities in the resulting crystals. The reaction that is expected to take place is:

$$2Zn(s) + SiO_2(g) + O_2 \leftrightarrow Zn_2SiO_4, \qquad \text{Eq.27}$$

although it is even more likely that Zn will be oxidized before it reacts with the SiO_2, and thus the walls will be coated with ZnO. This should not be a problem for the ZnO crystals, but could affect the crystallinity of the produced ZnS.

The coating was first made by placing 3-4 shots of pure zinc (99.9998%, Goodfellow LS353023) with a mass of 0.2-0.3g in an ampoule and then heated under vacuum with a hydrogen torch. This worked out poorly however, and a different method in which the ampoules were heated in a temperature gradient in a furnace without establishing vacuum was chosen. A range of different temperature gradients ranging from 870-940 °C at the hot end from 500-750 °C at the cold end were applied in order to establish which temperatures resulted in the smoothest layer. The bottom of the ampoule was positioned at the hot end, with the three zinc pellets as close to the bottom of the ampoule as possible. Diffusion of too much zinc out of the ampoule was prevented by sealing the open end with quartz wool. The ampoules were kept in the furnace for different time durations ranging from two to four days. In order to facilitate whether a layer of Zn_2SiO_4 had been formed, a silicon substrate was put roughly in the middle of the ampoule, which later was characterized by AFM, SEM, XRD and ellipsometry. It is assumed that some of the silicon substrate was oxidized during the coating process and thus it is likely that the reaction between the substrate and the sublimated Zn will be similar to the one between Zn and the quartz walls. Analysis of the quartz wool, which consists of SiO_2, could also give an indication whether Zn will react with the ampoule.

The first ampoules that were used in order to do the chemical transport reaction were filled ZnO powder with a purity of 99.999% (Sigma-Aldrich, CAS: 1314-13-2) in one ampoule, and ZnS with a purity of 99.99% (Sigma-Aldrich, CAS: 1314-98-3) in another. Powder of NH_4Cl (99.9995%, Sigma-Aldrich, CAS: 12125-02-9) was added to each ampoule according to Table 2. The amount was selected in order to keep the internal pressure in the ampoule at 3-4 bars (see Appendix II for calculation). The ampoules were sealed under vacuum by using a hydrogen torch, and vacuum was confirmed with an electrostatic vacuum tester.

The ampoules were positioned in a furnace with a temperature gradient ranging from 900 °C in one end, to 880 °C in the other and with the feed material positioned near the hot end. After 14 days, the ampoules were taken out of the furnace and opened. The resulting crystals were taken to ESRF and were analyzed by SXRD with a MAR345 area detector and a wavelength of 0.7 Å was used.

Table 2: Amounts of material used for the CVT of ZnO and ZnS for 14 days with a temperature gradient of 800-900 °C.

ZnO Ampoule	ZnS Ampoule
ZnO: 0.9965g	ZnS: 1.0242g
NH_4Cl: 0.0183g	NH_4Cl: 0.0190g

After the results of the first transport reactions were confirmed, a new ampoule was prepared with chemicals according to Table 3. The ampoule was first kept in the furnace for 14 days with a temperature gradient of 940-950 °C. The feed material was positioned at the hot end in order to transport any remaining powder on the ampoule walls and at the cold end over to the hot end. The temperature gradient was changed after 14 days and the ampoule was kept in the furnace for an additional 23 days. The resulting crystals were investigated with an optical microscope, both with and without a polarization filter and a scanning electron microscope in both low and high vacuum mode.

Table 3: Amounts of material used for the CVT of ZnO for 37 days with a temperature gradient of 940-950 °C.

ZnO	0.989g
NH_4Cl	0.017g

4.2 Thermodynamics of ZnO and ZnS Growth

4.2.1 Determining Transport Direction

In order to find the transport direction, theoretical calculations were carried out with the HSC chemistry software. This program may be used in order to find the possible species that will be present in a reaction and their partial pressure, given the amount of starting materials, the temperature and the pressure at which the reaction takes place. The program uses thermodynamic values according to Appendix III.

The average pressure P in the ampoule is given by the ideal gas law:

$$P = \frac{nRT}{V}, \quad \text{Eq. 28}$$

where n is the amount of gas species in mol in the ampoule, R is the gas constant, T is the average temperature in the tube and V is the volume of the ampoule. The pressure in the middle of the ampoule for both the transport of ZnO and ZnS is calculated to be 3.43 Atm for the first experiment, while 3.59 for the second transport experiment of ZnO (see Appendix II).

Previously, the transport of ZnO with HCl as the active transport agent has been reported as being exothermic (*72*). Figure 14 shows the calculated activity (normalized) of each possible gas species in the transport of ZnO. The activity of $ZnCl_2$ is higher than Zn at temperatures below 1150 °C and this could be an indication that HCl is the transport agent that dominates the transport of ZnO at the temperatures used in this study, although H_2 will also either contribute or slow the transport and thus further investigation is needed.

In order to find the transport direction, the change of the activity of $ZnCl_2$ and Zn needs to be evaluated as it is only the change in partial pressure which has any significance on the transport. It is clear that the activity of Zn is increased once it starts sublimation at 880 °C and the partial pressure of Zn will consequently be large in the hot area. Diffusion of Zn will thus be from hot to cold. The activity of $ZnCl_2$ is reduced as the activity of elementary Zn increases at the selected temperature range (880-900 °C and 940-950 °C). Due to the negative activity gradient the transport of $ZnCl_2$ will be from cold to hot at the experimental conditions, i.e. different from the direction of elementary Zn. The gradient of the activity of $ZnCl_2$ appears to be quite similar or possibly lower than that of elementary Zn, and finding the dominating transport agent just from these data is quite complicated. Figure 15 reveals that the activity gradient of $ZnCl_2$ is negative at temperatures above 870 °C; however the change in activity is very small for the first experiment that was carried out. The second experiment was done with a smaller temperature gradient, but in an area where the gradient falls off at a higher rate. The increase in partial pressure of Zn is also higher at this temperature range and as the activity of Zn is fairly sensitive to the input parameters, it is impossible to say for sure which transport agent will be the dominating one before carrying out an experiment.

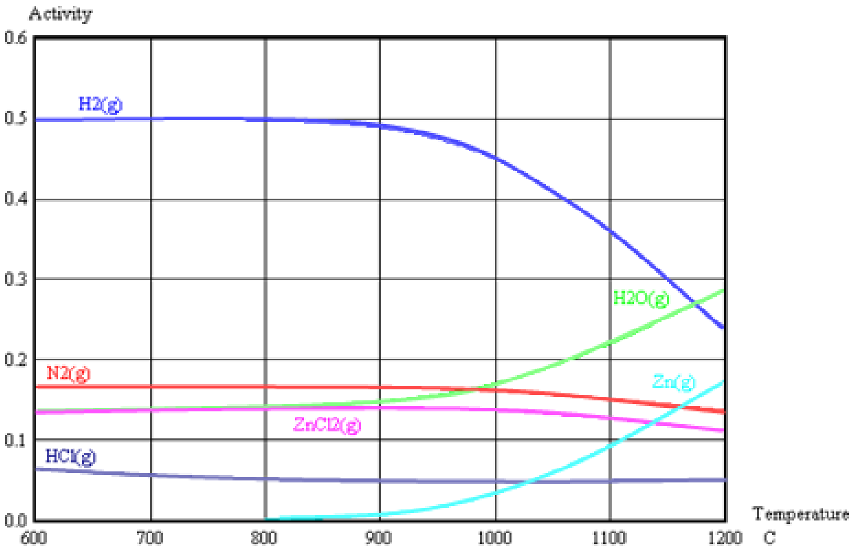

Figure 14: Calculated activity (partial pressures) of possible gaseous species during the chemical vapour transport of ZnO with NH_4Cl as transport agent at temperatures 600-1200 °C.

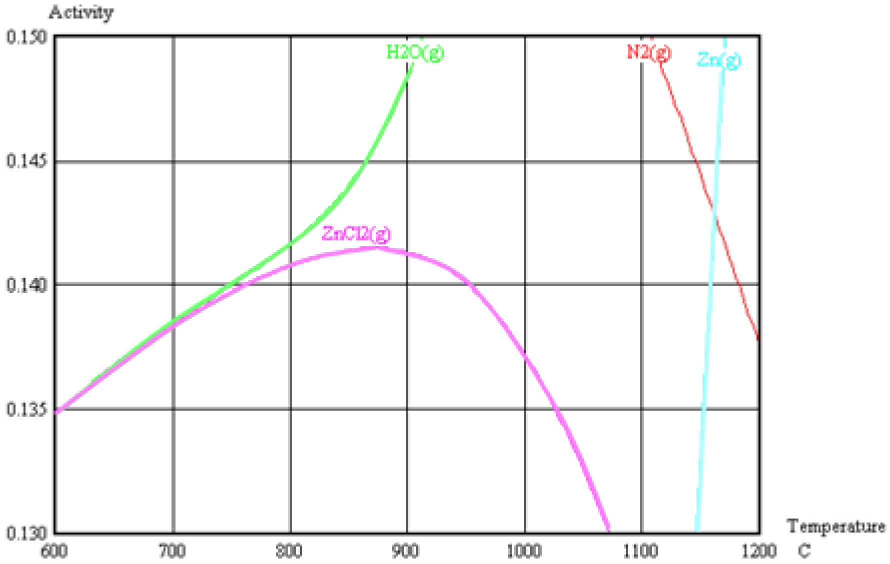

Figure 15: A closer inspection of the activity of $ZnCl_2$ reveals a decrease in partial pressure after 870 °C, which indicates that the transport direction will be from cold to hot in the temperature range given that $ZnCl_2$ is the dominating transport agent.

Figure 16 shows the activity of the possible gaseous species during the transport of ZnS. The activity of $ZnCl_2$ is also in this case higher than for elementary Zn (which can be neglected in this case), suggesting HCl to be the dominating transport agent. The activity of $ZnCl_2$ is steadily increasing with the temperature over the whole temperature range, suggesting that the transport will be from hot to cold.

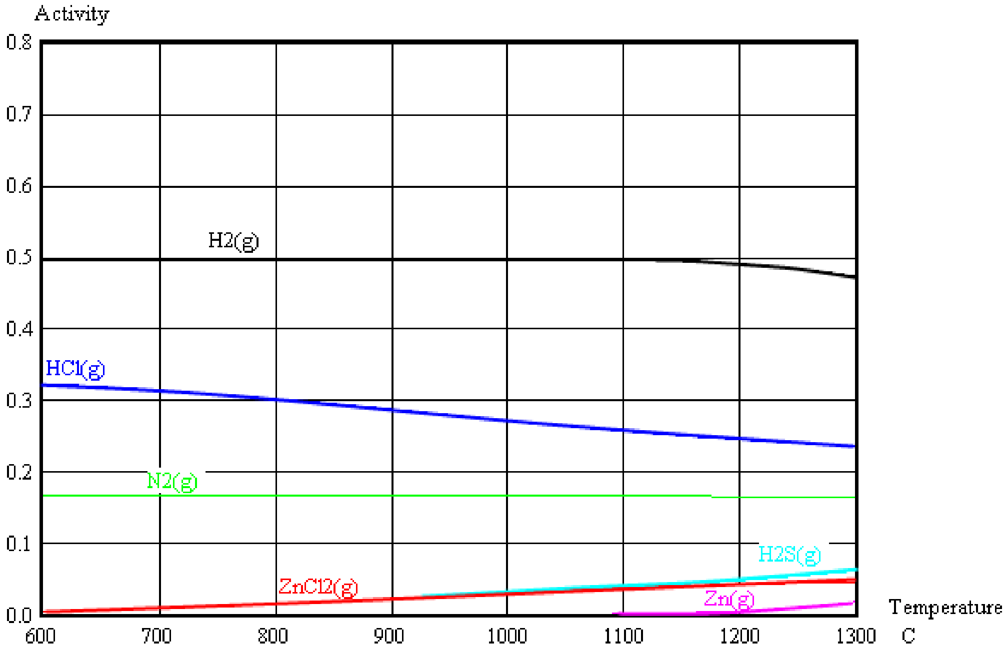

Figure 16: The calculated activity of possible gaseous species during the chemical vapour transport of ZnS using NH_4Cl at transport agent.

4.2.2 Determining Growth Rates

In order to determine the growth rates, the following equilibrium should be considered:

$$i\,A(s) + \ k(B)g \ \leftrightarrow j\,C(g) \qquad \text{Eq. 29}$$

It possible to calculate a theoretical estimate of the transported mass in the reaction by using the following equation (derivation and calculation in Appendix IV)(*73*):

$$n_A = \frac{i}{j}\frac{\sum P_0\,\Delta P_A}{\sum P}\frac{T^{0.8}D_0qt}{sRT_0^{\ 1.8}} \cdot 10^{-3}(\text{mole}) \qquad \text{Eq. 30}$$

The symbols in the equations are explained in Table A.1 in Appendix V. For the transport of ZnO in the temperature gradient of 940-950 ° C, the calculated result is that 0.05 g is transported with $ZnCl_2$ over a period of 23 days. This is much lower than desired, but given the results obtained, the value is likely to be underestimated by a factor of 10, which is mainly attributed to the change in partial pressure being unrealistically low. If the calculations are correct, the growth rate given a transport period of 23 days should be 0.091 mg/hour or 2.2 mg/day.

For the transport of ZnS, the calculations in Appendix V give a transport of 0.26 g given the conditions stated in Chapter 4.1. With the transport being carried out for 14 days, the theoretical growth rate should thus be ~19 mg/day.

4.3 Experimental Setup for SXRD

In order to analyze the thin films, a setup similar to low angle diffraction is used in which the sample is aligned parallel to the incident beam as shown in Figure 17. The experiments are carried out on a KM6-CH-type diffractometer, delivered by Oxford Diffraction. To obtain the correct sample height, the holder is adjusted so that the shadow of the substrate can be seen on a CCD-camera and ensures that the beam hits the sample. The holder is mounted on a goniometer head, which in turn is positioned on a six axis goniometer. The sample is fastened to the holder by the use of double sided adhesive tape. The axes used in this experiment are labeled ω, φ, θ and κ. The ω axis is used to adjust the tilt of the sample, while the φ adjusts the in plane rotation. The θ axis is used to move the detector. The κ axis is shown in Figure 18

(*74*) and lies in the plane spanned by $\mathbf{e_1}$ and $\mathbf{e_3}$, with an angle of 45 ° on both $\mathbf{e_1}$ and $\mathbf{e_3}$. The $\mathbf{e_2}$ axis is pointed towards the reader.

The alignment of the film is done by using a laser pointed at an angle down on the film and then reflected at a wall or screen, positioned ~2 meters from the sample. By rotating the sample first 180 ° around the φ axis and tracking the change in the reflection of the laser, the goniometer head can be adjusted so that the laser point converges to a point in the middle of the two measured reflections. Rotating the sample back 90 ° and then doing a new 180 ° φ rotation and adjusting the goniometer head, so that the reflected laser hits the same spot, will result in the reflected spot staying stationary when the sample is rotated 360 ° around the φ axis. The alignment is also done in a similar way for the κ axis. The axis is rotated from 0 ° to 90 ° and then from 90 ° to -90 ° and the laser is aligned in a similar fashion. Having done both these alignments correctly, ensures that the beam will always hit the same spot and that scattering from identical planes in the crystal will be scattered to the same point on the detector, which is at a distance of 250 mm, which is much closer than the wall or screen used for the alignment. Thus any small errors in the misalignment will become less pronounced. Increasing the detector distance will however increase the resolution.

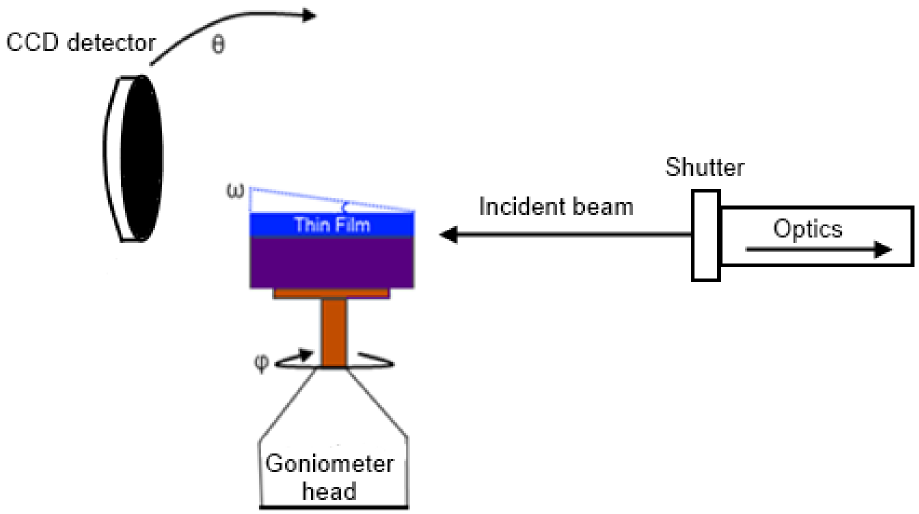

Figure 17: Schematic setup for thin film X-ray diffraction analysis viewed from the side.

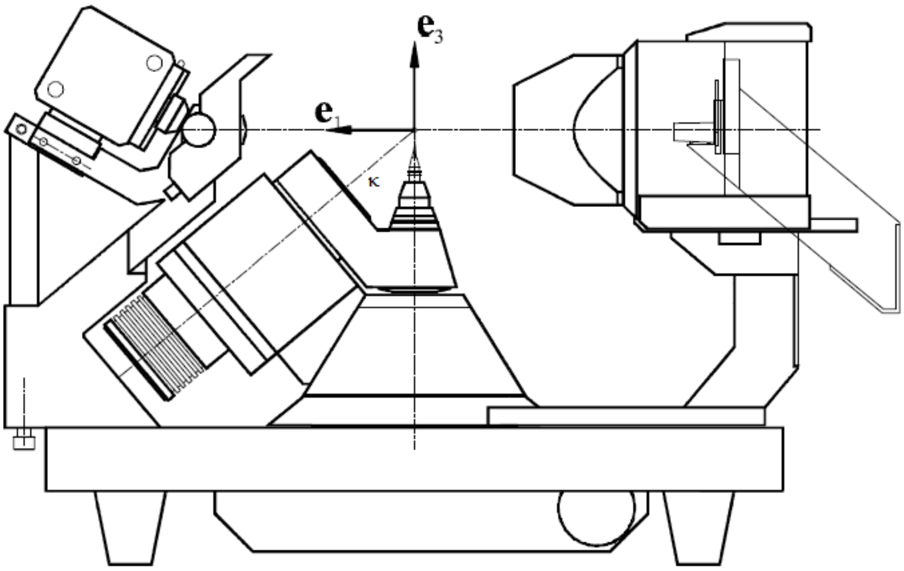

Figure 18: Side view of experimental setup of the KM4CCD system (*74*). The laboratory reference system is shown with bold vectors. The κ axis lies in the $\mathbf{e}_1$–$\mathbf{e}_3$ plane as indicated by a black line on the figure. The invisible $\mathbf{e}_2$ axis is directed towards the reader. The instrument used in this study is a newer model; however the κ axis is the same.

The beam itself is sent through an optics section where various mirrors and slits can be employed in order to shape the beam. For thin films, a beam size with a height of ~150 μm and a width of ~800 μm is usually employed, although a smaller beam size would be desirable. This rectangular shape of the beam reduces the intensity obtained from the substrate. A monochromator is also used, which for thin film measurements selects wavelengths of typically ~0.7 Å. In most cases a filter which reduces the intensity of the beam is also employed. This is needed to avoid overexposure which results in very bright spots that are impossible to interpret and may shadow other reflections. Various thicknesses are available or can be made on demand, but for thin films, filters with thicknesses of Cu ranging from 50-250 μm are usually employed. The filter used depends a lot on how well the sample scatters and thus needs to be selected specifically for each sample. Finally a moveable shutter is in place that can prevent the beam from hitting the sample. The shutter can open and close in less than a second and is used in order to generate a dark current map, which is used as a calibration. While the shutter is closed, any photons that hit the detector are counted and subtracted from the final image in order to reduce noise.

4.3.1 Thin Film Measurements

The thin film is first scanned ~12° around the ω axis with a step size of 0.25-0.5° with an exposure time of minimum one second per degree in order to find the tilt where you obtain the most reflections from the film with a decent intensity. The angle which is found is then used for a panorama scan, which is a 180° rotation around the φ axis. A step size of 0.25° is usually enough to get all the desired information, although depending on how much time is available, lower step size will result in better resolution and could give additional reflections. With a step size of 0.25°, most experiments will be done in less than an hour. Should the CCD camera become overexposed, a new image will be taken with reduced exposure time and if the selected filter is too weak or certain reflections scatter too strongly, the experiment will take much longer, as most images will be taken twice.

After the scan in complete, software is employed in order to search for diffraction spots above a certain intensity. These are then used to reproduce a 3-dimensional reconstruction of the sample in reciprocal space, which can be used to index the thin film and substrate in order to find an orientation matrix. The orientation matrix tells the software how the film is oriented and can thus by simple input adjust all the angles of the goniometer in order to analyze a specific reflection. This can in turn be used to compare intensities of various reflections or to do high resolution scans of the peaks in order to observe effects like Bragg satellites or peak splitting. Comparing intensities must be done with caution however, as the actual broadening of the peak may be a result of slight misalignment of the sample. This can be remedied if needed by rotating the sample 180° and doing a new scan. By comparing the full width at half maximum (FWHM) of the desired reflection from both scans, it is possible to find the actual midpoint of the reflection and it is possible to calculate the actual FWHM. This procedure has not been carried out in this study, and thus only qualitative data can be obtained from the intensities. Bragg satellites are a result of high intensity X-ray diffraction from crystalline surfaces or interfaces. When X-ray diffraction of a crystal with a flat surface is measured in detail, a diffuse, line-like distribution of the X-ray intensity around a Bragg reflection is observed. This is called crystal truncation rod (CTR) scattering, and is a result of the abrupt truncation of the periodicity of a crystal, which causes a delta function like distribution of the X-ray intensities. Oscillations in intensity along the rods are called Bragg satellites and can be used to find information about the atomic structure of the surface or interfaces, the thickness of the layer and to make estimates about the concentration of compounds in the layer (*75, 76*).

4.4 Modeling the ZnO(0001) and ZnO(000-1) Surface

The polar surfaces of ZnO have been investigated under various conditions in this study using DFT. The bond length contraction of the first layers of both these surfaces as well as the surface energy was calculated without any adsorbates present. This was done in order to reproduce the (1×1) surface from literature (*77*) and to compare results with previous work in order to know the validity of the calculations. As charged polar surfaces are inherently unstable and expected to undergo surface reconstruction to maintain electrostatic stability, one would expect severe reconstruction of the ZnO surface. That is however not the case and several studies have been done in order to explain the stability of these surfaces (*78*, *79*). The surface energies of the specific surfaces in various atmospheres is not something very well investigated, although there is an increasing interest in this area and there are several experimental results that show that the O terminated and Zn terminated faces have different reactivity (*79*). The surface energy is defined as half the energy created upon creating two cleaved surfaces. Usually two such surfaces have the same properties, but due to the polarity of the ZnO(0001) and ZnO(000-1) surface, these surfaces do not and thus it is of interest to find out which surface is the most stable under various conditions.

The surfaces were calculated with varying coverage of adsorbed O and Zn on the surface. The coverage of the surfaces usually has a large impact on the surface structure and finding the surface structure for all coverages is an endless task. By creating a 2×2×3 supercell there will be four unit cells on the surface, which in theory makes it possible to find the surface structure for coverages of one quarter, one half, three fourths and a complete mono layer (ML) of the adsorbate. In this work, coverages of one quarter, one half and a whole mono layer were considered and should be enough to be able to identify a general trend. Note that a quarter ML of O_2 implies a half ML of dissociated O atoms. For this reason a quarter ML of O atoms was not investigated as that would require a much larger supercell. On the other hand, half a ML of O_2 corresponds to one ML of dissociated O atoms, and thus a higher coverage of O_2 was not investigated either.

There are a large number of sites that a molecule can adsorb on each surface, and testing every single one requires a huge amount of work. On each surface with each adsorbate, around 20-30 configurations have been tested, and close to a 100 all in all, but upon relaxation most of the tested configurations will relax to a select few and only these will be presented in this work. Even though quite a large number of different sites have been tested for each adsorbate, it is still possible that there are configurations with lower energies than the ones found in this work. The chance of the calculated configurations with lowest energy being the ground state is however considered to be very high, especially close to 0 K.

Due to the large number of parameters, it is not common to use the calculated energy directly for each structure as this is usually not very precise for such large systems. Instead structures are compared with some reference energy. In this work, a calculation was done for all structures where the adsorbed molecule(s) was as far away from the surface as possible given the vacuum thickness and this calculated energy was then used as set-point energy for the system. All the other energies with an equal amount of molecules were compared with this “unbonded” configuration, in order to determine if it is desirable for a molecule to adsorb to a specific position, or if the system has a lower energy if the molecule is not bonded to that site at all. As long as all calculations are done with the same parameters, this will also ensure that any errors will be cancelled and thus greatly improve the accuracy of the calculations.

4.4.1 Computational Methodology and Convergence

The calculations in this work have been done using DFT. The approximation to the exchange correlation potential has been done using a Perdew-Wang 1991 (PW91) functional as implemented in the CASTEP and DMol-3 code. The functional is based on ultrasoft pseudopotentials using the GGA. The parameters were chosen to be as close as possible to previous work in order to be able to compare the results. For this reason a six layer slab was used, as well as a 12.5 Å vacuum thickness, even though increasing the vacuum thickness has little consequence for the computational time using the DMol-3 code. Zhang et al. tested 13.8 Å vacuum thickness but found that this had no consequential impact on the results compared to 12.5 Å and thus this was used. The ***k*** point density was set to one along the *c* axis as this axis is very long and thus the lattice vector in reciprocal space will be a short one. The density along the other axis was then determined by the inverse of the lattice parameters in those directions.

The calculations have been done using a global orbital cutoff of 4.4 Å and a 4×4×1 Monkhorst-Pack mesh is used for the Brillouin zone integration. This is considered to be relatively precise in DMol-3. A list of all the parameters used is shown in Table 4.

The CASTEP code was only used initially to relax the bulk unit cell, as this uses little computational power for highly symmetric systems. For all other calculations the DMol-3 code was used. The convergence criteria are what determine when the calculation is complete. When a step in the calculation is done, the energy, force and displacement is compared with the values in the previous step, and if the difference is sufficiently small, the calculation is complete. Should one of the convergence requirements not be met, then another attempt will be done using the Kohn Sham equations and the variation principle. The chosen convergence parameters are not extremely strict, but as limited time was available and the results of interest are comparisons between different surface structures, the results should be accurate using these parameters.

Table 4: Overview of parameters used for the following DFT calculations on ZnO using the DMol-3 code. Note that 1 Ha = 27.2116 eV

XC-functional	PW91-GGA
Supercell size	2×2×3
k-point density	4×4×1
Global orbital cutoff radius	4.4 Å
Convergence of total energy	$1E^{-5}$ Hartree (Ha)
Convergence of forces	0.003 Ha/Å
Max displacement	0.005 Å
Basis set	Double numerical plus d-functions (DND) (basis file 4.4)
Core treatment	All electron
Electronic smearing	0.01 Ha
Vacuum thickness	12.5 Å
Multipolar expansion	Octupole

5 CVT Results

The following chapter will contain results about the experiments related with the chemical vapour transport of ZnO and ZnS. The outcome of the coating process will be presented first, followed by actual results of the CVT experiments and characterization of the synthesized crystals.

5.1 Coating of Ampoules - Results

The coating of the ampoules when done by hydrogen torch under vacuum resulted in deformation of the ampoule walls, and it was impossible to coat the whole ampoule evenly. By placing the ampoule in a furnace with a temperature gradient, and with the Zn shots at the hot end, the coating became even and transparent on the ampoule walls and the Si substrate appeared to have a smooth thin film. Several experiments were done, and in some cases the quartz wool that was used to stop the sublimated Zn to merely diffuse out of the ampoule contained a lot of yellow powder. The top of the ampoule had also a yellow fluorescent glow, suggesting that the diffusion of Zn through the ampoule was perhaps too fast and that most of the Zn powder was rather transported to the quartz wool and oxidized to ZnO. The quartz wool might be a better representation of the ampoule than the Si substrate as the Si substrate will only have a very thin layer of SiO_2 at this temperature. That the quartz wool exhibited a yellow fluorescent glow suggests that it did not react with Zn and probably formed ZnO, as yellow fluorescence is a characteristic of ZnO above a certain temperature (*80*). It is however possible that the Zn was already oxidized before reaching the quartz wool and hence did not react. Another possibility is that a layer of Zn_2SiO_4 was formed and any surplus of Zn on this surface is likely to become oxidized as Zn_2SiO_4 is inherently stable.

In one case, three ampoules were put in the same furnace at the same time. Two of the ampoules were put at the bottom of the furnace, while the last one was positioned right on top of these. The two ampoules at the bottom had no powder in the quartz wool and some of the Zn pellets still remained at the bottom of the ampoule. The one positioned on top had no Zn pellets remaining however, and a quite significant amount of powder was present in the quartz wool. The shading of the film on the Si substrate was also uneven. The other substrates were however covered with even thin films with uniform yellow-green shading. The repeated process, which was carried out over four days instead of two, resulted in all the substrates being evenly coated and all had still some Zn pellets remaining. A final experiment where three ampoules were kept in the furnace for just 1 day with a source temperature of 930 °C resulted in all the Zn pellets sublimating completely and even films of roughly 150 nm were produced. The process is thus quite sensitive to unknown parameters and it was not possible to determine the precise conditions that result in most of the Zn diffusing to the other end of the ampoule or exactly how this affects the film thickness as both even and uneven films were produced.

In order to obtain precise information on the film roughness, AFM (Figure 19) and SEM analysis was performed of the surface. Both the image obtained by the AFM scan and SEM scan revealed an almost atomically flat surface.

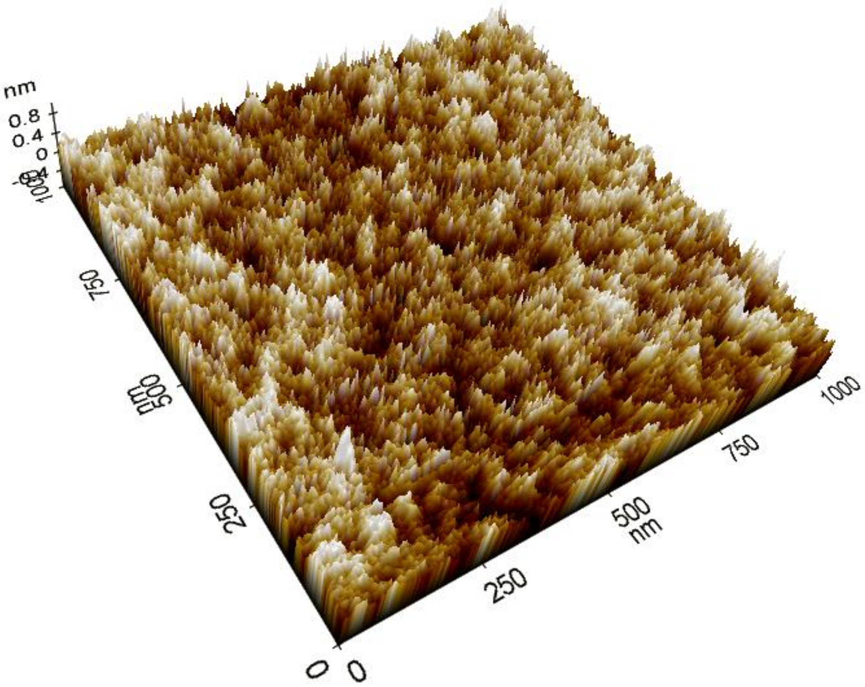

Figure 19: AFM image of the Si-substrate after the coating process. The height scale of the image is less than 1 nm implying that the film is atomically flat.

In order to know if a film had been deposited, the Si substrate was studied with ellipsometry before and after the coating process. Figure 20 shows data of the Si substrate before deposition. The fit is not particularly good, but the software suggests a SiO_2 layer of ~5 nm on top of the Si substrate.

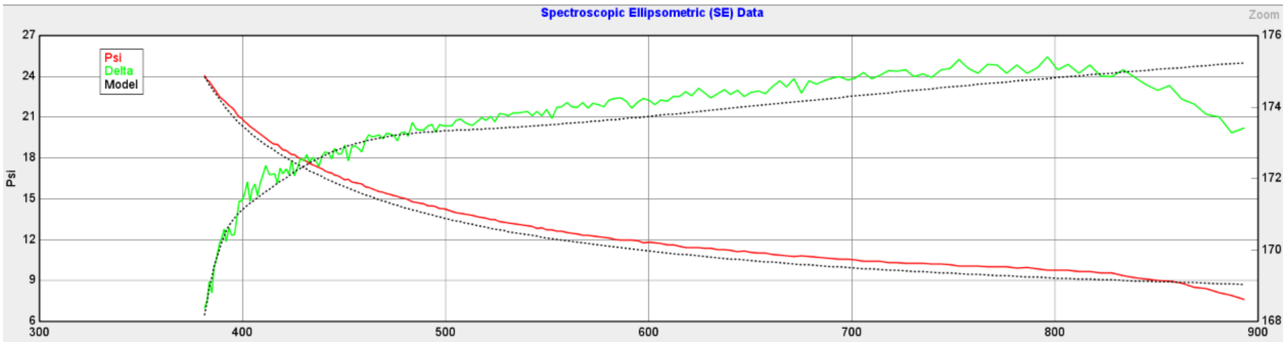

Figure 20: Ellipsometry data of a Si substrate. The software suggests a SiO_2 layer of ~5 nm.

Figure 21 shows ellipsometry data of a substrate being subjected to a temperature gradient of 940 °C in the hot end, to 750 °C in the cold end for two days. While not a perfect fit, it is clear that a film has been deposited and that the thickness is somewhere between 175-200 nm.

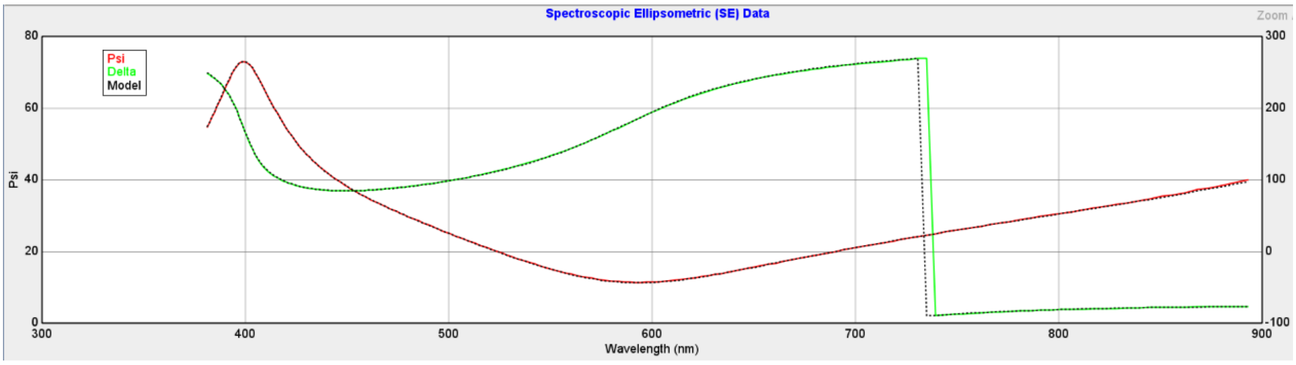

Figure 21: Ellipsometry data of Si substrate after being subjected to a temperature gradient of 940 °C in the hot end, to 750 °C in the cold end for two days. The software suggests a film thickness of 150-250 nm.

Ellipsometry data for a substrate after being subjected to a different temperature gradient (875-500 °C), but for the same time duration, is shown in Figure 22. The ellipsometry model used provided a perfect fit and the thickness was measured to be 375 nm.

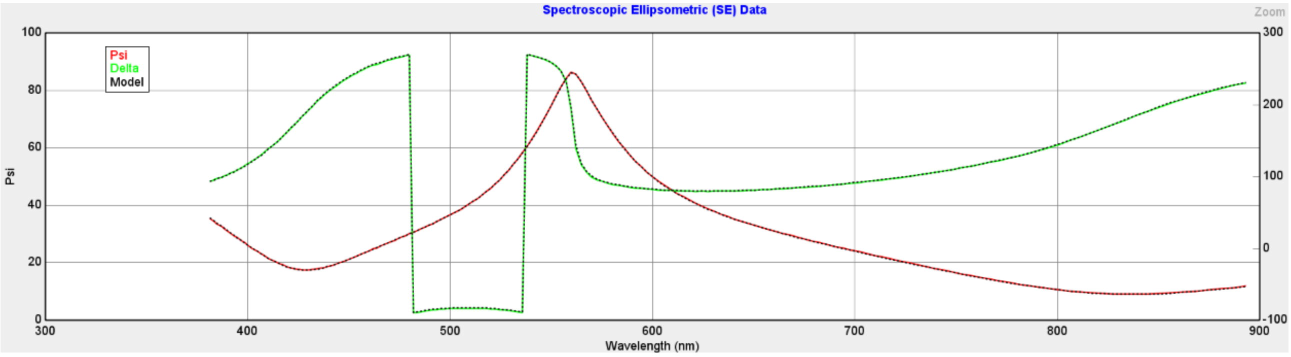

Figure 22: Ellipsometry data of Si substrate after being subjected to a temperature gradient of 875 °C in the hot end, to 500 °C in the cold end for two days. The software suggests a film thickness of 375 nm.

Increasing the time duration from two to four days did not affect the film thickness, i.e. the three samples measured had all film thicknesses ranging from 365-375 nm.

XRD of the coated Si substrates was carried out in order to get an indication of whether Zn_2SiO_4 actually had been formed. The only crystalline species in the resulting diffraction patterns was the Si substrate, indicating a lack of formation of a crystalline phase. Under the coating conditions, Zn_2SiO_4 is expected to become amorphous, and consequently this was anticipated, however to get an indication of whether Zn_2SiO_4 has been formed, the sample was analyzed by X-ray fluorescence (XRF); however this did not give any useful information apart from the fact that Zn is present in the sample. A more suitable method would have been X-ray photoelectron spectroscopy (XPS), this was however not prioritized.

5.2 CVT of ZnO – Results

The ZnO crystals that were grown for 14 days in a temperature gradient ranging from 900-880 °C were not transported to the cold end, but instead they were compressed at the hot end of the ampoule, which indicates that an endothermic reaction took place. This is not in agreement with the theoretical calculations. The scent of chlorine was strong when the ampoules were broken, however no characteristic smell of ammonia was noted, which likely suggests that ammonia decomposed to hydrogen and nitrogen gas.

The ZnO crystals produced were transparent and polycrystalline with single crystals domains of around 0.5 mm^3. A complete area diffraction pattern obtained by a MAR345 2D-area detector at the BM01A station at the SNBL (Figure 23) indicate that the grown crystals are of good structural quality. The inspected single crystals were around 100 μm and were selected using an optical microscope with a polarization filter.

The ZnO that was grown in the furnace for 23 days (after 14 days of back transport) with a temperature gradient ranging from 940-950 °C had single crystal domains of up to 2 mm^3 and were also transparent and of varying crystal quality. The transport in this case was also endothermic, which this time was expected due to the previous experiment, however it still does not agree with the theoretical calculations performed.

It was estimated that around 2/3 of the starting material was transported. However as the crystals are grown on the ampoule walls and most of them are difficult to remove without risk of destroying them, the mass was not measured. Given that a tiny amount of the starting material was lost during the sealing process, it is estimated that ~0.5 g was transported. This corresponds to a growth rate of 21.7 mg/day, which is a factor 10 higher than was calculated in Appendix IV.

The crystals were inspected in an optical microscope, both with and without a polarization filter (Figure 24), which makes use of the fact that crystals with different orientations diffract and reflect polarized light differently and thus makes it possible to determine if the crystal is twinned or single crystal. In addition to roughly 20 regularly shaped crystals, several needle shaped crystals were also found with lengths of roughly ~0.3 mm.

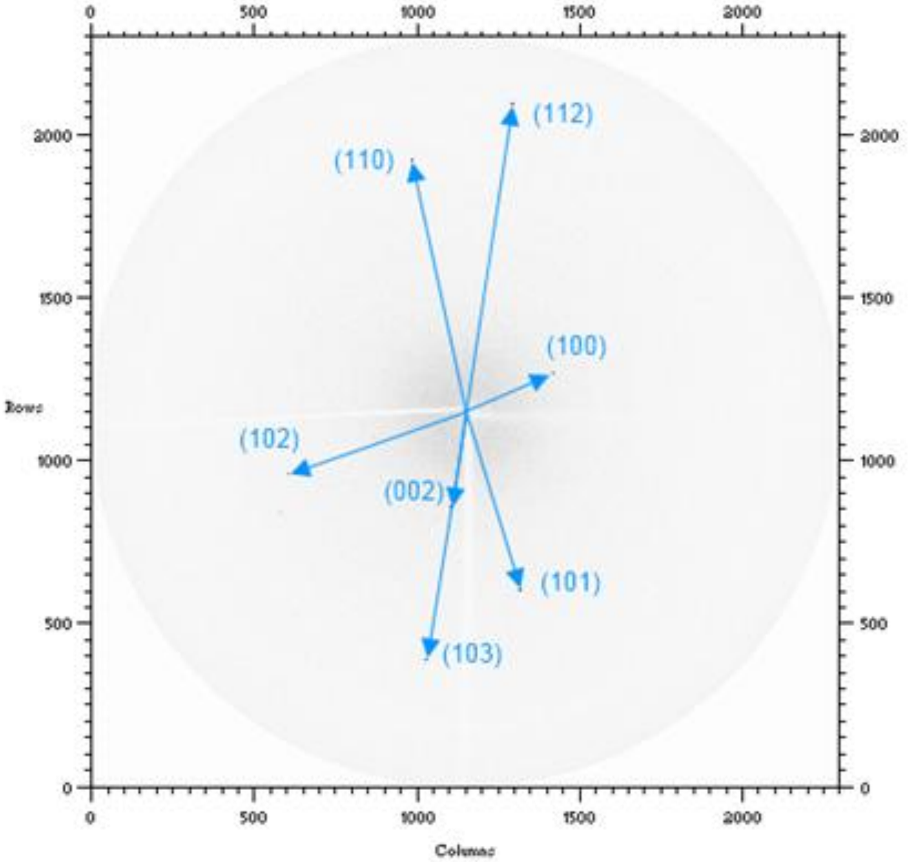

Figure 23: Area diffraction pattern of ZnO grown by CVT. The well resolved diffraction spots indicate high structural quality. The rows and columns are pixels on the detector, and given the detector distance (250 mm) and the wavelength of the beam (0.7 Å), the values may be used to calculate the *d*-spacing of the planes. A point in the middle of the plate represents planes separated infinitely far away from each other, while a point at the edge represents planes with a distance *d* = 1 Å.

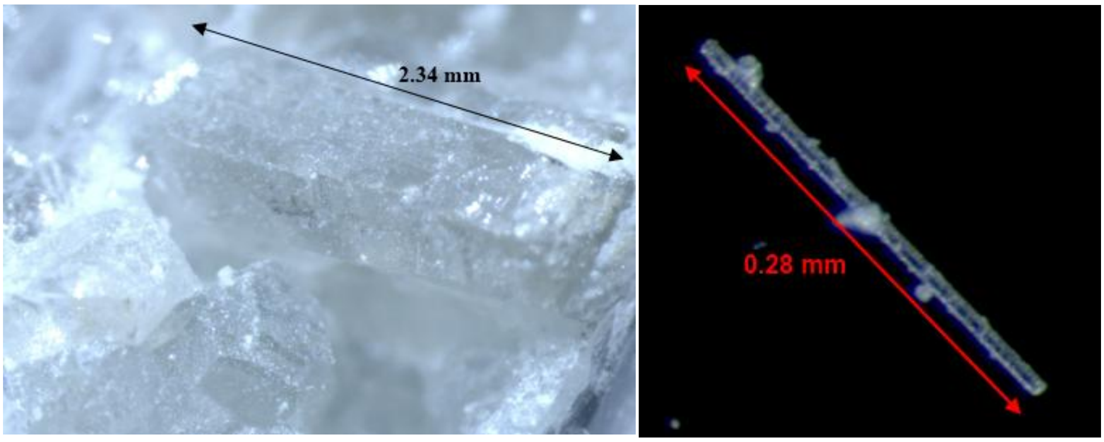

Figure 24: ZnO crystals grown by CVT. The left image is taken in an optical microscope with a polarization filter, while the image to the right is taken without.

The crystals were also inspected with SEM (Figure 25). Several crystals of varying sizes are visible and most of the crystals appear to be polycrystalline. Figure 26 shows a closer inspection of some of the crystals that were possible to extract from the ampoule walls. It is apparent that both crystals with smooth and rough surfaces were produced, although most of the larger ones have smooth crystal faces. Figure 27 shows a close up image of one of the smooth crystal faces of the crystal to the right in Figure 26. The crystal face is stepped and is roughly 1 mm^2. A lot of particles are also present on the sample surface. That most the particles exhibit a darker contrast on the image obtained by the SSD detector, suggest that the particles have a different chemical composition than the crystal.

EDS analysis of the crystal face in Figure 28, indicates very few impurities. A small peak of Al (<1 At %) was present in the spectrum, however as there was no Al present under the synthesis and the peak is quite small, it is impossible to draw any conclusions from it. The peak is slightly shifted from an expected Si peak, which would be the most likely impurity to be present in the crystal as the crystals were transported in a small glass container. The software did not recognize Si as one of the possibilities however and Al was consequently removed from data set. The composition of the crystal given by the EDS analysis can be seen in Table 5. The composition is found to be close to Zn_4O_3, although it is commonly observed that the atomic quantity of O is lower than the actual values found by EDS if operated in low vacuum. As ZnO is semiconducting with a relatively large band gap, low vacuum was needed in order to avoid charging and this decreases the detection sensitivity of lighter elements. Oxygen vacancies in ZnO also tend to colour the crystals orange, which was not observed for the produced crystals. The actual composition is thus likely to be much closer to 1:1.

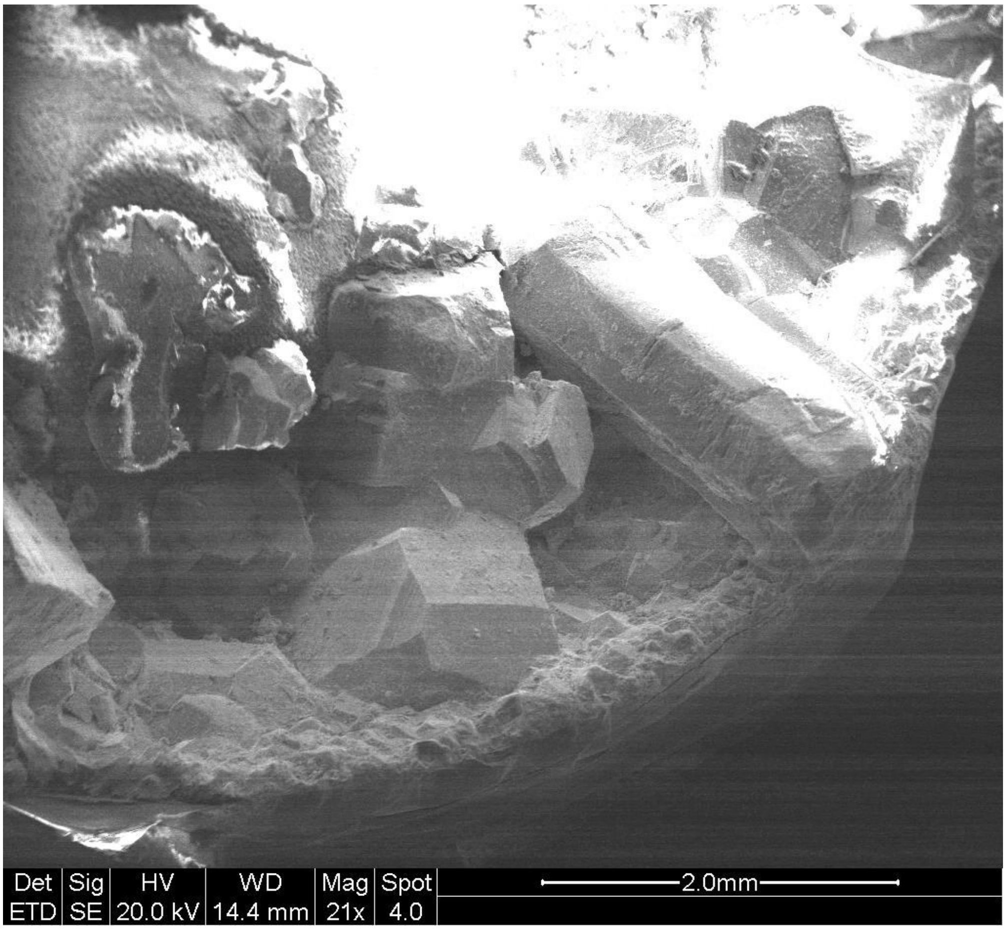

Figure 25: SEM image of ZnO crystals grown on one part of the ampoule walls, obtained using the ETD. The image is taken at high vacuum before the sample became too charged for further imaging at this vacuum level. Several crystals of varying sizes are visible and the crystals appear to be mostly polycrystalline.

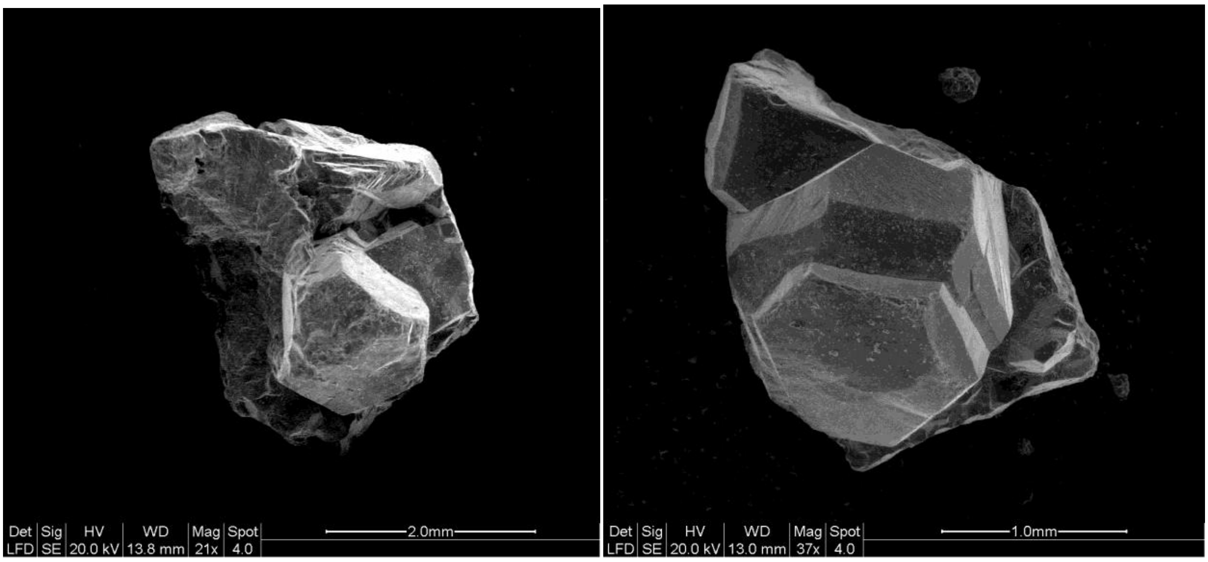

Figure 26: SEM images of two polycrystalline ZnO crystals grown by CVT, obtained using the LFD. The crystal on the left image has a quite rough surface, although the transparency was still high. The crystal on the right image has smooth faces and the hexagonal structure of wurtzite ZnO is possible to deduce from the angles of the faces.

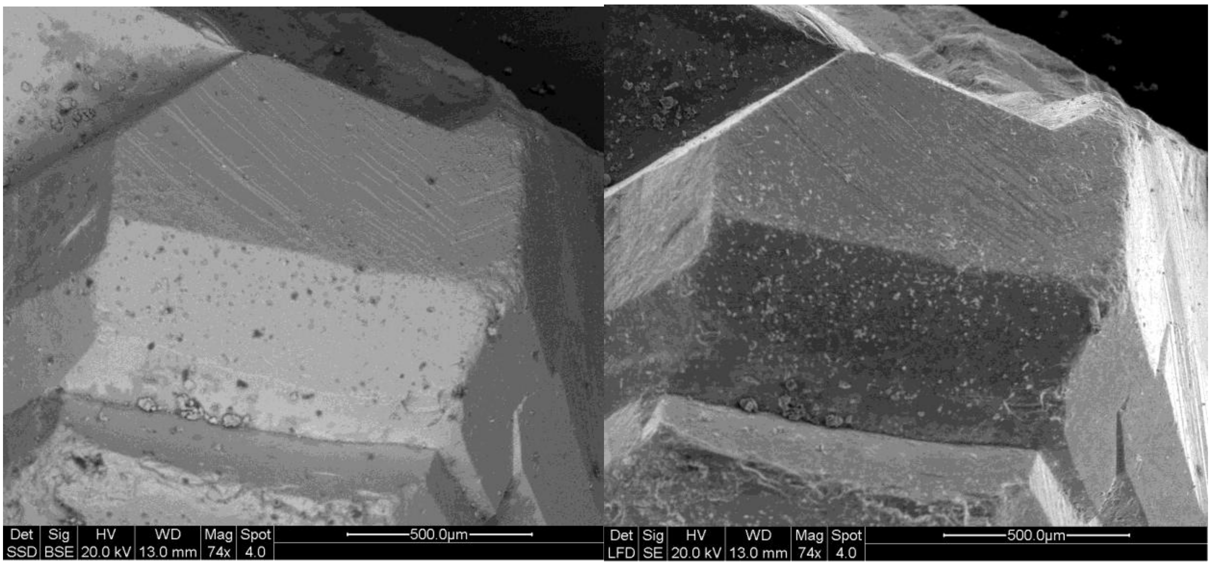

Figure 27: Magnified SSD and LFD images of one of the crystal faces shown to the right in Figure 26. Both images reveal a stepped surface, although the SSD image shows that most of the particles on the surface have a different composition than the crystal.

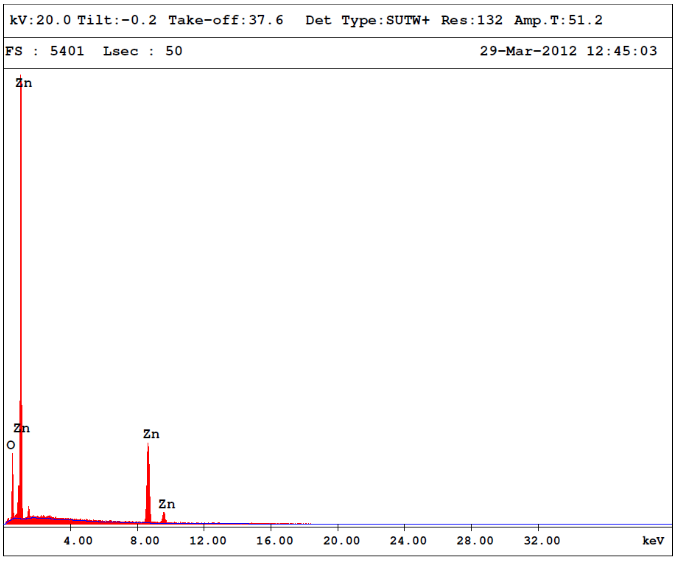

Figure 28: EDS spectra of the ZnO crystal shown in Figure 27. The small unindexed peak was by the software suggested to be Al, although the presence of Al is highly unlikely in the crystal and the peak is more likely a result of Si contamination.

Table 5: Composition of ZnO crystal face acquired by EDS analysis

Element	Atom %	Weight %
O	43	15
Zn	57	85

The crystal faces were also covered with some powder, which EDS analysis indicated to contain chlorine (Figure 29 and Table 6). As the powder was not isolated, the data is affected by the underlying ZnO crystal which makes it difficult to describe the composition of the powder. It is however quite likely due to condensation of the transport agent $ZnCl_2$ on the surface of the crystals, which is also supported by an increase in the Zn signal in the powder compared to the crystal face. It is highly unlikely that any ammonium chloride should remain as hydrogen and nitrogen are unlikely to react back to NH_3 again. It is however not possible with EDS to say for sure if the powder could be ammonium chloride, as hydrogen is impossible to detect with EDS, and with the small amounts of N compared to the underlying ZnO, in addition to the reduction in sensitivity of lighter elements at low vacuum, N is not expected to be visible in the spectrum. The presence of Si, which can be seen in the spectrum, also indicates that this is present in the powder, and probably stems from the container used to store the sample.

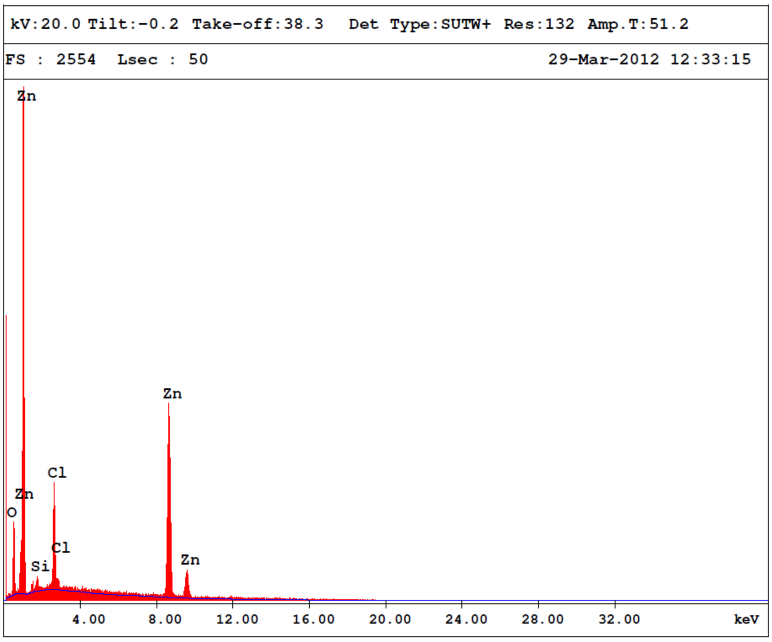

Figure 29: EDS spectra from powdery area of one of the ZnO crystals.

Table 6: Acquired composition from scan in powdery area of the sample

Element	Atom %	Weight %
O	27	9
Zn	62	83
Cl	9	7
Si	2	1

5.3 CVT of ZnS – Results

Only one ampoule of ZnS was successfully grown. After 14 days of growth, polycrystalline ZnS crystals were extracted from the ampoule. The scent of H_2S was noted, and evidence that it was present in the ampoule. The crystals were grown in the cold end, which agrees with thermodynamic calculations performed. The polycrystals were ~2-3 mm^3 and exhibited a yellow hue. The size of the crystals indicates quite rapid growth rates, which could affect the crystallinity of the crystals. The mass of the produced crystals are estimated to be ~0.4 g, which is slightly higher than the theoretical calculations suggest (0.26 g), which indicates that the temperature gradient is slightly larger than what the thermocouple of the furnace displays.

The transparency of the produced crystals was low and XRD data obtained at the synchrotron at the ESRF can be seen in Figure 30. The diffraction data reveal several ZnS orientations, indicating that the grown crystals are of relatively poor quality compared to the ZnO crystals. As the inspected crystals were quite small and the ones that were found appear to be polycrystalline, suggests that any single crystal would be too small for any practical purpose. For this reason, the ZnS crystals were not studied further with other techniques. While growing better crystals of ZnS possibly could be achieved using a lower temperature gradient, it was not prioritized as ZnO is considered to be the main focus of this study.

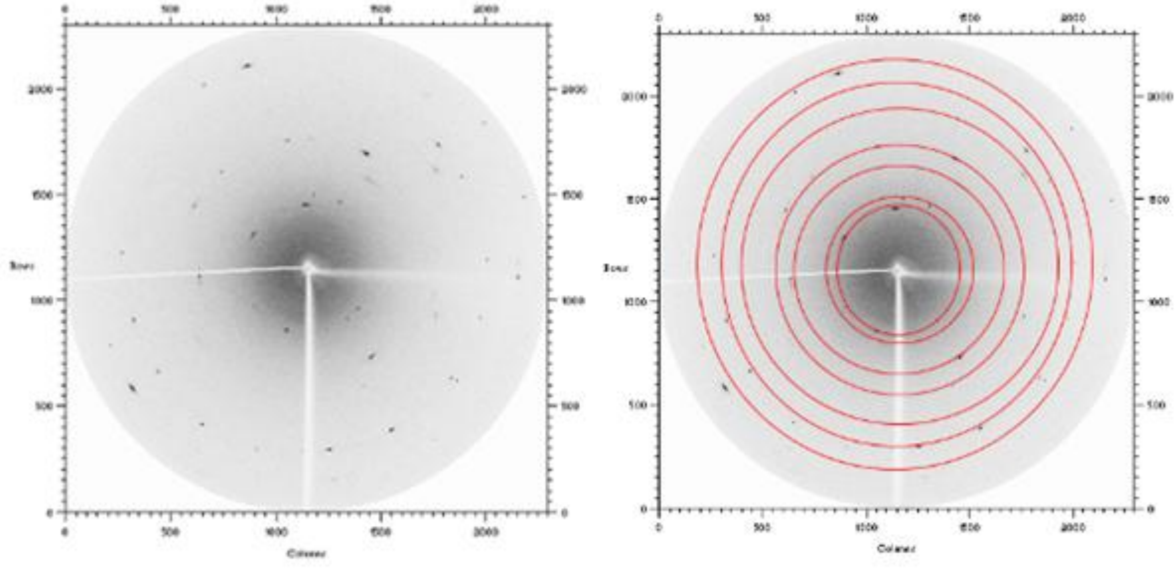

Figure 30: The left image shows an area diffraction pattern of one of the ZnS crystals grown by CVT. The right image shows the same figure with an overlay of plane distances corresponding to the (111), (200), (220), (311), (400), (331) and (422) planes. The (111) planes are closest to the middle, while (422) planes are represented by the outermost circle.

6 Development of Thin Film SXRD

The setup described in the experimental section proved useful in order to analyze thin films, and Figure 31 shows a raw CCD image of an 800 nm Co_3O_4 thin film deposited on a α-Al_2O_3 substrate. Diffraction spots of both thin film and substrate are easily distinguished. As the thin film is on the nanometer scale in one direction and several orders of magnitude larger in the two other directions, the reflection will be similar to a dumbbell in shape. The substrate which is much thicker will exhibit sphere shaped reflections. This information is however not needed if the unit cell of the thin film or substrate is known, as the CrysAlis Pro software by Agilent Technologies® used to analyze the diffraction data is able to automatically untangle which reflections belong to the film.

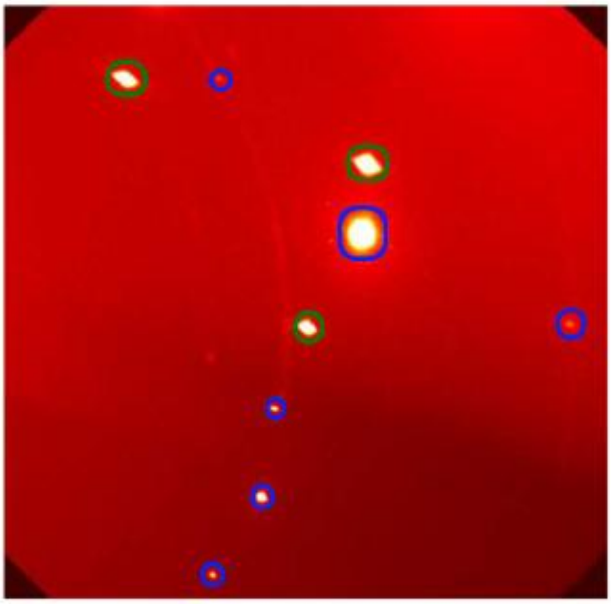

Figure 31: Raw CCD image obtained by SXRD of Co_3O_4 deposited on α-Al_2O_3. The reflections circled in green originate from the thin film and can be distinguished from the substrate peaks circled in blue by the shape of the reflection. The axes on the image are pixels on the detector, and converting these values is a complicated process. The image is thus for illustration purposes only.

It was possible to reproduce and confirm previously known results about the thin film samples with the setup, but it was also discovered that it was possible to obtain additional information that could not be extracted by regular XRD. A significant problem however is that the software currently is not designed for thin films, and getting the needed information to a presentable format is extremely tedious work. The images obtained are pixels on the detector and while the software is able calculate what each pixel represents in reciprocal space, the information is hidden and consequently producing reciprocal space maps of single reflections must be done manually if desired. This has not been carried out in this study, and the images are mainly for illustrative purposes and to show what kind of information is possible to obtain. Another limitation with the software used for data reduction is getting information about the surface structure. Diffraction rods originating from the surface or interface were visible on several samples as shown in Figure 32, however it was at the present not possible to extract information from these rods. Note that the image is simply a snapshot and as the tilt of the sample is increased, the CTR will move directly towards the right in the image and with oscillating intensity. The left side of Figure 33 shows well resolved diffraction from two thin film reflections in Figure 32, while the right side shows a blown up image of the crystal truncation rod. A long range of samples were investigated, and a selection of these will be presented in this study.

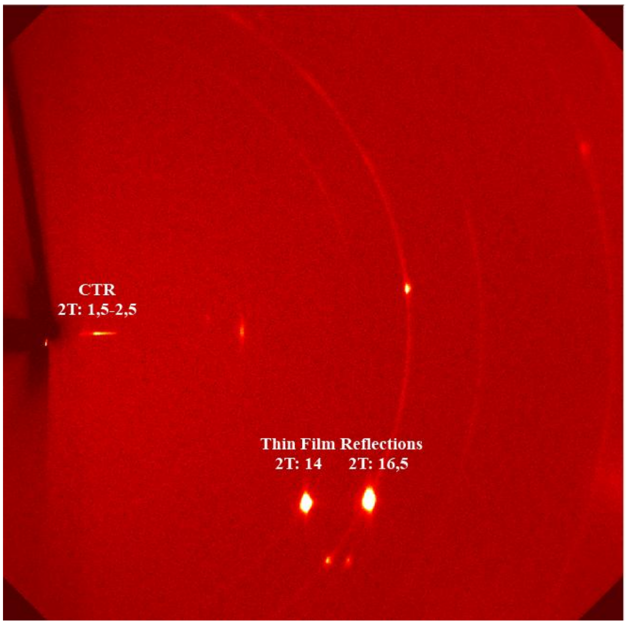

Figure 32: Raw CCD image of Co_3O_4 thin film on Al_2O_3 (different sample from previous image). A crystal truncation rod (CTR) is visible at 2 theta ≈ 1.5-2.5. Well resolved diffraction spots are visible at 2 theta ~14 and ~16.5.The shadow of the sample and beam stop can be seen to the left in the image.

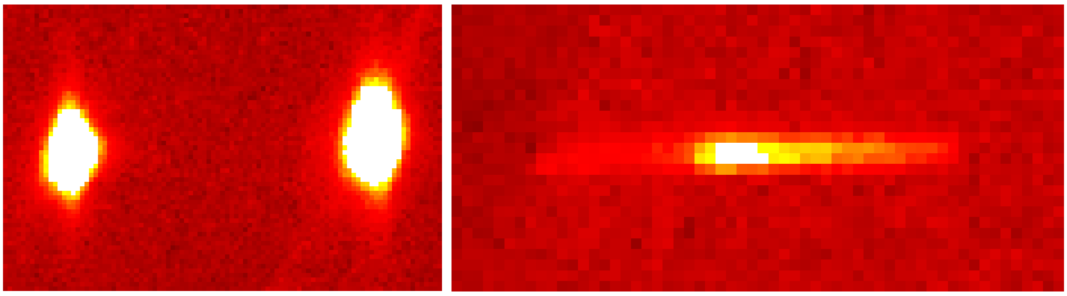

Figure 33: The left image shows the two dumbbell shaped thin film reflections from Figure 32, while the right shows part of a CTR from the same figure.

6.1 Thin Films of Co_3O_4 Grown on α-Al_2O_3 Substrate

The Co_3O_4 deposited on α-Al_2O_3(001) system has previously been grown and well characterized by Klepper et al. (*81, 82*) and the thin films shows a high degree of epitaxy. For this reason it is used as a model system in this study. The films were grown by the atomic layer deposition method (ALD, also known as atomic layer epitaxy or atomic layer chemical vapour deposition), which is a chemical gas phase thin film deposition technique. It is based on self-limiting gas-to-surface reactions, which means that a complete monolayer is grown before the next layer is deposited and allows for controlled growth of thin films (*82*).

The Co_3O_4 has a spinel (cubic) structure type with lattice parameters of a = 8.08 Å (*83*), while the α-Al_2O_3 adopts a trigonal structure with cell dimensions of $a = b$ = 4.76 Å and c = 12.93 Å. Although α-Al_2O_3 is trigonal, the (001) plane can be considered to be pseudo hexagonal (*82*). The diffraction pattern in Figure 34 obtained by Klepper et al. clearly indicate highly ordered and crystalline Co_3O_4 growing in the (111) direction.

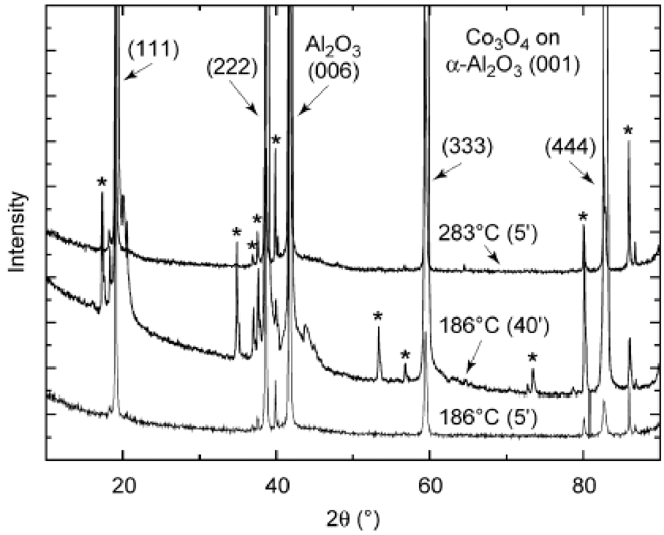

Figure 34: XRD diffraction patterns of Co_3O_4 deposited on α-Al_2O_3. The reflections marked * stem from impurities in the X-ray tube producing CuK*β* and WL*α (82).*

The diffraction data obtained by SXRD resulted in lattice parameters for α-Al_2O_3 of a = 4.8 Å and c = 12.8 Å. The reciprocal lattice grid is shown in Figure 35. Figure 36 shows the reciprocal grid of Co_3O_4 with respect to the Al_2O_3 lattice. The lattice parameters were found to be a = 7.98 Å, which are 1.4 % lower than previously found parameters for bulk Co_3O_4 i.e. a = 8.08 (*83*). The diffraction spots indicate that the thin film is highly oriented along the [111] direction, which is in agreement with data obtained by Klepper et al.

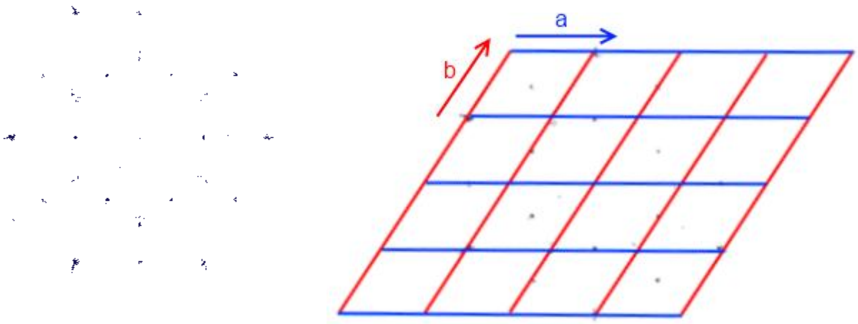

Figure 35: SXRD diffraction data of 800 nm of Co_3O_4 on α-Al_2O_3. The left image shows all the obtained diffraction spots. In order to get the best match, the spots with low intensity are filtered out. The right image shows the reciprocal lattice grid of α-Al_2O_3 found by the software in order to obtain the best fit with the remaining diffraction spots. The spots not in the corners of the reciprocal lattice belong to the thin film.

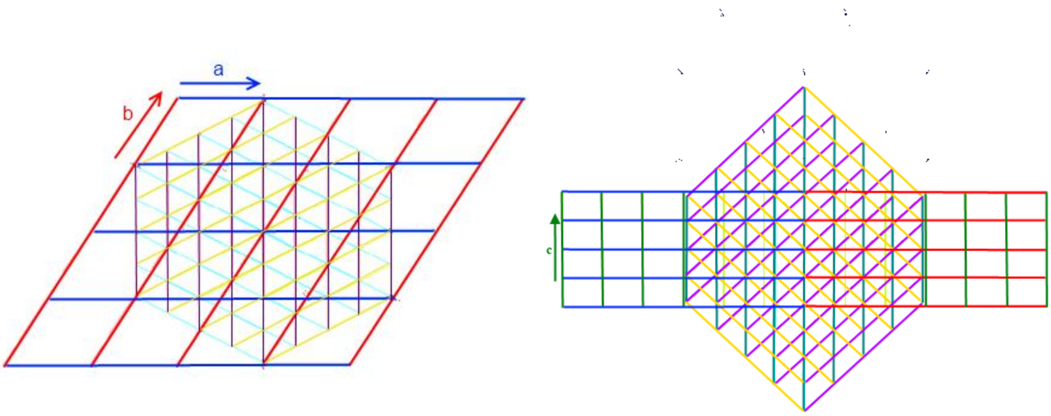

Figure 36: SXRD data of 800 nm of Co_3O_4 on α-Al_2O_3. By matching the angle and distance between reflections to certain lattice parameters, the software is able to find the orientation of the unit cells of the thin film and substrate. The left image shows the substrate viewed along the [001] direction of the substrate, with the *c* axis pointed away from the reader. The hexagonal pattern in the middle originates from the cubic thin film and confirms that the film is grown in the direction of the densest packed planes, i.e. the [111] direction, which appears hexagonal. On the image to the right, the *a* and *b* axis intercept in the middle of the figure. The blue lines represents the *a* axis, while the red represents the *b* axis. The reflections seen above the two grids are repeated periodically and fit the grids when the grids are repeated along the *c* axis.

After reconstructing the 3-dimensional reciprocal space and finding the orientation matrix, it is possible to make slices along certain directions by integrating the frames obtained by the scan. This can be used in order to view specific reflections, which may give information about split peaks or crystal truncation rods that could appear between two specific reflections. Figure 37 shows such slices through reciprocal space. If the substrate and thin film is indexed correctly, the software is able to identify which peaks that correspond to certain reflections.

This way it is possible to pick out interesting reflections that can be scanned with a higher resolution.

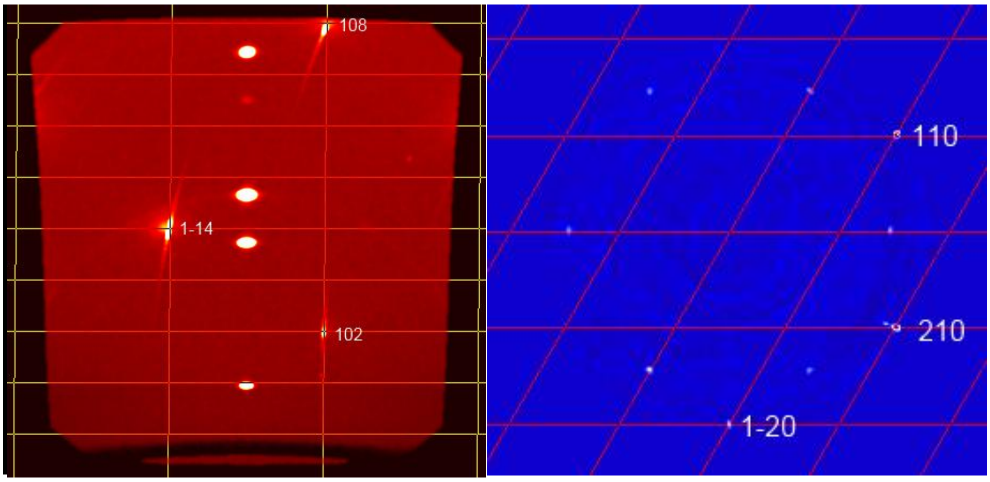

Figure 37: Slices through reciprocal space of Co_3O_4 on α-Al_2O_3 substrate. The slice on the left is spanned by the reciprocal lattice vectors [110] and [101], while the slice on the right is spanned by the [100] and [010] reciprocal lattice vectors. Both reciprocal grids use the α-Al_2O_3 lattice parameters as basis and reflections in the corner of the reciprocal cell thus belong to the substrate, while the remaining spots belong to something else, which in this case is the Co_3O_4 thin film. Note that the background colour is chosen in order to make the reflections easily distinguishable.

Figure 38 shows a slice through reciprocal space with the thin film as basis, which must at the moment be done if a reciprocal grid of the thin film is desired. This is however not needed as the software is able to tell which reflection belongs to the thin film even without the grid. Using the thin film as basis for a slice through reciprocal space can however be useful in order to find reflections from the thin film which are difficult to find using the substrate as basis.

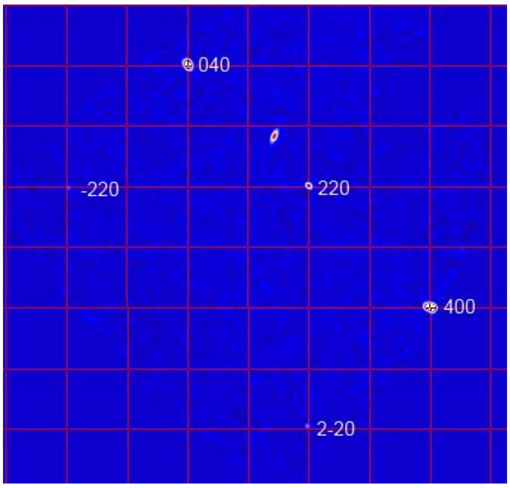

Figure 38: Slice through reciprocal space of the same sample, but with the Co_3O_4 lattice parameters as basis for the reciprocal grid. The slice is spanned by the [010] and [100] reciprocal lattice vectors of the thin film.

The command to scan specific reflections was used in order to obtain a set of reflections shown in Figure 39. The images show a family of reflections: the (222), (444) and (666) reflection. These images are useful in order to obtain information about the crystal quality of the thin film, as the far out reflections will often reveal split peaks due to lattice mismatch or slight disordering in the crystal. This sample exhibits no such feature, indicating that the film is of very high structural quality. If the sample is perfectly aligned, the FWHM may be found in order to determine the size of the crystallites in the film. A slight misalignment will however result in a broadening of the reflexes that are not correlated to the material itself, and using the obtained intensities without doing additional scans will only result in qualitative data.

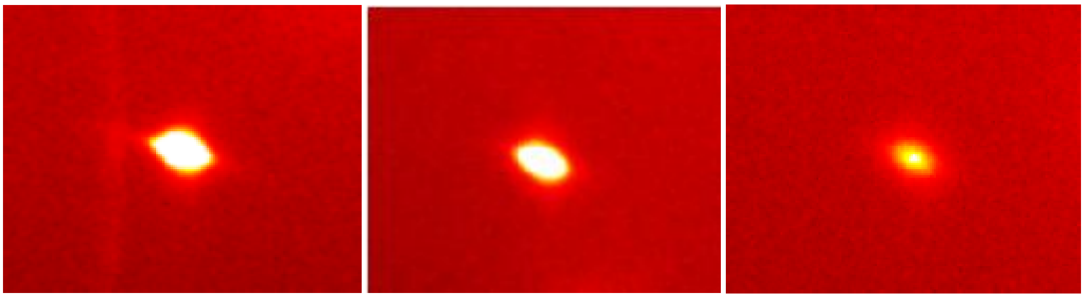

Figure 39: Symmetric single reflections from the Co_3O_4 thin film. Left: (222)-reflection. Middle: (444)-reflection. Right: (666)-reflection, images are scaled respectively to each other in order for comparison to be possible.

6.2 $SrTiO_3$ Substrates

It has previously been common practice at the Department of Chemistry at the University of Oslo to recycle old single crystal substrates as these are usually highly expensive. This has simply been done by polishing the substrate until no film remains. Regular XRD of the polished substrates show that no film remains and the substrate still appears to be single crystal. A $SrTiO_3$ substrate was however etched with HF with the purpose to create a TiO_2 terminated surface. A polished and an etched $SrTiO_3$ substrate was investigated with the thin film setup at the ESRF and Figure 40 shows a raw CCD image of the polished substrate. Powder rings are evident, and it is clear that polishing the sample severely damages the structure of the surface. Figure 41 shows diffraction data obtained by the same setup of the HF etched substrate. It is apparent that etching the surface with HF practically restores the substrate back to its original state and should be a much better way to recycle used substrates. $SrTiO_3$ is a perovskite and has previously been reported to have a lattice constant of a =3.9 Å

(*84*). The lattice constant found by SXRD of the etched substrate in this work was found to be in good agreement with this, i.e. a = 3.92 Å.

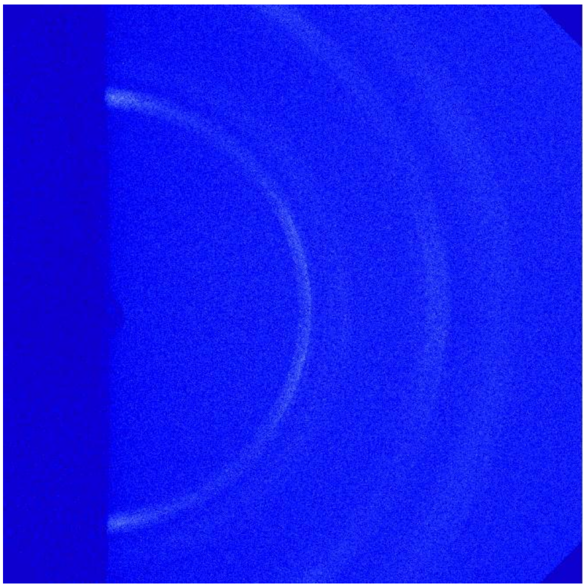

Figure 40: Raw CCD image taken with the thin film setup of a supposedly single crystal polished $SrTiO_3$ substrate. The image reveals that the surface of the substrate is purely polycrystalline.

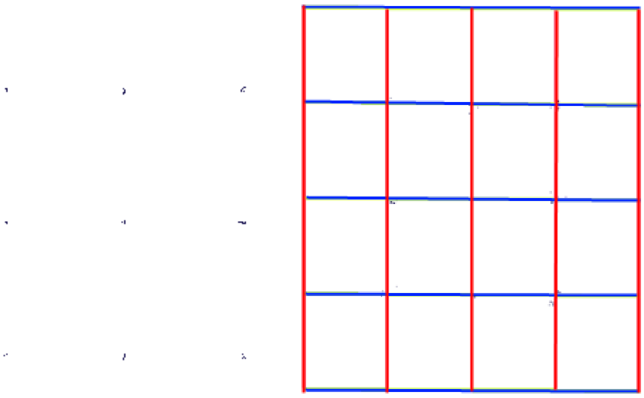

Figure 41: SXRD diffraction data of a HF etched $SrTiO_3$ substrate. The left image shows the result of the peak hunt, while the right image shows the corresponding lattice found by the software in order to index the reflections. The cubic symmetry of $SrTiO_3$ is apparent and in perfect agreement with previous results.

6.3 $LaMnO_3$ on Al_2O_3 and $Ca_{1/3}La_{2/3}MnO_3$ on $LaAlO_3$

Two samples previously prepared with ALD at Inorganic Chemistry group at the University of Oslo, were investigated with the purpose of determining the substrate face the thin films were grown on, and to determine the crystallinity of the grown thin films. The first sample with $LaMnO_3$ on Al_2O_3 revealed the substrate to be cut in the [11-20] direction as can be seen from Figure 42. The sample exhibited a crystal truncation rod in the middle of the powder semi spheres, although it is at the moment not possible to extract further information from this. A thin film of $Ca_{1/3}La_{2/3}MnO_3$ on $LaAlO_3$ was also studied, as can be seen to the right in Figure 42. Both samples were completely polycrystalline, and not much information could be extracted, apart from the cubic substrate being cut in the [001] direction.

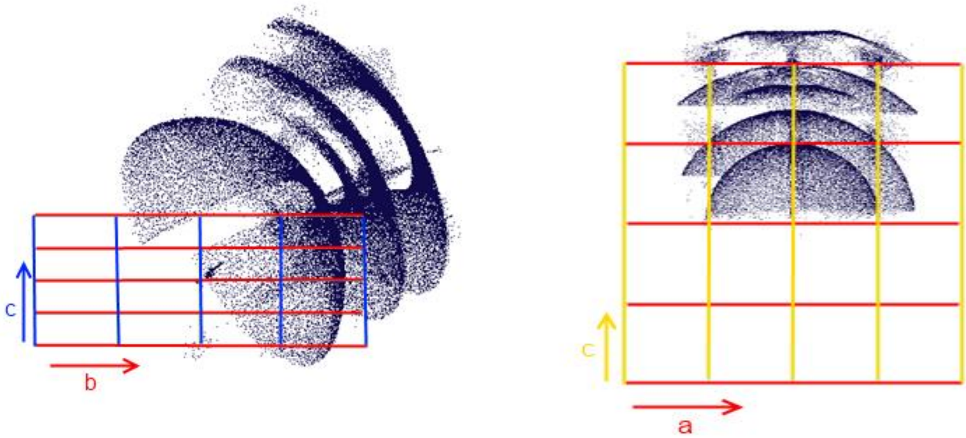

Figure 42: The left image shows $Ca_{1/3}LaMnO_3$ on $LaAlO_3(001)$ viewed along the -*b* axis. The right shows $LaMnO_3$ on Al_2O_3(11-20) viewed from the side (the *a* axis is pointed 60° out of the *cb*-plane).

Figure 43 shows a slice through reciprocal space of the $Ca_{1/3}La_{2/3}MnO_3$ on $LaAlO_3$ sample, spanned by the [100] and [010] reciprocal lattice vectors of the substrate. The image shows that it is possible to obtain powder diffraction patterns that may be used to find the structure of the thin film if needed.

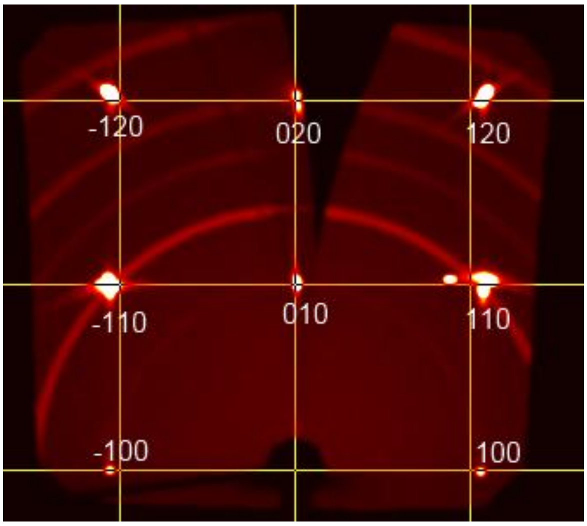

Figure 43: Slice through reciprocal space of the $Ca_{1/3}La_{2/3}MnO_3$ on $LaAlO_3$ sample, spanned by the [100] and [010] reciprocal lattice vectors of the substrate. The rings may be analyzed like a powder diffraction pattern and may be used to confirm that the film consists of $Ca_{1/3}La_{2/3}MnO_3$.

6.4 MnO_2 on MgO

A sample of with tetragonal MnO_2 grown epitaxially on an MgO substrate was studied with the purpose of finding the texture of the film. The sample was previously grown and characterized by O. Nilsen et al. (*85*). Figure 44 shows a raw CCD image of the diffraction with the thin film setup. The powder ring is from the thin film and two strong reflections can be seen right next to each other along the ring (middle of the figure). The smaller diffuse spots are from the substrate and also show two preferred orientations. This indicates that the two preferred orientations of the film, which results in an unusual film texture, most likely were adopted from the substrate as it also exhibits two preferred orientations, and is not a consequence of the growth conditions.

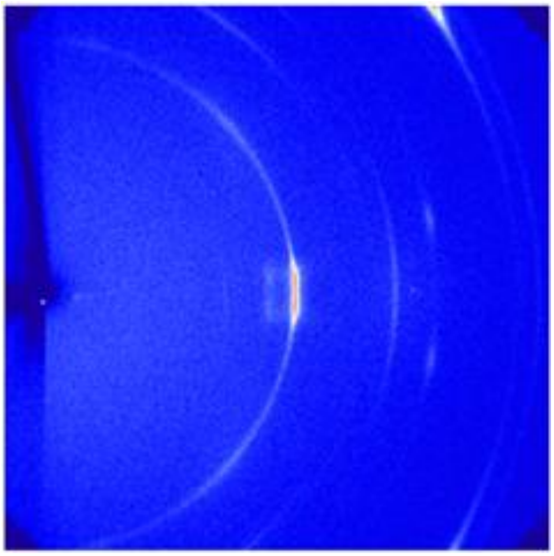

Figure 44: Raw CCD diffraction pattern of MnO_2 on MgO. Two preferred orientations can be seen for both the thin film and the substrate, indicating a texture of the film and substrate as shown to the right.

6.5 Choice of Substrate

Some of the thin films that were investigated were difficult to index as they were grown on Si substrates. Phonon scattering is a pronounced effect in crystalline Silicon, and at the boundary between Si and a thin film, the effect is even more pronounced as the phonons are scattered by dislocations in the interface region, which results in a lot of diffuse scattering (*86*). Diffuse scattering is a field on its own and a lot of information can be gained if proper software is employed in order to analyze the data; however this software is not yet compatible with the instruments available at the SNBL at the present. The use of Si as a substrate is consequently a poor choice if characterization with SXRD is desired, as the resulting noise may overshadow any reflections from the thin film. Figure 45 shows a raw diffraction pattern of polycrystalline ZnO deposited on a Si substrate.

Soda lime glass is another substrate not well suited for thin film characterization with SXRD. Figure 46 shows a raw CCD image of a $CaCO_3$ thin film deposited on soda lime glass. While amorphous substrates could be useful for thin film characterization, as all the strong reflections will be from the thin film, the diffraction from soda lime glass is highly diffuse and could easily hide thin film reflections. Figure 47 shows a 2θ scan of the same sample, demonstrating how the intensity distribution is dominated by the soda lime glass substrate.

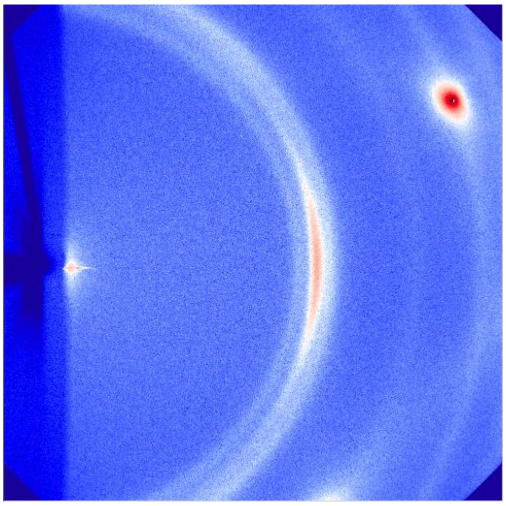

Figure 45: Raw CCD image of a polycrystalline ZnO thin film on a Si substrate. The large spot in the top right stems from the Si substrate, while the powder rings in the middle are from the ZnO thin film.

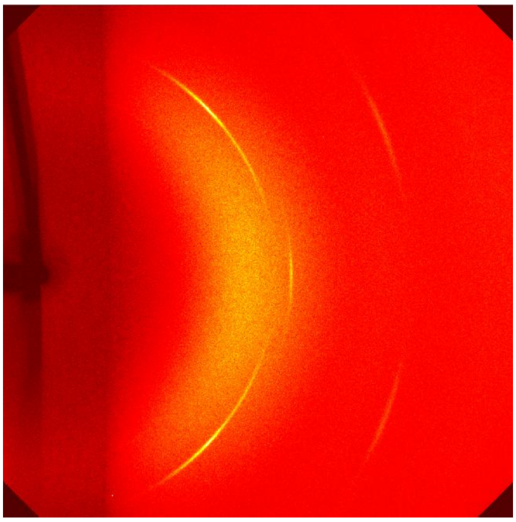

Figure 46: Raw CCD diffraction pattern of a $CaCO_3$ thin film on soda lime glass.

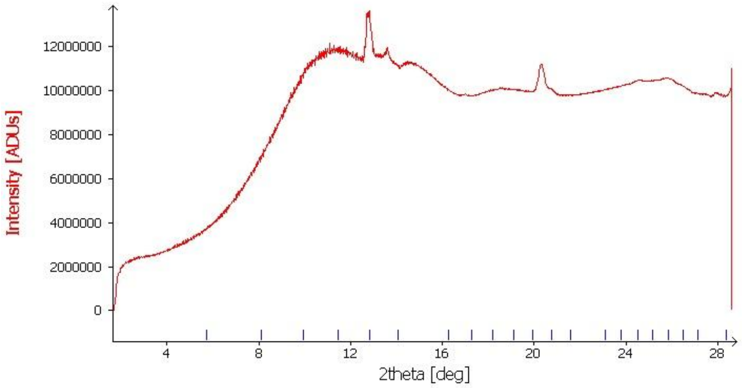

Figure 47: 2θ scan of the same sample. The resulting intensity distribution is dominated by the diffuse scattering from the soda lime glass substrate.

Substrates well suited for thin film characterization with SXRD would be materials like MgO, which only exhibits a few allowed reflections that easily can be separated from the thin film reflections.

7 Surface Calculation Results

7.1 The Clean Surface of ZnO(0001) and ZnO(000-1)

The problem arising from the polarization of the *c* axis has been treated in the same manner as suggested by Na. et al. (*67*), who suggested keeping the middle layers fixed in order to prevent unrealistically strong contraction. While the inward relaxation for the Zn terminated face, which does not agree with experiments still persists; it has been reduced significantly and can no longer be considered to have any significant impact on further calculations done on these surfaces.

In order to know the validity of the calculations, attempts to model the ZnO(0001) and ZnO(000-1) in vacuum were done in order to reproduce previous results obtained on these surfaces (*66, 67, 69*).

Relaxing the unit cell of ZnO using the CASTEP code resulted in the following lattice parameters listed in Table 7. The calculated values are around 1% higher than the experimental ones and the result is nearly identical to the one published by Zhang et al.

Table 7: Calculated lattice parameters using CASTEP geometry optimization compared with previously published result both computational and experimental

Axis	This work	Zhang et al. (*66*)	Experimental Values
a	3.28 Å	3.28 Å	3.2465 Å
b	3.28 Å	3.28 Å	3.2465 Å
c	5.28 Å	5.29 Å	5.2030 Å

Using these lattice parameters, a 2×2×3 supercell with a vacuum layer of 12.5 Å, and capping the bottom with hydrogen resulted in the structures shown in Figure 48 upon cleaving perpendicular to the *c* axis.

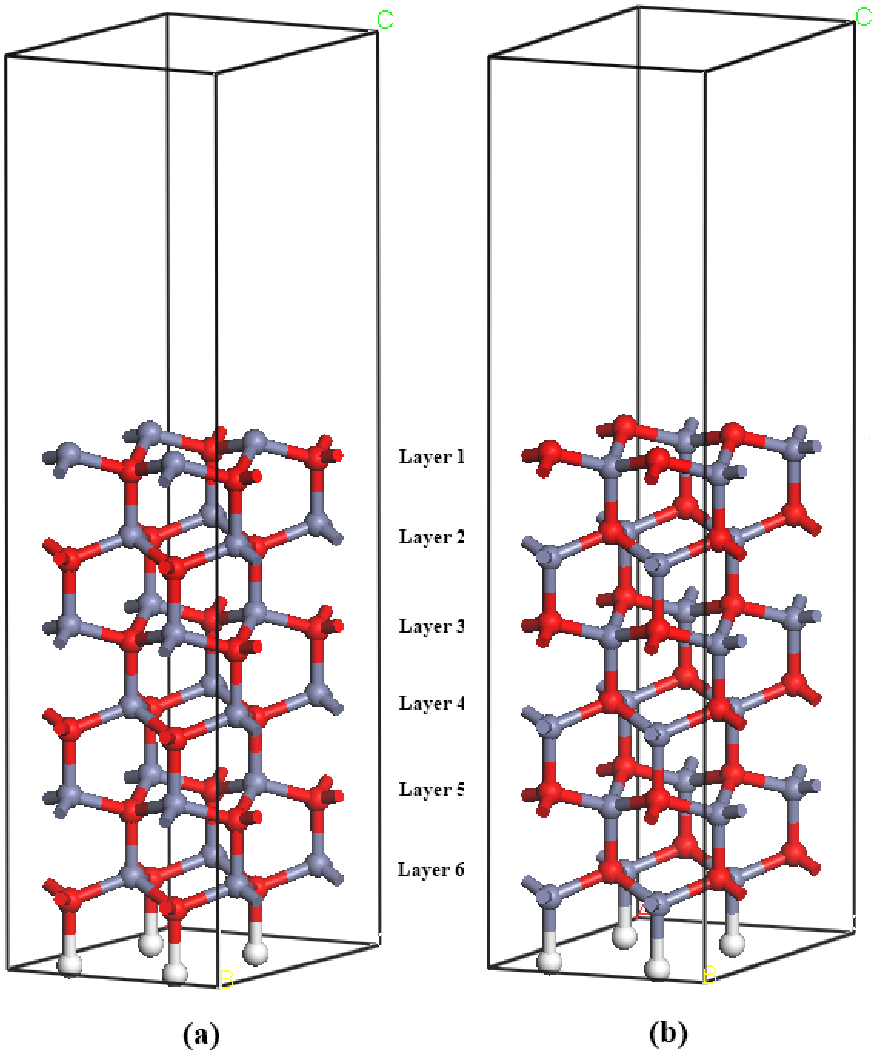

Figure 48: Three-dimensional views of the perfect (a) (0001) surface, and (b) the (000-1) surface. The red and blue are O and Zn atoms respectively. The slabs consist of 2×2×3 unit cells which results in six layer slabs. The bottom of each cell is capped with four pseudohydrogen atoms shown as white balls.

The geometry optimized structures using the DMol-3 resulted in a slight contraction of 0.062 Å between the first and second layer for the ZnO(0001) surface and practically no change between the second and third layer. The O terminated ZnO(000-1) surface calculation gives a fairly strong contraction of 0.256 Å between the first and the second layer, with a much weaker contraction between the second and third. The results are shown in Table 8 and Table 9. While the results are in good agreement with the previously published result for the interlayer relaxation between the first layers R_{12}, they deviate quite a lot between layer two and three, denoted R_{23}. The reason for this is the choice of fixed layers. Zhang et al. have fixed layer five and six, while in this work layer three and four were held at fixed coordinates, which thus results in a sharply reduced relaxation between layer two and three.

Table 8: Calculated bond length contraction (Å) of Zn-terminated ZnO(0001) surface

Interlayer relaxation	This work: GGA-PW91 DMol-3	Zhang et al. (*66*) GGA-PBE DMol-3
R_{12}	-0.062	-0.109
R_{23}	0.002	0.136

Table 9: Calculated bond length contraction (Å) of O-terminated ZnO(0001) surface

Interlayer relaxation	This work: GGA-PW91 DMol-3	Zhang et al. (*66*) GGA-PBE DMol-3
R_{12}	-0.256	-0.301
R_{23}	-0.043	0.112

The surface energies were calculated using Eq. 20 and are given in Table 10. Zhang et al. appear to have made an error in their choice of units, but apart from that, all the energies are in very good agreement. Wander et al. extrapolated their result for an infinite number of layers in order to arrive at an estimate for the actual surface energy.

Since both the ZnO(0001) and ZnO(000-1) surface is created upon cleaving a crystal, it is not common to speak of a specific surface energy for these surfaces. Due to the polarity of the surface though, they have quite different chemical and physical properties and thus it is of interest to find out which surface is the most reactive. By capping the bottom with hydrogen it is possible to observe this property and the calculations show quite clearly that the O terminated surface is more stable than the Zn terminated one. This agrees also with experimentally observed results although the surface energy for the O terminated surface is substantially lower than calculated by Zhang et al. Qualitatively though, the results seem to agree reasonably well with both previous calculations and experiments and was thus taken as encouragement to do further calculations with these surfaces in other atmospheres.

Table 10: Result of surface energy calculation for ZnO(0001) and ZnO(000-1)

	This work (6 bilayers)	Zhang et al. (*66*) (8 bilayers)	S. Na and C. Park (*67*) (6 bilayers)	Wander et al. (*69*) (Infinite bilayers)
Zn terminated ZnO(0001)	3.99 J/m^2	(2.2838 eV/m^2)* 3.6540 J/m^2	4.299 J/m^2	~4 J/m^2
O terminated ZnO(000-1)	2.74 J/m^2	(2.2736 eV/m^2)* 3.6377 J/m^2		

* Most likely a misprint as 1 eV corresponds to $1.6\cdot10^{-19}$ J. In the surface science community it is often common to write the surface energy in units of eV/Å^2 and thus the m^2 is likely supposed to be Å^2. The number positioned underneath in the table is the corresponding energy if this is the case.

7.1.1 ¼ ML Coverage of O_2 on ZnO(0001)

A reference energy where oxygen is not bonded to the surface was found (Figure 49) in order to be able to compare the bonding energy of other structures. Figure 50 shows the first configuration that was tested (i.e. O_2 bonded perpendicularly to the topsite above Zn) and Figure 51 shows what happens upon relaxation. The calculations indicate that the top site is unfavorable and that the O_2 favors a position in one of the triangular pits created by Zn atoms on the surface. In order to name these triangular pits, the first layer is considered to consist of two sublayers of O and Zn respectively. An atom or molecule positioned in the triangular pit which is located directly above the bottommost sublayer, is indicated as being in a *hcp* position, as this can be considered as ABA stacking. The other triangular pit can in this way be designated as a *fcc* position as shown in Figure 52.

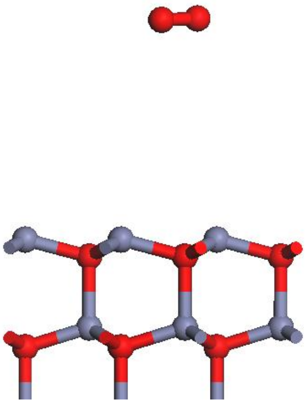

Figure 49: A two dimensional image of the Zn terminated ZnO(0001) surface with a O_2 molecule positioned far enough away so that the interactions with the surface can be considered to be negligible.

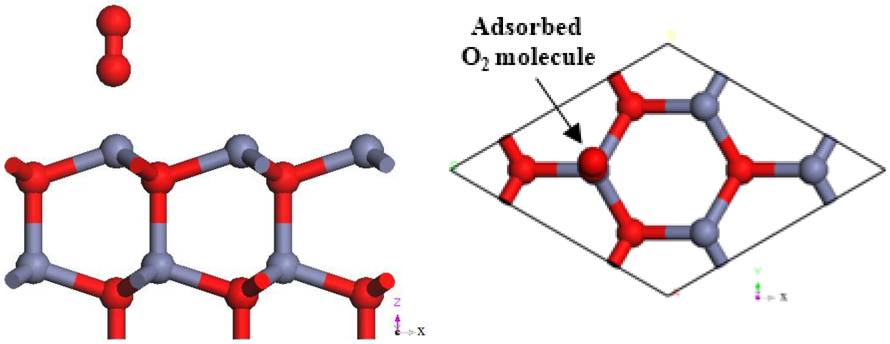

Figure 50: Two dimensional images of ¼ ML coverage of O_2 on top sites above Zn on the ZnO(0001) surface before relaxation.

In order to improve the accuracy of the calculation, a new relaxation was done of the *hcp* configuration with a slightly rotated O_2 molecule compared to Figure 51 as starting point, which resulted in the O_2 molecule being rotated 90 degrees with respect to the configuration in Figure 51. The energy is -2.65 eV lower than the reference.

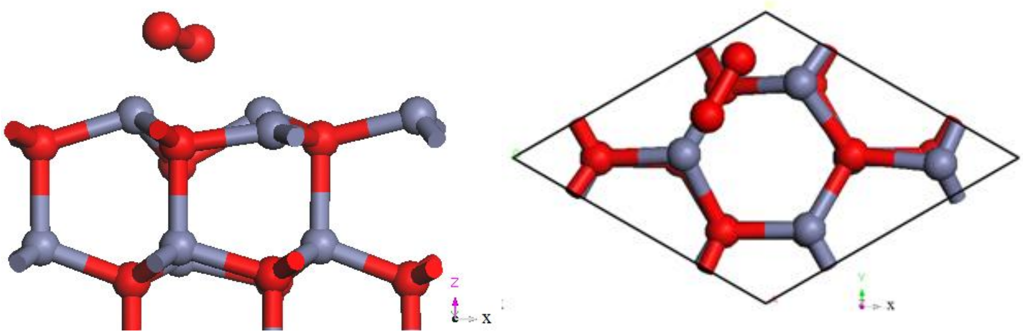

Figure 51: The images show the structures in Figure 50 after relaxation. The O_2 molecule diffused to one of the triangular pits created by the Zn atoms on the surface and positioned itself above a lower lying oxygen atom. This can in a way thus be classified as a *hcp* position.

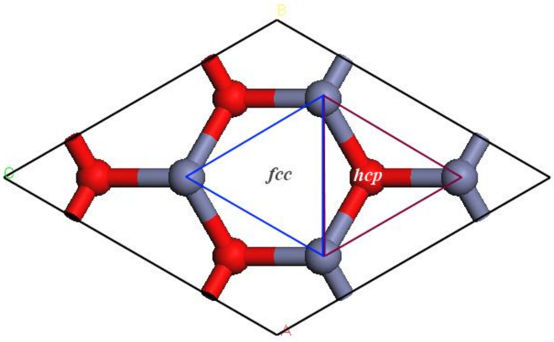

Figure 52: Two dimensional image of the surface of ZnO(0001), viewed along the *c* axis. The image shows the two triangular pits created by Zn on the ZnO(0001) surface, which in this work is designated at the *fcc* position(blue pit) or *hcp* position(violet pit).

Figure 53 shows the next position that was tested. In this *fcc* configuration, the O_2 molecule is positioned in the other triangular pit on the surface. The molecule did not move significantly upon relaxation and the total energy of the system is -2.93 eV lower than the reference energy. This configuration is thus calculated to be more stable than the *hcp* configuration and also the most stable of all the calculated positions at this coverage.

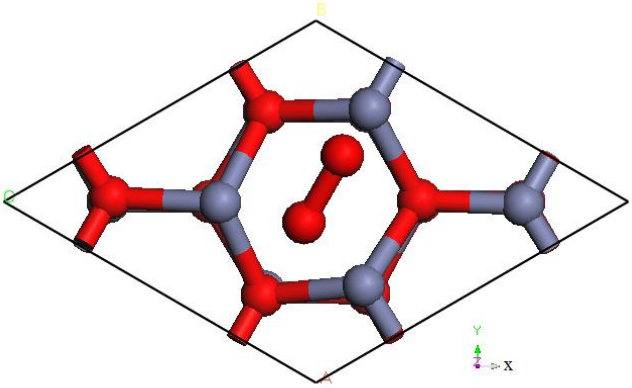

Figure 53: A two dimensional image of a flat O_2 molecule positioned in the *fcc* position on the ZnO(0001) surface. The configuration is calculated to be the most stable at this coverage.

A few other calculations were done with O_2 being positioned in various bridge sites, vertically above a surface oxygen atom (i.e. the vertical *hcp* position) and a configuration in which the O_2 molecule was used as a bridge between two Zn surface atoms. All of these configurations relaxed to either the *fcc* or *hcp* configuration. The only other configuration that did not relax to one of these, is the vertical *fcc* configuration shown in Figure 54. The energy of this system is -1.85 eV less than the reference and thus a bit higher than the flat *hcp* and flat *fcc* position. The differences in energy between the vertical *fcc* configuration and the flat configurations is however small enough that it may be observable for a finite time at ambient conditions at this coverage.

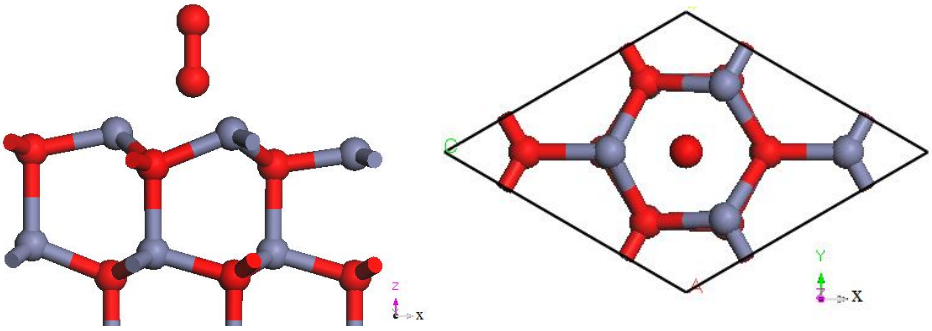

Figure 54: Relaxed structure with O_2 positioned vertically in the *fcc* position on the ZnO(0001) surface. The calculations indicate that the position is less stable than both the flat *fcc* and flat *hcp* configuration, but could still be a metastable surface state at ambient conditions.

In order to see if the O_2 molecule is likely to dissociate, energies for O adatoms in the *fcc* and *hcp* position were calculated (Figure 55). This corresponds to ½ ML of O on the surface. The calculations indicate that the *fcc* position is the most stable with an energy of -3.17 eV lower than the reference energy, while the *hcp* position only lies -1.45 eV below the reference. The result is thus that with one O_2 molecule per four unit cells of ZnO(0001) surface, the O_2 molecule is likely to adsorb to the flat *fcc* position before dissociating due to lattice vibrations and form the (1×2)-O adatom surface structure depicted in Figure 56.

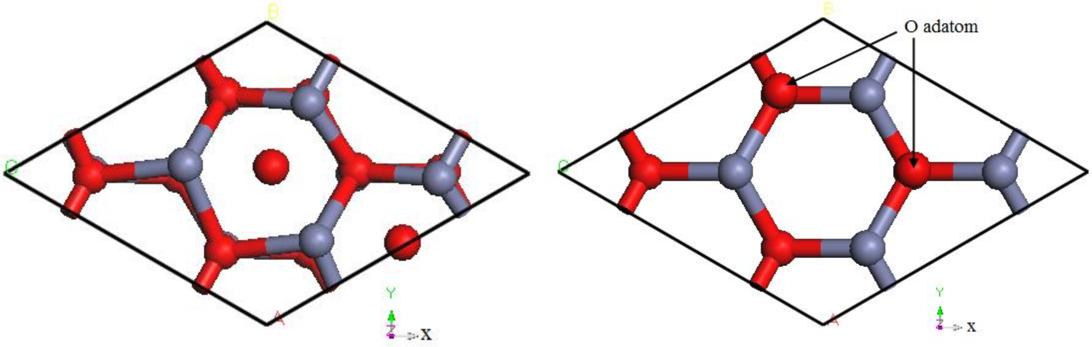

Figure 55: Relaxed surface structure of O adatoms on the ZnO(0001) surface in *fcc* position(left) and *hcp* position(right). Calculations suggest that the *fcc* position is the most stable configuration at ½ ML coverage of O adatoms on the ZnO(0001) surface.

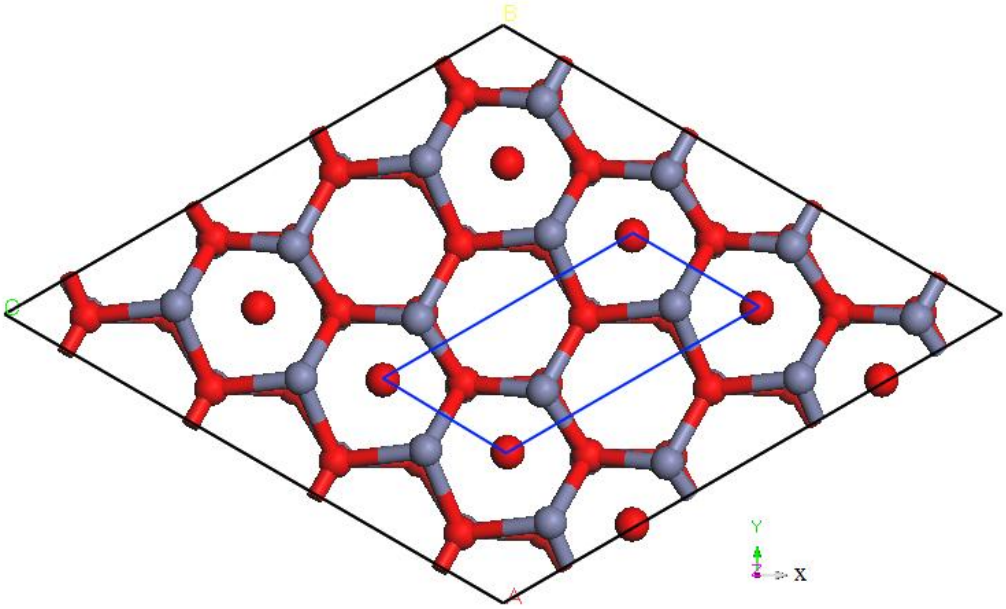

Figure 56: The calculated surface structure of ZnO(0001) with ½ ML of O adatoms. The blue box represents the smallest repeating unit, suggesting a (1×2)-O adatom surface structure.

Some other positions were also tested, but they all relaxed to the *fcc* position upon relaxation. Figure 57 shows an example of this. O adatoms were positioned on top sites above Zn atoms and upon relaxation they moved to the *fcc* position, clearly indicating this as the most stable adsorption site.

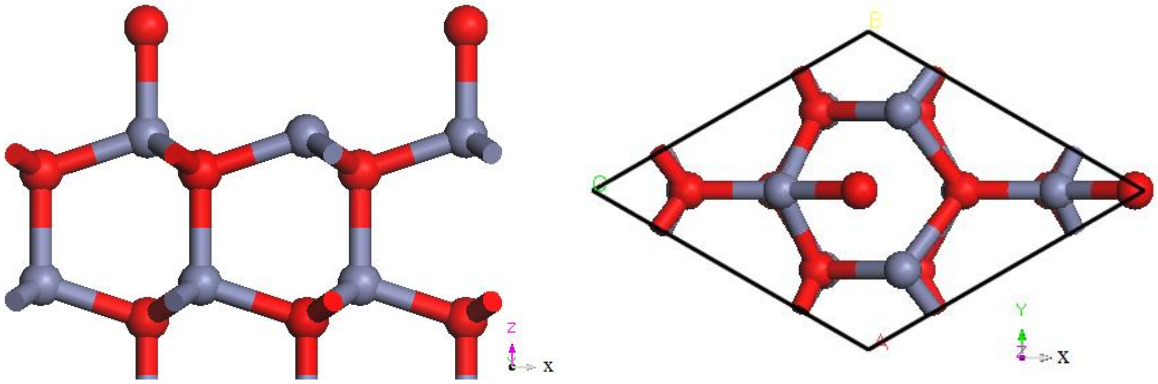

Figure 57: The left image shows O adatoms positioned on top sites directly above Zn atoms before relaxation. The right image shows the relaxed structure, indicating that the *fcc* position is the most stable adsorption site at this coverage. Note that the bonds have no impact on the calculations and that only the atom positions matter.

A summary of all the relevant calculated energies can be found at the end of the next subchapter in Table 11.

7.1.2 ½ ML Coverage of O_2 on ZnO(0001)

A reference energy was again found where two O_2 molecules are positioned as far away from the surface as possible, as well as from each other. The first position that was tested was the most stable configuration at ¼ ML coverage of O_2, i.e. the flat *fcc* position shown in Figure 58.

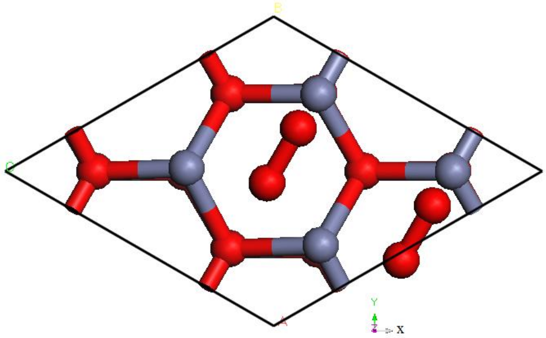

Figure 58: Two dimensional image of two relaxed O_2 molecules in the flat *fcc* position on the ZnO(0001) surface.

The structure did not change significantly upon relaxation and the calculated energy was found to be -3.44 eV below the reference.

The flat *hcp* position was also tested, but was found to be unstable and changed to the flat *fcc* position upon relaxation. The same happened with the tested bridge configurations as well. The vertical *fcc* configuration is still metastable and an energy of -2.32 eV below the reference was calculated.

None of the dissociated configurations were stable, and a calculation where the O adatoms were forced to stay in the *fcc* position was done in order to calculate the energy, which indeed was slightly positive (0.02 eV). Figure 60 shows the result of a run where the adatoms were positioned vertically above the Zn atoms (Figure 59). While the displacement did not converge even after 200 cycles, it is still possible to deduce that O_2 is formed. The position of O_2 on the surface has already been found, i.e. the flat *fcc* position, which could be a likely possibility to be the final position if the calculation had run for even more cycles and allowed the displacement to converge.

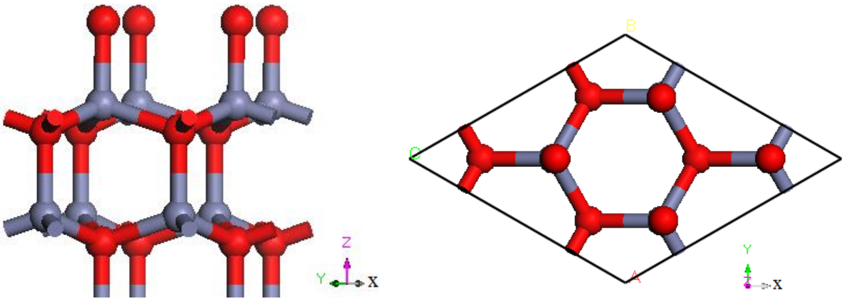

Figure 59: The images show dissociated O adatoms positioned directly above Zn from different angles. The images are taken before the relaxation process.

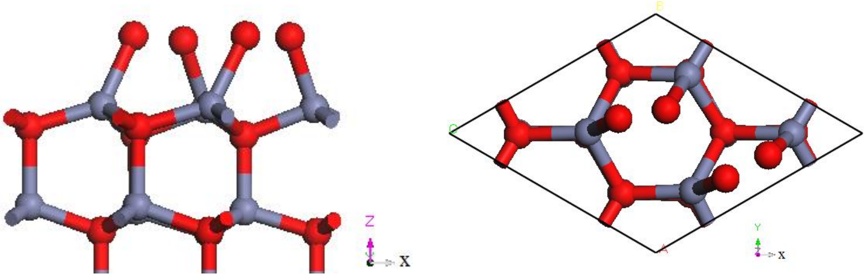

Figure 60: These images show the result of the relaxation, which did not complete even after 200 cycles of iterations. Even though the calculation did not converge, it is possible to deduce that oxygen bonds are formed and it is likely the final position will be the flat *fcc* position.

The final result is thus quite similar as the case for ¼ ML coverage of O_2, except of O adatoms in the *fcc* position being the most stable, the O_2 molecules now occupy this position instead as shown in Figure 61. A summary of all the relevant calculated energies can be seen in Table 11.

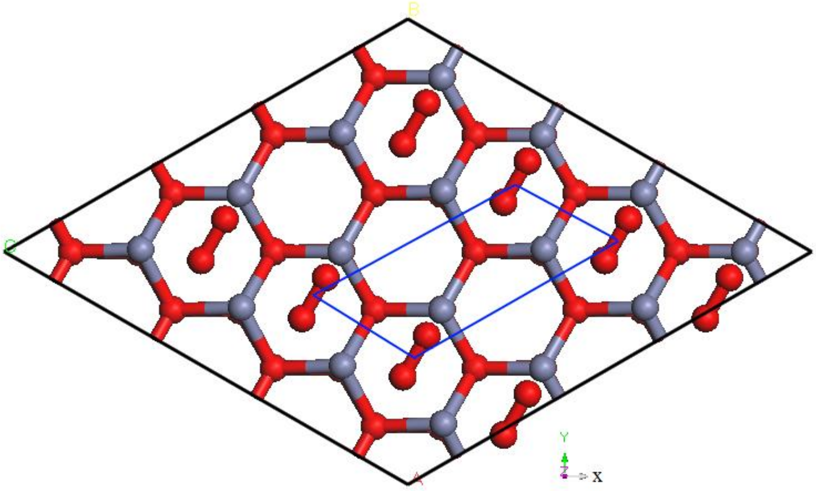

Figure 61: The calculated surface structure of ZnO(0001) with ½ ML of adsorbed O_2 molecules. The blue box represents the smallest repeating unit, i.e. (1×2)-O_2 surface structure.

Table 11: Calculated adsorption energies of O_2 in three binding orientations and the dissociated configurations of two of these for two coverages on ZnO(0001)

	Change relative to unbonded configuration (eV)	
Binding orientation	¼ ML*	½ ML*
fcc vertical	-1.85	-2.33
hcp flat	-2.65	Not stable
fcc flat	-2.93	-3.44
dissociated hcp	-1.45	Not stable
dissociated fcc	-3.17	0.02

* The coverages of dissociated oxygen are larger by a factor of two.

7.2 ZnO(0001) Surface in Zn Atmosphere

7.2.1 ¼ ML Coverage of Zn on ZnO(0001)

Figure 62 shows the two most stable tested configurations. The first is a distorted version of the *fcc* configuration, which can be considered as a bridge site. The second is a *hcp* configuration in which the Zn adatom sits directly above a substrate O atom. The total energies of these configurations were calculated to be -0.60 eV and -0.55 eV below the reference respectively. The top site configuration in which the Zn adatom is positioned directly above a substrate Zn atom had a slightly higher energy of -0.49 eV.

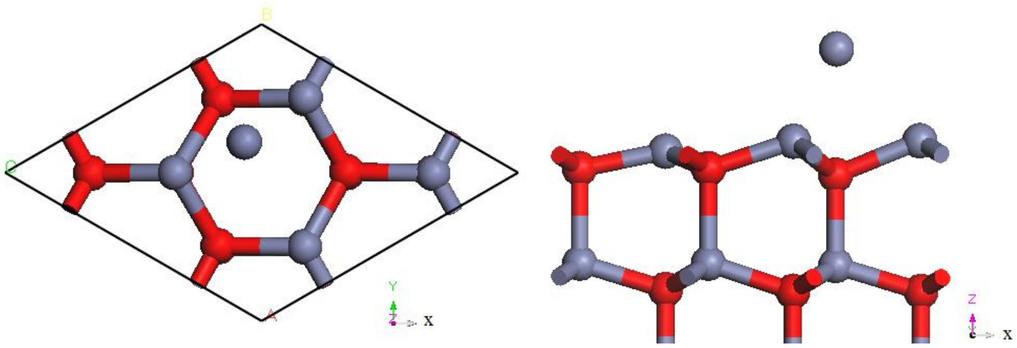

Figure 62: Two dimensional views of left: relaxed structure of the bridge site and right: relaxed structure of the *hcp* configuration. The bridge site has the lowest total energy and is thus the predicted adatom surface structure at this coverage.

The bridge site is thus the lowest calculated energy at this coverage and this will thus result in a (2×2)-Zn adatom surface structure at ¼ ML coverage as can be seen in Figure 63.

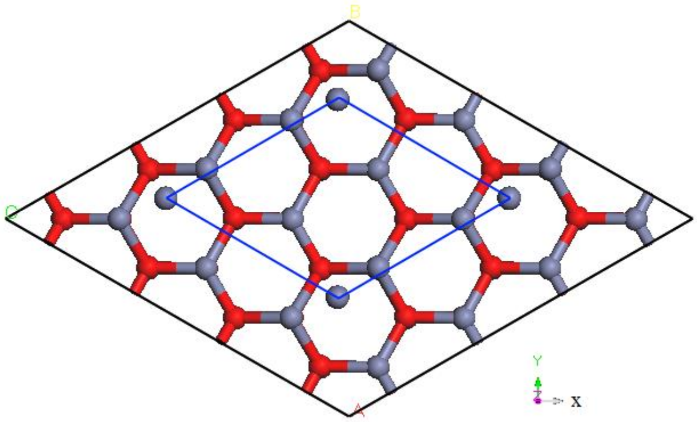

Figure 63: The calculated ZnO(0001)-(2×2)-Zn adatom surface structure with ¼ ML coverage of Zn.

7.2.2 ½ ML Coverage of Zn on ZnO(0001)

At ½ ML coverage the bridge position, which is slightly closer to the center than at ¼ ML coverage, is still slightly more favorable than the *fcc* with an energy of -2.855 eV below the reference. The *fcc* position no longer distorts towards the bridge and is also stable with an energy -2.850 eV below the reference. With an uncertainty of ~10^{-4} eV, the calculations can in theory differ between these configurations, although from a practical view, the difference in energy between the positions (Figure 64) is so small that they can be considered to be degenerate. The *fcc* configuration has a higher symmetry, which structures tend to prefer at higher temperatures, but electronic considerations could favor a bond between the two Zn adatoms, which causes a doubling of the unit cell. More careful calculations are necessary to make absolutely sure which configuration has the lowest ground state energy.

The *hcp* and the top site position above Zn were slightly higher in energy with energies -2.79 eV and -2.76 eV below the reference respectively. The calculated result at ¼ ML coverage is thus the ZnO(0001)-(1×2)-Zn adatom surface structure as shown in Figure 65.

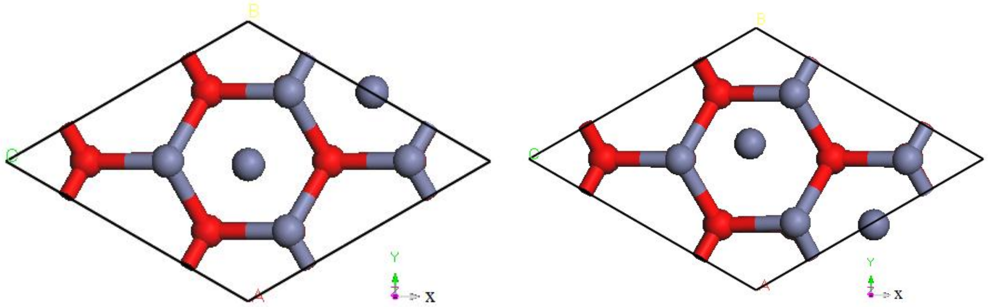

Figure 64: The left image shows Zn in the *fcc* position on the ZnO(0001) surface, while the right one shows the bridge site which is slightly more stable. At ambient conditions it is likely that both will be present and that the Zn adatom will continuously shift between the *fcc* position and various bridge sites.

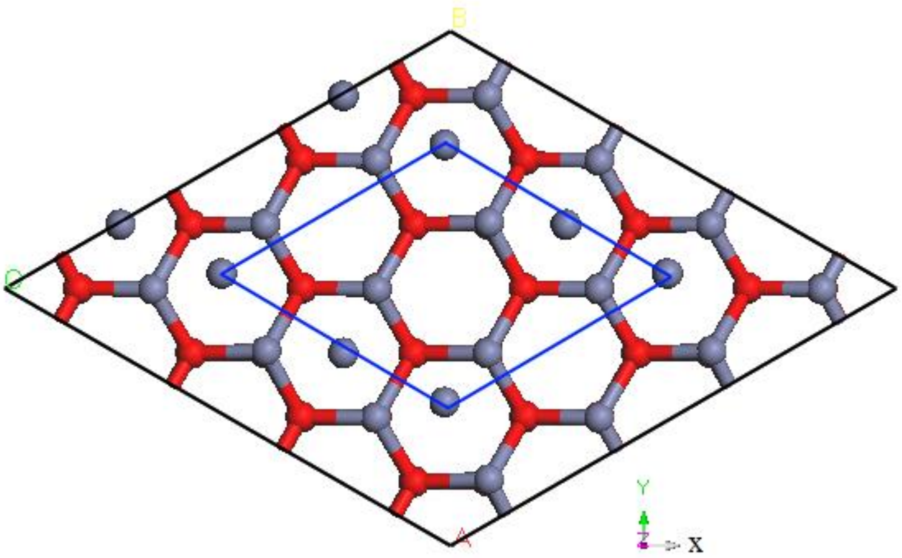

Figure 65: The calculated ZnO(0001)-(2×2)-Zn adatom surface structure for ½ ML coverage of Zn. The structure is likely to be degenerate with the *fcc* configuration which has a (1×2) surface structure, as the calculations with the selected parameters are not accurate enough to differ between these. At higher temperatures the *fcc* configuration might be more stable as this would imply a higher symmetry.

7.2.3 1 ML Coverage of Zn on ZnO(0001)

At 1 ML coverage of Zn, the structures begin to become quite complex and a lot of possibilities had to be tested. A slightly distorted version of the *fcc* position (Figure 66) was still stable, with an energy of -6.18 eV below the reference, and when a Zn atom at the bridge site was allowed to relax, it moved to this position. The *hcp* position was however no longer stable at this coverage. The other top site above Zn (Figure 66) distorted slightly and an energy of -6.07 eV below the reference was calculated. The configuration that had the lowest energy at this coverage was a very complicated structure where two of the Zn adatoms occupy bridge sites, while the other two are in slightly distorted positions of *hcp* and *fcc* respectively (Figure 67). This configuration had an energy of -6.35 eV below the reference. A similar configuration with two Zn adatoms in distorted *fcc* and the other two in distorted *hcp* had an energy of -6.30 eV below the reference. A few other exotic configurations were tested but they relaxed to similar structures. At this coverage it is difficult to predict the most energetically favorable configurations, and it is a possibility that there are arrangements with lower or degenerate energies. Figure 68 shows the calculated surface structure at 1 ML coverage of Zn.

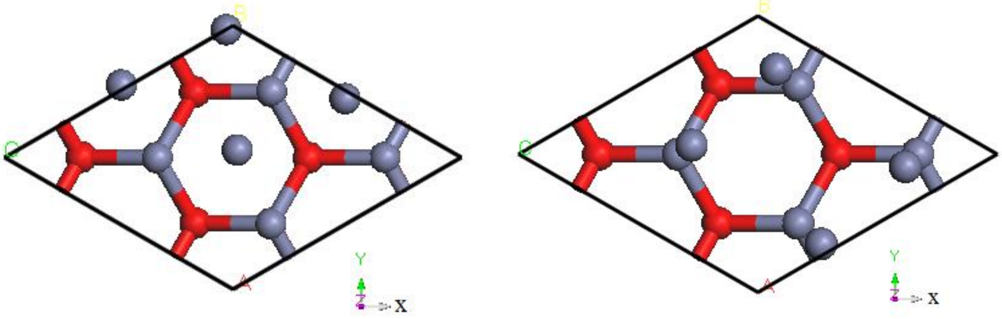

Figure 66: Two of the tested surface configurations for 1 ML coverage of Zn. The left image shows the relaxed structure of the *fcc* configuration, which is slightly distorted. The right image shows quite strongly distorted Zn adatoms in the top site configuration after relaxation.

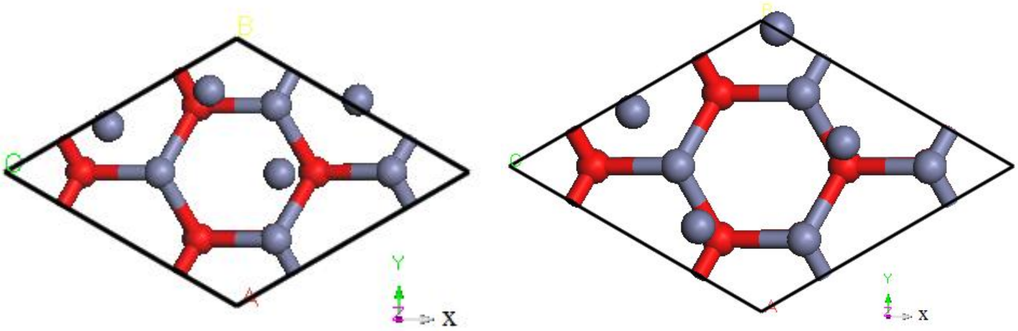

Figure 67: The two most stable calculated configurations at 1 ML coverage of Zn on the ZnO(0001) surface. The configuration on the left image has a slightly lower energy with the difference being that the right one has two Zn adatoms in *hcp* positions, while the left one has only one. The other adatoms are in distorted *fcc* or bridge sites.

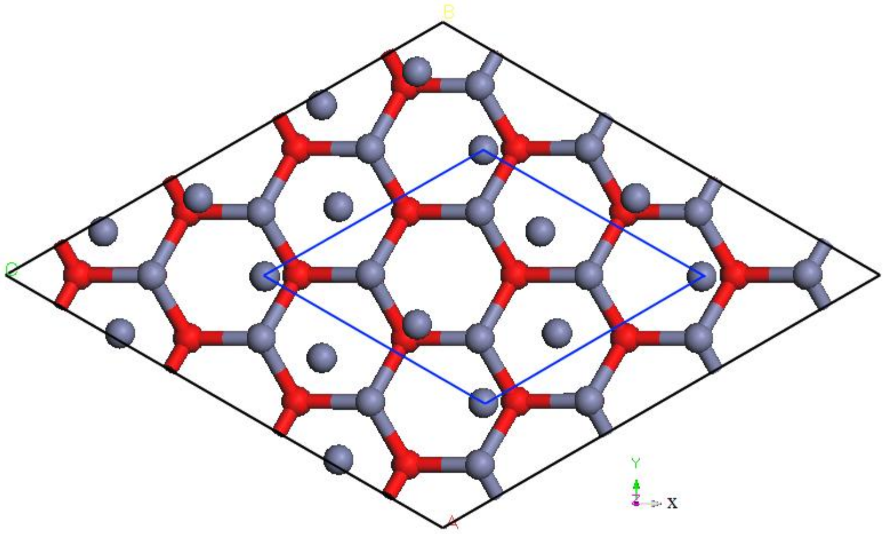

Figure 68: The calculated ZnO(0001)-(2×2)-Zn adatom surface structure for 1 ML coverage of Zn.

Table 12 summarizes the presented data in chapter 5.2.

Table 12: Calculated adsorption energies of Zn in various binding orientations for three different coverages on ZnO(0001)

	Change relative to unbonded configuration (eV)		
Binding orientation	¼ ML	½ ML	1 ML
vertical above Zn	-0.49	-2.76	-6.07
hcp	-0.55	-2.79	Not stable
fcc	Not stable	-2.85	-6.18
bridge	-0.60	-2.85	Not stable
bridge + hcp	-	-	-6.35
fcc + hcp	-	-	-6.30

7.3 ZnO(000-1) Surface in O_2 Atmosphere

7.3.1 ¼ ML Coverage of O_2 on ZnO(000-1)

The calculations done on the ZnO(000-1) surface show that O_2 is repelled from the surface after relaxation (Figure 69). Single O adatoms are however able to bind to the surface at the top site directly above the substrate O atoms (Figure 70). The energy of the configuration was calculated to be -1.37 eV below the reference. The *fcc, hcp* and various bridge sites were tested, but all configurations with single O adatoms either changed into this configuration upon relaxation or moved away from the surface. With every second topsite covered by O adatoms, the calculated surface structure for ¼ ML coverage of O_2, which corresponds to ½ ML coverage of O, is the ZnO(0001)-(2×1)-O surface structure.

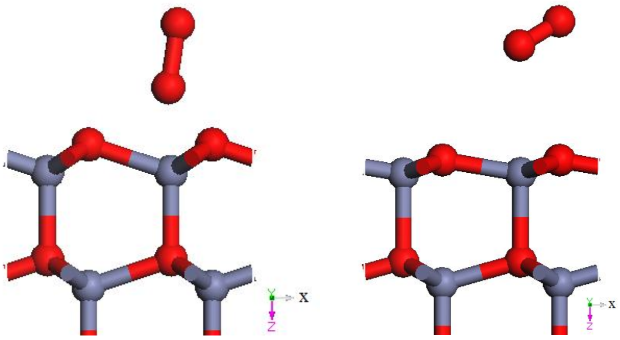

Figure 69: Two dimensional images of O_2 on the ZnO(000-1) surface. The left image shows the tested configuration before relaxation while the right image shows the relaxed structure. The O atoms in the first layer contract slightly inward while the O_2 molecule is repelled from the surface.

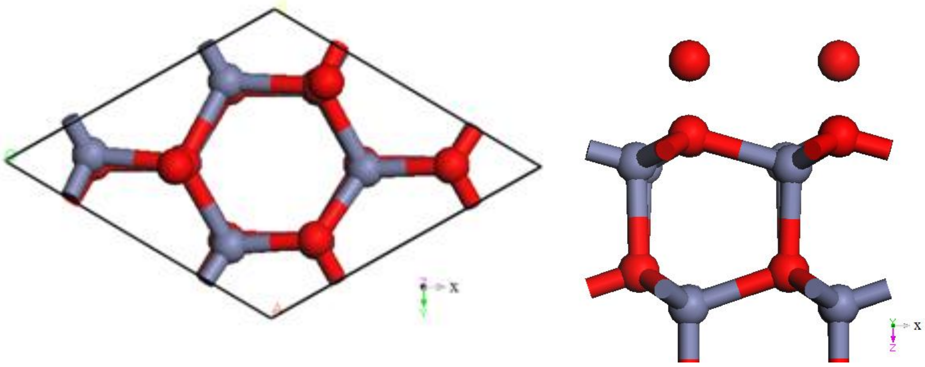

Figure 70: Two dimensional images of O adatoms bonded to topsites on the ZnO(000-1) surface. The calculations suggest that this is the only stable configuration on the ZnO(000-1) surface at ½ ML coverage of O on the surface, which corresponds to ¼ ML of O_2.

7.3.2 ½ ML Coverage of O_2 on ZnO(000-1)

At ½ ML coverage of O_2, no configuration was found with a lower energy than the reference, indicating that oxygen actually desorbs from the surface at this coverage. Two metastable configurations were however found for dissociated oxygen. The configuration with the lowest energy has O atom positioned at an angle above the O-Zn bond (Figure 71), and can be considered as a strongly distorted topsite configuration. The energy is calculated to be 5.17 eV above the reference. The undistorted topsite configuration to the right in Figure 71 was also metastable with an energy of 5.48 eV above the reference. Both energies are significantly larger than the reference, in which two O_2 molecules are positioned far away from the surface. Any perturbation is thus likely to cause the O adatoms to form O_2, which in turn is likely to desorb from the surface. A careful calculation of dissociated O adatoms in *fcc* positions caused two of the O adatoms to desorb and although the calculation did not converge after 200 iterations, it is quite safe to assume that a coverage of more than ¼ ML of O_2 on the ZnO(000-1) surface is energetically unfavorable. A summary of the results from chapter 7.3 can be seen in Table 13.

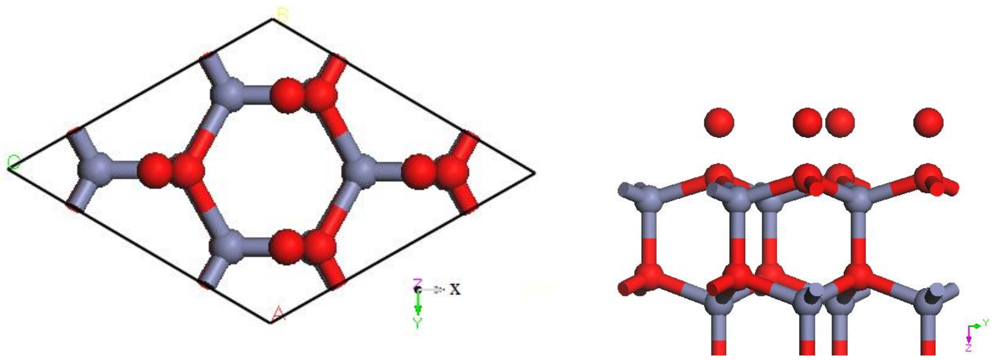

Figure 71: Two metastable configurations of dissociated oxygen on the ZnO(000-1) surface. The left image shows O adatoms positioned above the O-Zn surface bond, while the right shows O adatoms on topsites above O surface atoms. Both configurations have a higher energy than the reference and consequently unstable.

Table 13: Calculated adsorption energies of O_2 for two coverages on ZnO(000-1)

	Change relative to unbonded configuration (eV)	
Binding orientation	¼ ML*	½ ML*
dissociated topsite	-1.37	5.48
dissociated distorted topsite	-	5.17

* The coverages of dissociated oxygen are larger by a factor of two.

7.4 ZnO(000-1) Surface in Zn Atmosphere

7.4.1 ¼ ML Coverage of Zn on ZnO(000-1)

Of the tested configurations, both the *fcc* and the topsite configurations were the most stable, with both having an energy of -6.70 eV below the reference, and are thus degenerate. The *hcp* position lies several eV lower, with an energy of -3.22 eV below the reference. The structures can be seen in Figure 72. The difference is most likely caused by the interaction between the Zn adatom and the lower lying Zn. The repulsion between these causes the lower lying Zn to contract further into the material, which results in an elongation in the bonds between Zn and the O atoms in the same layer. This elongation is unfavorable and the configuration has thus a higher energy than the other two as the Zn adatom in these positions do not cause the same kind of strain on the bonds between the surface atoms. With every fourth *fcc* or topsite filled, the calculated surface structure at ¼ ML coverage of Zn adatoms is thus predicted to be ZnO(000-1)-(2×2)-Zn.

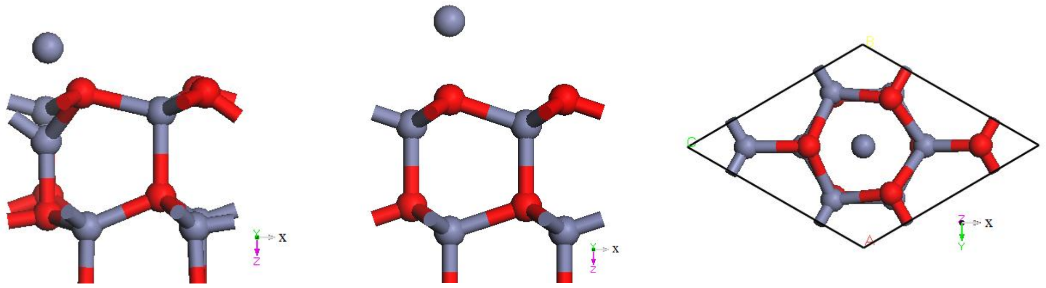

Figure 72: Three stable configurations of Zn adatom on the ZnO(000-1) surface. The left image shows Zn in the *hcp* position, the middle shows Zn on the topsite above oxygen and the right one shows Zn in the *fcc* position. The topsite and *fcc* are both equally stable while the *hcp* causes strain in the level below and has a higher energy.

7.4.2 ½ ML Coverage of Zn on ZnO(000-1)

At ½ ML coverage of Zn, only two stable configurations were found. The most stable configuration was calculated to be a mix where 50% of the Zn adatoms occupy *fcc* positions and the other 50% occupy an unusual position, in which the Zn adatom lies above the bond between a Zn and an O surface atom as shown to the right in Figure 73. The figure shows how the Zn adatoms move from the tested configuration, in which the Zn adatoms are positioned vertically above the O surface atoms, and then move to the more stable configuration upon relaxation. The total energy of this configuration was calculated to be -4.25 eV below the reference. The *hcp* configuration also changed to this arrangement upon relaxation, which is a quite strong indication that this is the most stable configuration at this coverage.

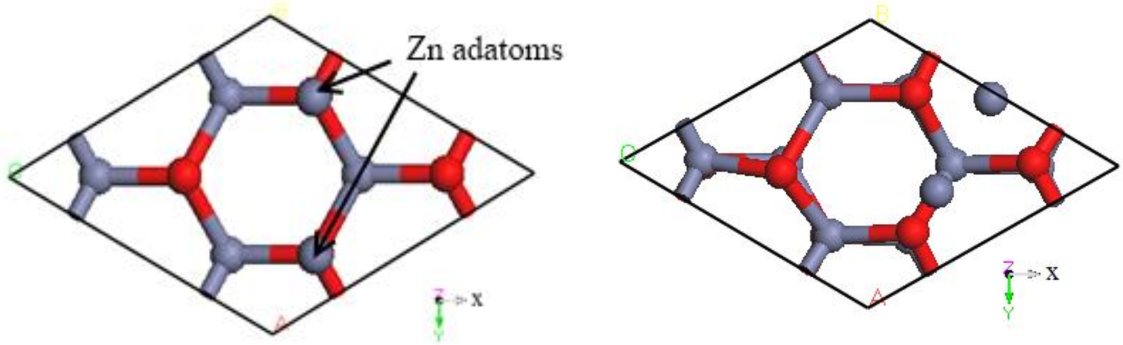

Figure 73: The left image shows the unrelaxed configuration in where the Zn adatoms were positioned above O surface atoms. The right image is taken after relaxation and shows that the Zn adatoms prefer a bonding configuration in which one of the Zn adatoms occupies a *fcc* position while the other occupies a position above one of the bonds between the Zn and O on the surface.

The *fcc* configuration was the only other stable position that was found, and was calculated to have an energy of -3.98 eV below the reference. The calculated surface structure for ½ ML coverage of Zn on this surface, is thus the ZnO(000-1)-(2×2)-Zn shown in Figure 74.

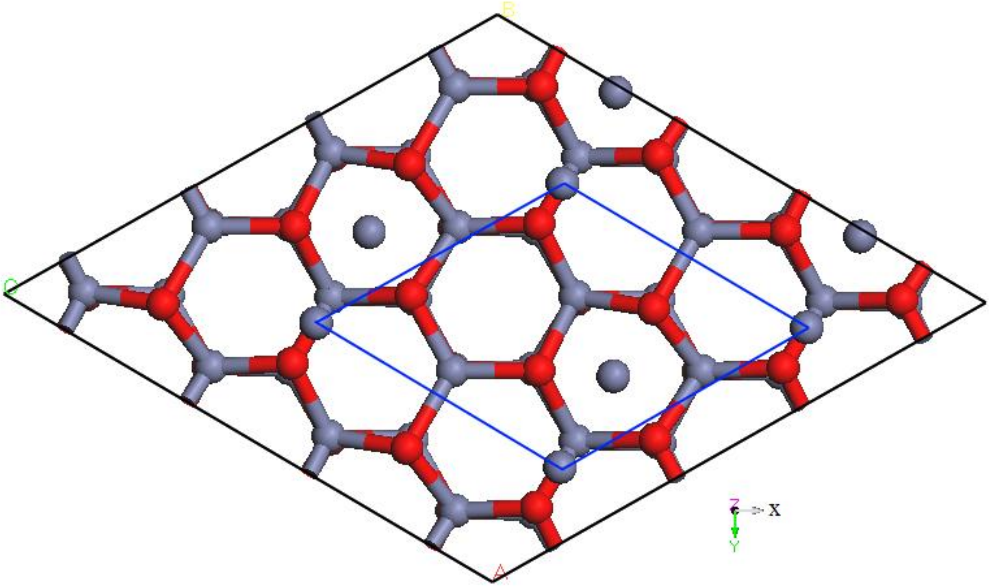

Figure 74: The calculated ZnO(000-1)-(2×2)-Zn adatom surface structure for ½ ML coverage of Zn.

7.4.3 1 ML Coverage of Zn on ZnO(000-1)

The first configuration that was tested was the one that was most stable one for ½ ML (Figure 73). This configuration was however no longer stable and changed into a strongly distorted top site configuration upon relaxation, as can be seen to the left in Figure 75. The energy of this configuration was -5.34 eV below the reference. The configuration with the lowest energy can be seen to the right. In this configuration one of the Zn adatoms is positioned on a top site while the other three are in a sort of bridge like position between two Zn surface atoms and one O surface atom. The energy of this configuration was calculated to be -5.41 eV below the reference. A configuration that was quite similar to the one calculated to be the most stable at ½ ML was found. In this configuration 75% of the Zn adatoms occupy the position above the Zn-O bond, while 25% are in a top site position above an O surface atom. The energy of this configuration was calculated to be -5.37 eV below the reference and can be seen in the middle of Figure 75. The difference between all these configurations are within 0.07 eV from each other and all of them are likely to present at higher temperatures, which could make epitaxial growth difficult.

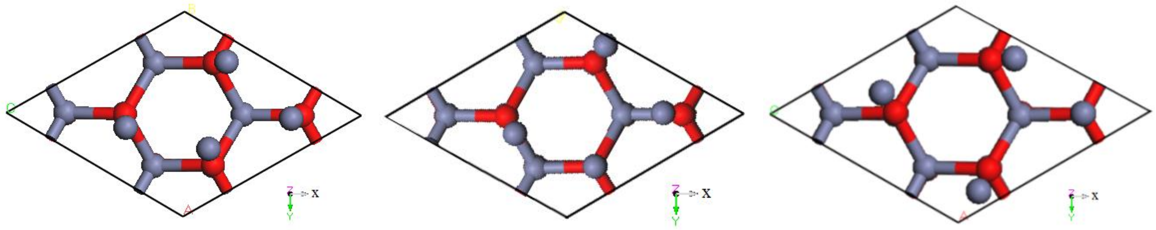

Figure 75: Three nearly equally stable configurations of Zn on the ZnO(000-1) surface. The left image has Zn adatoms positioned in strongly distorted topsites and has the largest energy of the three configurations. The middle configuration has ¾ of the Zn adatoms positioned above the Zn-O bond while ¼ of the Zn adatoms are positioned at the top site directly above O. The most stable configuration can be seen to the right. The configuration is very similar to the one in the middle, except that the Zn adatoms that were positioned above the Zn-O bond are rotated 180° around the O surface atom so that they no longer are positioned above the bond, but instead occupy a sort of bridge site between two Zn surface atoms.

A summary of the results shown in chapter 7.4 are presented in Table 14.

Table 14: Calculated adsorption energies of Zn in various binding orientations for three different coverages on ZnO(000-1)

	Change relative to unbonded configuration (eV)		
Binding orientation	¼ ML	½ ML	1 ML
topsite above O	-6.70	Not stable	-5.34 (distorted)
hcp	-3.22	Not stable	Not stable
fcc	-6.70	-3.98 (distorted)	Not stable
½ fcc + ½ Zn-O bond	-	-4.25	Not stable
¼ topsite + ¾ Zn-O bond	-	-	-5.37
¼ topsite + ¾ bridge	-	-	-5.41

8 Discussion

While some of the specific results have already been discussed to some extent, this chapter will address some general trends observed and possible explanations for these, in addition to possible sources of error which could affect the results.

8.1 Chemical Vapour Transport of ZnO and ZnS

As previously mentioned, the overall aim with the CVT experiments was to produce single crystals suitable for testing the SXRD configuration and as possible substrates for subsequent thin film depositions. For these applications, the crystals should be as large and pure as possible.

The first ZnO crystals that were produced (880-900 ^{o} C), were grown in the hot end of the ampoule, which suggests that HCl was the dominating transport agent. If H_2 had been the dominating transport agent, the crystals would have been grown in the cold end. Even though the crystals were small, it proved that transport with HCl as transport agent was possible in the temperature range. The second experiment was carried out at a higher temperature (940-950 ^{o} C), i.e. in the range where the drop in partial pressure of $ZnCl_2$ is most significant (Figure 15). The calculations suggest that transport should happen both ways in equal amounts; however as the first transport experiment clearly yielded a significant amount of crystals at the hot end and none in the cold, it is likely that the calculated thermodynamic values are slightly off, and transport of elementary Zn can possibly be neglected. This assumption was also supported by the second transport experiment, as once again the crystals were grown in the hot end. Around 2/3 of the starting material was transported, which also is significantly more than what the calculations done in Appendix IV suggest. If the increase in partial pressure of Zn in the temperature range is incorrect and that it in reality first begins at a higher temperature, then it is also possible that the decrease in partial pressure of $ZnCl_2$ is affected by this and thus the change in partial pressure used in the calculation is likely to be too small. It seems however unlikely that the partial pressure is off by a factor of 10 and other parameters are also likely to affect the results.

Another aspect that could affect the results could be that the thermocouple used to measure the temperature was not sufficiently calibrated, or was positioned slightly off from the ampoule, so that the measured temperature was lower or higher than the actual temperature inside the ampoule. Figure 76 shows a diagram of the actual temperature in a similar transport furnace as a function of distance from the opening as previously reported by O. Nilsen (*87*). The temperatures were measured with a different thermocouple than used by the furnace. As the ampoules used in the current experiment were quite large, they barely fit into the transport furnace and consequently it is likely that the end of the ampoule where the feed material was positioned was significantly colder than the actual thermocouple showed. If the end of the ampoule containing the feed material is positioned too close to the opening, the temperature gradient will be from cold to hot for the first 15 cm. This could imply that the temperature gradient where the feed material was positioned was in the wrong direction for the first experiment. In the second experiment, the ampoule was turned around however, and the crystals were still grown at the hot end so it is unclear whether this has any effect on the transport direction. In addition, the first transport experiment was done simultaneously with both an ampoule of ZnO and one with ZnS in the same furnace. The ZnS crystals were grown at the cold end, while the ZnO crystals were grown at the hot end. If the ampoule was colder at the end with the feed material and hotter towards the middle, then ZnS should not have been transported to the other side either. As the transport furnace used in this experiment is a different one, it could also be that the temperature was higher that what the thermocouple displayed. Looking at the results, it seems quite likely that the gradient was much larger than anticipated. If this is the case, then the change in partial pressure of $ZnCl_2$ would be higher and this would increase the amount of transported material and could explain why the amount of crystals produced exceeded the calculated amount for both ZnO and ZnS.

The first produced ZnO crystals were nonetheless of high structural quality, which suggested that the temperature range was still good in order to produce high quality crystals. Their size was too small for being used as substrates though, which is mainly attributed to the fact that they grew in contact with the feed material. For this reason, the second attempt to grow ZnO crystals was done in a different manner. Back transport of the remaining powder along the ampoule walls was carried out and a lower temperature gradient (10 °C) and a longer transport time was chosen in order to improve the size of the single crystal domains. The temperatures were increased to better match the window in which the decrease in partial pressure $ZnCl_2$ was calculated and to see whether the transport would be endothermic again. The results show that these measures improved the size of the crystals significantly, although in order to produce crystals of adequate sizes for the use as substrates, the process needs to be scaled up, i.e. more feed material should be used (at least 3g), with slightly more transport material in addition to an even longer transport duration. The ampoule also needs to be able to withstand the increased pressure that more material would imply and a different geometry that forces growth in only one direction could be applied.

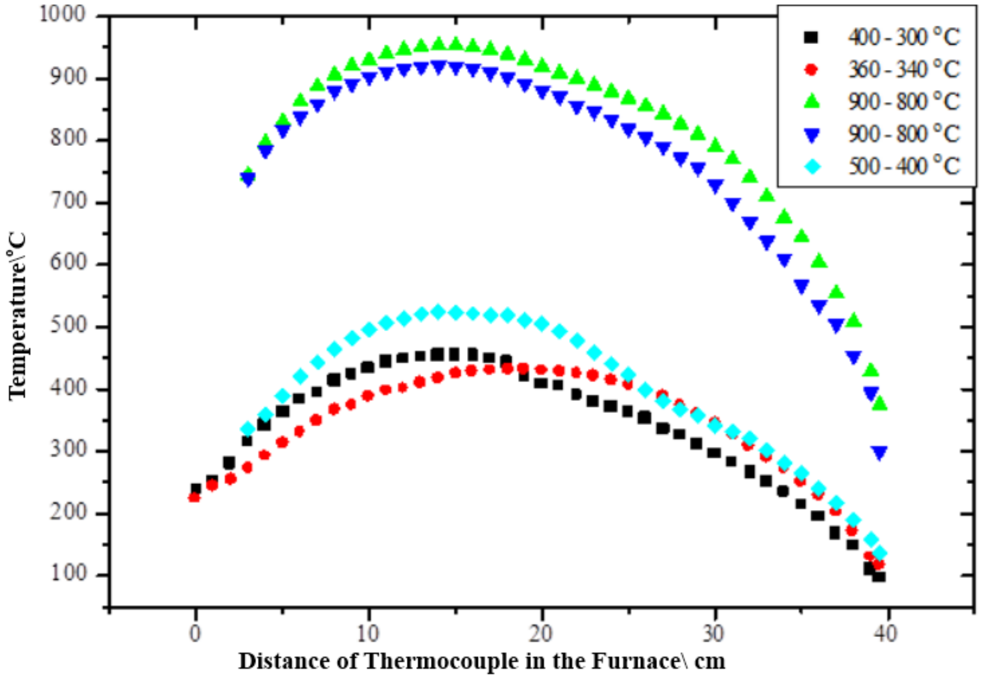

Figure 76: Actual temperatures in a similar transport furnace as a function of distance. The legend in the top right shows the input temperature for the various tests.

The EDS data obtained indicate that ZnO crystals produced are also chemically pure, although EDS is not the best technique for analyzing impurity concentrations and further investigation needs to be done in order to truly facilitate whether coating the ampoules with Zn has an effect on the Si contamination of the crystals. The fact that it is possible to make uniform thin films by sublimation of Zn in an open ampoule in less than two days is however quite significant and might be worthwhile to investigate further.

The observation that the produced crystals of ZnS were of poor structural quality could be an indication that the temperature gradient used (20 ° C) in this work was not optimal, and a significantly smaller temperature gradient at the beginning of the experiment is likely to improve the quality of the produced crystals. Back transport was not carried out for the CVT of ZnS, and remaining ZnS powder might have affected the quality of the crystals. If the coating process affected the growth of ZnS is not clear, but it is possible that contamination of ZnO had an effect on the crystallinity of the grown ZnS crystals as well, although ZnO should be transported to the other side as shown by the other experiment. The yellow fluorescent glow in the quartz wool noted during the coating process is a strong indication that the ampoules are coated with ZnO, which is more reactive than the originally desired Zn_2SiO_4 and it is quite probable that this could have an effect on the grown ZnS crystals. Comparing crystals prepared with and without coated ampoules could consequently be of interest.

The overall results from the CVT experiments produced suitable crystals for exploring the possibilities of the SXRD experiments; however, the crystals were not sufficiently large to be used as suitable substrates for depositions.

8.2 Thin Film Setup for SXRD

The results obtained in this study show that the thin film setup developed in this study is a versatile and powerful tool for analyzing epitaxial thin films. The Co_3O_4 on Al_2O_3 system shows how the technique can be used to determine crystallinity and growth directions, while the MnO_2 on MgO system shows how thin film texture can be determined. While most information obtained in this study can be obtained with other techniques, there are some advantages by using SXRD. Basically no sample preparation is needed and most samples can be measured in less than an hour. While organic samples may be damaged by the strong radiation, the technique is non-destructive for all other samples, which is one of the main advantages. The ability to study specific reflections at very high resolution and without instrumental broadening makes it possible to determine fine details about texture or crystallinity, otherwise impossible or difficult to find with other techniques. The open system also allows for instance *in situ* temperature measurements and other devices could also be installed if needed. The *in situ* ALD measurements done at the advanced photon source in Argonne could most likely be done at the ESRF with this setup if a new slit system with finer control of the beam size could be implemented at the station. The software is however a significant problem at the moment, as it was not designed to treat thin film measurements and exporting the data into a presentable format is currently a very time consuming process. This should however be fairly easy to remedy and will most likely not be a problem in the future.

A smaller spot size of the beam could also be used to obtain diffraction spots from surface or interface, although for thin film experiments, only known surface structures can be indexed as it is most likely impossible to obtain only surface diffraction data with this setup, and untangling these reflections from both thin film and substrate could become extremely difficult. In addition, new software, or modification to the current software employed is needed in order to analyze crystal truncation rods visible in several thin film experiments, as these hold a lot of interesting information that could make the technique a lot more useful for studying surfaces. Beam lines dedicated to surface diffraction are still better suited for such an analysis, however being able to obtain similar data at the SNBL is a huge advantage as the group has several other activities that may be carried out at this station. Being able to use 1-2 hour slots to do a complete thin film and surface analysis, may be possible to do in-between other experiments and consequently the highly expensive beam time may be used more efficiently.

8.3 *Ab Initio* Calculations

The DFT calculations done on ZnO in vacuum confirm several of the results obtained previously on the ZnO(0001) and ZnO(000-1) surfaces (*66, 67, 69*). By capping the bottom of a slab with hydrogen, it was possible to reproduce the experimentally observed difference in surface energy (*71*) of these two surfaces and the Zn terminated ZnO(0001) surface was calculated to be the most reactive. The calculated surface energies agree well with previously calculated results and agree qualitatively with experimental results obtained as well.

While the calculated bond length contraction of the first layers agrees well with previous calculations, the outward relaxation observed experimentally for the top layer of the Zn terminated surface was not possible to reproduce. By keeping the middle layers of the slab fixed, it was however possible to reduce the contraction to an insignificant amount.

The calculations done on the ZnO(0001) surface in O_2 atmosphere suggest that the oxygen dissociation is exothermic at low coverages (¼ ML), but as the coverage is increased to ½ ML of O_2, the molecular configurations become more stable and the dissociated oxygen changes to the flat *fcc* configuration. At higher temperatures, a vertical configuration might however be more stable, but molecular dynamics would need to be employed in order to validate this. The driving mechanism behind the formation of the molecular configuration requires extensive work in order to determine, but is likely to be connected with the surface spin moment. At low coverage of oxygen there is an electron deficiency as each oxygen adatom has two valence electron holes, which are likely to be fully polarized. At higher coverage, these polarized electron holes are paired into covalent O-O bonds and could be the driving force for the molecular configuration.

For the ZnO(0001) surface in Zn atmosphere, the calculations have shown a bridge configuration to be the most stable at low coverages (1/4 ML), which remains stable until half the surface is covered with Zn adatoms. Increasing the coverage above this value however, makes the configuration become unstable and more exotic surface structures like the combination of *hcp* and bridge sites become more stable. This could indicate that the adsorbate-surface interactions are approaching the same magnitude as the adsorbate-adsorbate interactions and that the underlying substrate structure has less influence of the surface structure.

In oxygen atmosphere, the calculations of the ZnO(000-1) surface have demonstrated that oxygen does not adsorb molecularly, but that the dissociation of oxygen on the surface is exothermic for low coverages. For higher coverages, the calculations show that the adsorption of oxygen is not energetically favorable and thus the only stable configuration of the tested coverages was found when O adatoms covered half the top sites above the O atoms on the surface. This can possibly be attributed to the already accumulated negative charge on the surface and possibly the coordination of oxygen. On the surface, oxygen is connected to three Zn, opposed to four in the bulk. This suggests that an electron deficient oxygen adatom could be able to bond to the oxygen on the surface in the top site in order to compensate a dangling bond. An oxygen molecule on the other hand would not be able to completely compensate the dangling bonds and could be a reason why the O_2 molecule is not adsorbed to the surface. As the oxygen coverage is increased it is likely that the oxygen adatoms begin to interact with each other and the formation of molecular $O_{2,}$ as seen for the ZnO(0001) is more favorable. As adsorbed O_2 on the surface is unstable however, the calculation is unable to find the final stable configuration and instead a configuration with positive energy with disordered O adatoms on the topsite is found.

The calculations done on the ZnO(000-1) surface in Zn atmosphere have shown that Zn has two configurations at ¼ ML coverage that are degenerate (*fcc* and top sites), but at coverages above ½ ML, the *fcc* configuration is beginning to distort and the top site is unstable. As the coverage is increased even further (1 ML), the *fcc* configuration becomes completely unstable as well and several complex structures, all with very similar energies to each other, are calculated to have the lowest energies at this coverage. It thus becomes challenging to predict which configuration will be the most stable at temperatures above 0 K. At 0 K though, the calculations indicate that a configuration where ¼ of the adsorbed Zn adatoms occupy topsites and ¾ occupy bridge sites is the most stable.

A general trend seems to be that triangular pits are favorable adsorption sites at low coverage, while at higher coverage; the Zn adatoms are localized closer to the oxygen surface atoms, which could be an indication that a continuation of the structure becomes more favorable. As the coverage is increased however, adatom-adatom interactions become more pronounced and this could also result in the complex surface structures, similar to what was observed on the ZnO(0001)-Zn surface. It could be of interest to see what happens with the Zn adatoms when a new layer of oxygen is positioned on top of them and compare the two layers with the bulk structure.

9 Concluding Remarks

The first goal of this study was to grow high quality single crystals of ZnO and ZnS by the use of chemical vapour transport. While it has been demonstrated that high quality single crystals of ZnO can be grown with the use of the CVT by using NH_4Cl as feed material for the transport agent (H_2 and HCl), the same can not be said for the grown crystals of ZnS. A lower temperature gradient needs however to be tested before ruling out HCl as a good transport agent for the growth of high quality ZnS single crystals. The affect the coating has on the produced crystals also needs to be investigated.

The second goal was the modeling of the polar surfaces of ZnO in vacuum, for varying concentrations of oxygen and zinc. This has been performed successfully and possible surface structures have been found for different coverages of both zinc and oxygen at 0 K. While the extent of this study has been limited, a sufficiently large number of structures have been tested in order to obtain qualitative information about the structural changes as the coverage of oxygen or zinc is increased on the polar surfaces of ZnO.

The last goal was to establish collaboration with the SNBL and to find a method to routinely analyze thin films. This goal has been achieved and discussions about future installments for *in situ* atomic layer deposition have already begun. While it has been demonstrated that the technique already is able to find information which is hidden in regular XRD, new slit systems with finer control of the beam size as well as software to interpret information from crystal truncation rods could make the setup a powerful tool in order to analyze thickness and roughness of thin films. This in combination with *in situ* ALD, could give much better insight to the growth of thin films and shed light on some difficult processes.

Future Work

Due to the broad nature of this study, there are quite a lot of options available for further study in the future. The coating process used for the quartz ampoules had quite interesting results and investigating the process further with different samples and varying parameters could help understand the benefits and limitations of the technique as well possible applications. Obtaining uniform thin films of ZnO on Si substrates is not easily done with techniques like ALD, and the other possibility of Zn reacting with the Si substrate is also of major interest for the silicon industry.

In order to exploit the possibilities of SXRD of thin films, *in situ* ALD measurements should be carried out in the future. Growing thin films, while doing XRF, SXRD or reflectometry as well as having control of temperature, will give a vast set with information otherwise extremely tedious or impossible to obtain.

Doing experimental work that could be complimentary to the modeling done on the polar surfaces of ZnO could be of interest in order to verify the calculated results or to determine which surface structure is dominating in the cases where several possibilities were found. The most interesting path to follow with calculations would be to add additional layers on the structures already found and see how this affects the underlying layers. Expanding the supercell used for the calculation will always also be an option, in order to be able to test more coverages and determine more precisely when changes in the surface structure occur. In order to calculate the stable surface structure configurations at higher temperatures, molecular dynamics could be implemented. Investigating the other common surface terminations of ZnO is also of interest with respect to understanding the growth of ZnO.

References

1. Coleman, Jagadish, in *Zinc Oxide Bulk, Thin Films and Nanostructures Processes, Properties and Applications,* S. P. Chennupati Jagadish, Ed. (Elsevier, Oxford, Kidlington, 2006), pp. 3-17.

2. A. Mycielski, L. Kowalczyk, A. Szadkowski, B. Chwalisz, A. Wysmolek, R. Stepniewski, J. M. Baranowski, M. Potemski, A. Witowski, R. Jakiela, A. Barcz, B. Witkowska, W. Kaliszek, A. Jedrzejczak, A. Suchocki, E. Lusakowska, E. Kaminska, The chemical vapour transport growth of ZnO single crystals. *Journal of Alloys and Compounds* **371**, 150-152 (2004).

3. V. Avrutin, G. Cantwell, J. Zhang, J. J. Song, D. J. Silversmith, H. Morkoc, Bulk ZnO: current status, challenges, and prospects. *Proc. IEEE* **98**, 1339-1350 (2010).

4. R. Nitsche, H. U. Bölsterli, M. Lichtensteiger, Crystal growth by chemical transport reactions—I: Binary, ternary, and mixed-crystal chalcogenides. *Journal of Physics and Chemistry of Solids* **21**, 199-205 (1961).

5. S. Ito, T. Shimazaki, M. Kubo, H. Koinuma, M. Sumiya, Communication: The reason why +c ZnO surface is less stable than -c ZnO surface: First-principles calculation. *Journal of Chemical Physics* **135**, 241103/241101-241103/241104 (2011).

6. O. Nilsen, O. B. Karlsen, A. Kjekshus, H. Fjellvag, Simulation of growth dynamics for nearly epitaxial films. *Journal of Crystal Growth* **308**, 366-375 (2007).

7. D. L. Smith, *Thin-Film Deposition Principles & Practice*.McGraw-Hill, inc. , United States of America, ed., 1995, pp. 616.

8. W. M. Klipstein, S. K. Lamoreaux, E. N. Fortson, Observation of spontaneous spin polarization in an optically pumped cesium vapor. *Phys. Rev. Lett.* **76**, 2266-2269 (1996).

9. O. Dulub, U. Diebold, G. Kresse, Novel Stabilization Mechanism on Polar Surfaces: ZnO(0001)-Zn. *Physical Review Letters* **90**, 016102/016101-016102/016104 (2003).

10. J. P. Borah, J. Barman, K. C. Sarma, Structural and optical properties of ZnS nanoparticles. *Chalcogenide Letters* **5**, 201-208 (2008).

11. S. Ilican, Y. Caglar, M. Caglar, B. Demirci, Polycrystalline indium-doped ZnO thin films: preparation and characterization. *Journal of Optoelectronic and Advanced Materials* **10**, 2592-2598 (2008).

12. M. Bass, *Handbook of Optics: Devices, Measurements, and Properties*.Handbook of Optics,McGraw-Hill, 2, 1994, vol. 2.

13. M. Bass, C. DeCusatis, G. L. Jay Enoch, V. N. Mahajan, V. Lakshminarayanan, E. V. Stryland, C. MacDonald, *Handbook of Optics: Optical Properties of Materials, Nonlinear Optics, Quantum Optics*.McGraw-Hill, 3, 2009, vol. 4, pp. Chapter 5.

14. K. Yoshio, A. Onodera, H. Satoh, N. Sakagami, H. Yamashita, Crystal structure of ZnO:Li at 293 K and 19 K by x-ray diffraction. *Ferroelectrics* **264**, 133-138 (2001).

15. X.-R. Chen, X.-F. Li, L.-C. Cai, J. Zhu, Pressure induced phase transition in ZnS. *Solid State Community* **139**, 246-249 (2006).

16. M. C. Ball, Chemical transport reactions. *Journal of Chemical Education* **45**, 651 (1968/10/01, 1968).

17. H. Schäfer, H. Jacob, K. Etzel, Chemische Transportreaktionen. I. Über den Transport des Bodenkörpers im Temperaturgefälle mit Hilfe heterogener Gleichgewichte. *Zeitschrift für anorganische und allgemeine Chemie* **286**, 27-41 (1956).

18. G. A. Somarjai, *Introduction to Surface Chemistry and Catalysis* Wiley, Department of Chemistry, University of California, Berkeley, California, ed., 2010, pp. 39-280.

19. I. H. Hung, Y.-R. Lan, T.-H. Wu, Z.-C. Feng, N. Li, H.-B. Yu, I. T. Ferguson, W.-J. Lu, Nanoscale InGaN/GaN on ZnO substrate for LED applications. *Proceedings of SPIE* **7422**, 74220K/74221-74220K/74212 (2009).

20. Y. Waseda, E. Matsubara, K. Shinoda, *X-Ray Diffraction Crystallography Introduction, Examples and Solved Problems*.Springer, Berlin, Heidelberg, ed., 2011, pp. 1-15.

21. J. Als-Nielsen, D. McMorrow, *Elements of Modern X-ray Physics* Wiley, United Kingdom, ed. 2nd., 2011 pp. 29-65, 275-300.

22. F. Krumeich, *Bragg's Law of Diffraction*, 2009, Available at: http://www.microscopy.ethz.ch/bragg.htm

23. M. Meier, *Measuring Crystallite Size Using X-ray Diffraction, The Williamson-Hall Technique*, Davis University of California 2005, Available at: http://www.kstreetstudio.com/science/experiments/files/XRD-CSize2.pdf

24. C. Li-Dong, *Soft-x-ray spectroscopy probes nanomaterial-based devices*, SPIE Newsroom 2007, Available at: http://spie.org/x15809.xml?pf=true&ArticleID=x15809

25. H. Wiedmann, *Synchrotron Radiation*.Springer, Berlin Heidelberg, ed., 2003, pp. 2-5.

26. A. P. Hitchcock, J. J. Neville, Applications of synchrotron light to physics and chemistry. *Physics in Canada* **55**, pp.191-198 (1999).

27. A. F. Craievich, Synchrotron SAXS studies of nanostructured materials and colloidal solutions. A review. *Materials Research Bulletin (Sao Carlos, Braz.)* **5**, 1-11 (2002).

28. B. D. Cullity, S. R. Stock, *Elements of X-ray Diffraction*.Addison-Wesley, United Kingdom, ed., 1956, pp. 531.

29. A. W. Hull, A new method of X-ray crystal analysis. *Physical Review Letters* **10**, 661-696 (1917).

30. B. Rupp, Phasing Techniques: The Phase Problem - A Basic Review. *Web Resource: Ruppweb.org*, (2009).

31. M. Dunlap, *How ESEM Works*, University of California Merced 2007, Available at: https://imf.ucmerced.edu/downloads/esem.pdf

32. J. Goodge, *Energy-Dispersive X-Ray Spectroscopy (EDS)*, University of Minnesota-Duluth 2012, Available at: http://serc.carleton.edu/research_education/geochemsheets/eds.html

33. J. C. Vickerman, I. S. Gilmore, *Surface Analysis The Principal Techniques*.Wiley, United Kingdom, ed. 2nd 2009, pp. 666.

34. ParkSystems, *AFM Metrology Considerations of Hard Disk Manufacturing*, 2008, Available at: http://www.parkafm.com/AFM_technology/application_view2.php?id=1271&cate=DataStorage

35. H. Fujiwara, *Spectroscopic Ellipsometry Principles and Applications* Wiley, Tokyo, Japan, ed., 2007 pp. 2-46.

36. G. Weiser, W. Fuhs, H. J. Hesse, Study of polariton resonances in a cyanine dye crystal. *Chemical Physics* **52**, 183-191 (1980).

37. O. M. Løvvik, G. Helgesen, *Lecture notes and summary FYS-MENA 3110/4110*, .Department of Physics University of Oslo, ed., 2009, pp. 21-22, 83-98.

38. E. A. Hylleraas, The energy of the helium atom in the fundamental state. *Physikalische Zeitschrift* **30**, 249-250 (1929).

39. W. Kohn, L. J. Sham, “Self-consistent equations including exchange and correlation effects” (Univ. of California, 1965).

40. R. Bauernschmitt, R. Ahlrichs, Treatment of electronic excitations within the adiabatic approximation of time dependent density functional theory. *Chemical Physics Letter* **256**, 454-464 (1996).

41. W. Kohn, Nobel lecture: electronic structure of matter-wave functions and density functionals. *Reviews of Modern Physics* **71**, 1253-1266 (1999).

42. R. G. Parr, W. Yang, *Density Functional Theory of Atoms and Molecules* International Series of Monographs on Chemistry,Oxford University Press, New York, ed., 1989, vol. 16.

43. R. G. Parr, *Density-Functional Theory of Atoms and Molecules*.Oxford University Press, 1995, pp. 342.

44. G. L. Oliver, J. P. Perdew, Spin-density gradient expansion for the kinetic energy. *Physical Review A* **20**, 397-403 (1979).

45. J. P. Perdew, K. Burke, M. Ernzerhof, Generalized gradient approximation made simple. *Physical Review Letters* **77**, 3865-3868 (1996).

46. M. Toyoda, T. Ozaki, Exchange functional by a range-separated exchange hole. *Physical Review A* **83**, 032515 (2011).

47. Y. Wang, J. P. Perdew, Correlation hole of the spin-polarized electron gas, with exact small-wave-vector and high-density scaling. *Physical Review B* **44**, 13298-13307 (1991).

48. D. S. Sholl, J. A. Steckel, *Density Functional Theory A Practical Introduction*.Wiley, Canada, ed., 2009, pp. 234.

49. R. A. Laudise, A. A. Ballman, Hydrothermal synthesis of zinc oxide and zinc sulfide. *Journal of Physical Chemistry* **64**, 688-691 (1960).

50. T. Sekiguchi, S. Miyashita, K. Obara, T. Shishido, N. Sakagami, Hydrothermal growth of ZnO single crystals and their optical characterization. *Journal of Crystal Growth* **214/215**, 72-76 (2000).

51. N. Sakagami, M. Yamashita, T. Sekiguchi, S. Miyashita, K. Obara, T. Shishido, Variation of electrical properties on growth sectors of ZnO single crystals. *Journal of Crystal Growth* **229**, 98-103 (2001).

52. D. Schulz, S. Ganschow, D. Klimm, M. Neubert, M. Rossberg, M. Schmidbauer, R. Fornari, Bridgman-grown zinc oxide single crystals. *Journal of Crystal Growth* **296**, 27-30 (2006).

53. M. Shiloh, J. Gutman, Growth of ZnO single crystals by chemical vapour transport. *Journal of Crystal Growth* **11**, 105-109 (1971).

54. H. Yan, R. He, J. Pham, P. Yang, Morphogenesis of one-dimensional ZnO nano- and microcrystals. *Advanced Materials (Weinheim, Ger.)* **15**, 402-405 (2003).

55. J. M. Ntep, S. S. Hassani, A. Lusson, A. Tromson-Carli, D. Ballutaud, G. Didier, R. Triboulet, ZnO growth by chemical vapour transport. *Journal of Crystal Growth* **207**, 30-34 (1999).

56. K. Grasza, A. Mycielski, Contactless CVT growth of ZnO crystals. *physica status solidi (c)* **2**, 1115-1118 (2005).

57. M. Mikami, T. Eto, J. Wang, Y. Masa, M. Isshiki, Growth of zinc oxide by chemical vapor transport. *Journal of Crystal Growth* **276**, 389-392 (2005).

58. R. Lauck, Chemical vapor transport of zinc sulfide. *Journal of Crystal Growth* **312**, 3642-3649 (2010).

59. K. Matsumoto, G. Shimaoka, Crystal growth of zinc sulfide and zinc selenide by chemical transport using ammonium chloride as a transport agent. *Journal of Crystal Growth* **79**, 723-728 (1986).

60. C. H. Ma, J. H. Huang, H. Chen, Residual stress measurement in textured thin film by grazing-incidence X-ray diffraction. *Thin Solid Films* **418**, 73-78 (2002).

61. J. R. Levine, J. B. Cohen, Y. W. Chung, P. Georgopoulos, Grazing-incidence small-angle x-ray scattering: new tool for studying thin film growth. *Journal of Applied Crystallography* **22**, 528-532 (1989).

62. J. R. Casanova, E. A. Heredia, C. D. Bojorge, H. R. Canepa, G. Kellermann, A. F. Craievich, Structural characterization of supported nanocrystalline ZnO thin films prepared by dip-coating. *Applied Surface Science* **257**, 10045-10051 (2011).

63. D. D. Fong, J. A. Eastman, S. K. Kim, T. T. Fister, M. J. Highland, P. M. Baldo, P. H. Fuoss, In situ synchrotron x-ray characterization of ZnO atomic layer deposition. *Applied Physics Letters* **97**, 191904/191901-191904/191903 (2010).

64. F. Mo, D. Chernyshov, L. S. Thoresen. (Acta Crystallographica, 2008), vol. A64, pp. C520-C521.

65. W. Knaepen, J. Demeulemeester, D. Deduytsche, J. L. Jordan-Sweet, A. Vantomme, R. L. Van Meirhaeghe, C. Detavernier, C. Lavoie, In situ X-ray diffraction study of thin film Ir/Si solid state reactions. *Microelectronic Engineering* **87**, 258-262 (2010).

66. Y. Zhang, Z. Guo, X. Gao, D. Cao, Y. Dai, H. Zhao, First-principles of wurtzite ZnO (0001) and (0001) surface structures. *Journal of Semiconductors* **31**, 082001/082001-082001/082005 (2010).

67. S.-H. Na, C.-H. Park, First-principles study of the surface of wurtzite ZnO and ZnS - implications for nanostructure formation. *Journal of the Korean Physical Society* **54**, 867-872 (2009).

68. O. Warschkow, K. Chuasiripattana, M. J. Lyle, B. Delley, C. Stampfl, Cu/ZnO(0001) under oxidating and reducing conditions: A first-principles survey of surface structures. *Physical Review B: Condensed Matter and Materials Physics* **84**, 125311/125311-125311/125325 (2011).

69. A. Wander, F. Schedin, P. Steadman, A. Norris, R. McGrath, T. S. Turner, G. Thornton, N. M. Harrison, Stability of Polar Oxide Surfaces. *Physical Review Letters* **86**, 3811-3814 (2001).

70. H. Maki, N. Ichinose, N. Ohashi, H. Haneda, J. Tanaka, The lattice relaxation of ZnO single crystal (0001) surface. *Applied Surface Science* **457**, 377-382 (2000).

71. N. Jedrecy, S. Gallini, M. Sauvage-Simkin, R. Pinchaux, Copper growth on the O-terminated ZnO(0001¯) surface: Structure and morphology. *Physical Review B* **64**, 085424 (2001).

72. Z.-r. Wei, M.-x. Wu, S.-q. Guo, P. Gao, L.-j. Yin, C.-x. Huang, J.-p. Zhang, X.-j. Zhang, G.-y. Dong, Synthesis of ZnO crystals by chemical vapor transport process. *Rengong Jingti Xuebao* **39**, 1261-1264 (2010).

73. H. Schafer, H. Jacob, K. Etzel, Chemical transport reactions. II. The use of the decomposition equilibriums of iron(II) and nickel(II) halides for metal transport in a temperature gradient. *Zeitschrift für anorganische und allgemeine Chemie* **286**, 42-55 (1956).

74. M. Meyer, *PhD thesis: Construction of a multi-purpose X-ray CCD detector and its implementation on a 4-circle kappa goniometer*.Faculty of Science,University of Lausanne, Lausanne, ed., 1998.

75. V. M. Kaganer, Crystal truncation rods in kinematical and dynamical x-ray diffraction theories. *Physical Review B: Condensed Matter and Materials Physics* **75**, 245425/245421-245425/245426 (2007).

76. M. Tabuchi, N. Matsumoto, Y. Takeda, T. Tetsuya, H. Amano, I. Akasaki, Crystal quality and surface structure of sapphire and buffer layers on sapphire revealed by crystal truncation rod scattering. *Journal of Crystal Growth* **189–190**, 291-294 (1998).

77. G. A. Samorjai, Y. Li, *Introduction to Surface Chemistry and Catalysis*.Wiley, New Jersey, ed. 2nd. , 2010, pp. 39-280.

78. K. Fink, Ab initio cluster calculations on the electronic structure of oxygen vacancies at the polar ZnO(000¯1) surface and on the adsorption of H2, CO, and CO2 at these sites. *Physical Chemistry Chemical Physics* **8**, 1482-1489 (2006).

79. M. Losurdo, M. M. Giangregorio, Interaction of atomic hydrogen with Zn-polar and O-polar ZnO surfaces. *Applied Physics Letters* **86**, 091901/091901-091901/091903 (2005).

80. E. Beutel, A. Kutzelnigg, Luminescence analysis. IV. Fluorescence of zinc oxide. *Monatshefte für Chemie* **61**, 69-86 (1932).

81. K. B. Klepper, O. Nilsen, H. Fjellvåg, Growth of thin films of Co3O4 by atomic layer deposition. *Thin Solid Films* **515**, 7772-7781 (2007).

82. K. B. Klepper, O. Nilsen, H. Fjellvåg, Epitaxial growth of cobalt oxide by atomic layer deposition. *Journal of Crystal Growth* **307**, 457-465 (2007).

83. H. Miyashiro, A. Yamanaka, M. Tabuchi, S. Seki, M. Nakayama, Y. Ohno, Y. Kobayashi, Y. Mita, A. Usami, M. Wakihara, Improvement of Degradation at Elevated Temperature and at High State-of-Charge Storage by ZrO2 Coating on LiCoO2. *Journal of The Electrochemical Society* **153**, A348-A353 (2006).

84. R. Ranjan, D. Pandey, W. Schuddinck, O. Richard, M. P. De, L. J. Van, T. G. Van, Evolution of Crystallographic Phases in (Sr1-xCax)TiO3 with Composition (x). *Journal of Solid State Chemistry* **162**, 20-28 (2001).

85. O. Nilsen, S. Foss, H. Fjellvag, A. Kjekshus, Effect of substrate on the characteristics of manganese(IV) oxide thin films prepared by atomic layer deposition. *Thin Solid Films* **468**, 65-74 (2004).

86. T. Klitsner, R. O. Pohl, Phonon scattering at silicon crystal surfaces. *Physical Review B* **36**, 6551-6565 (1987).

87. O. Nilsen, *Kjemisk gasstransport; Beregninger og eksperimenter, med eksempler fra MoS3, Pt og GeO2, Hovedoppgave Universitetet i Oslo*. 1998, pp. 6-15.

88. M. E. Davis, R. J. Davis, *Fundamentals of chemical reaction engineering, Appendix*.McGraw-Hill Higher Education, New York, NY, ed., 2003.

89. H. Banks, *Handout on Diffraction*, Department of Chemistry, Texas A&M University 2002, Available at: http://www.chem.tamu.edu/rgroup/hughbanks/courses/634/handouts/Diffraction.pdf

Appendix I

Chemical Equilibrium – Derivations (*88*)

The basic criterion for equilibrium in a single reaction is:

$$\Delta G = \sum_{i=1}^{N} v_i \mu_i = 0, \tag{A. 1}$$

where ΔG is the Gibbs function, N is the number of components in the system, v_i is stoichiometric coefficient of species i, and μ_i is the chemical potential of species i. The chemical potential is given by:

$$\mu_i = \mu_i^0 + RT \ln a_i, \tag{A. 2}$$

where μ_i^0 is the standard chemical potential of species i in a reference state such that $a_i = 1$ and a_i is the activity of species i, while R is the universal gas constant and T is the temperature.

Generally it is not true that the change in the standard Gibbs function, ΔG^0, is zero and consequently:

$$\Delta G - \Delta G_0 = \sum_{i=1}^{N} v_i (\mu_i - \mu_i^0). \tag{A. 3}$$

By using Equation A. 2, the following expression is obtained:

$$\Delta G - \Delta G_0 = RT \sum_{i=1}^{N} v_i \ln a_i. \tag{A. 4}$$

Consider the following reaction:

$$iA + jB + \cdots = kC + lD + \cdots \tag{A. 5}$$

A, B, C and D are chemical species, while i, j, k and l are coefficients of the reaction. By using Equation A. 4 and Equation A. 5 and that $\Delta G = 0$ at chemical equilibrium:

$$\Delta G_0 = -RT\ln\left[\frac{a_C^k + a_D^l + \cdots}{a_A^i + a_B^j + \cdots}\right] = -RT\ln K, \qquad \text{A. 6}$$

where K is the equilibrium constant. After considering Equation A. 4, the equilibrium constant, K, is thus defined:

$$K = \prod_{j=1}^{N} a_i^{v_i} \qquad \text{A. 7}$$

Differentiation of Equation A. 6 with respect to T gives:

$$\left[\frac{\partial(\frac{\Delta G_0}{T})}{\partial T}\right] = -R\left[\frac{\partial \ln K}{\partial T}\right] \qquad \text{A. 8}$$

The standard Gibbs free energy is given by the relation:

$$\Delta G_0 = \Delta H_0 - T\Delta S_0 = -RT\ln K, \qquad \text{A. 9}$$

where ΔH_0 and ΔS_0 are the standard enthalpy and entropy, respectively. Equation A. 8 can consequently be written as:

$$\left[\frac{\partial(\frac{\Delta G_0}{T})}{\partial T}\right] = -\frac{\Delta H_0}{T^2} \qquad \text{A. 10}$$

Equating Equation A. 8 and A. 10 gives the functional form for the temperature dependence of the equilibrium constant:

$$\left[\frac{\partial \ln K}{\partial T}\right] = \frac{\Delta H_0}{RT^2} \qquad \text{A. 11}$$

The expression may be easier understood by integration and assuming that ΔH_0 is independent of temperature:

$$K = K_0 e^{\frac{-\Delta H_0}{RT}} \qquad \text{A. 12}$$

The equation implies that if ΔH is negative, the reaction is exothermic, while the reaction is endothermic if ΔH is positive.

Appendix II

Calculation of the Pressure inside the Ampoules used for CVT

The ideal gas law gives the pressure inside the tubes:

$$P = \frac{nRT}{V} \qquad \text{A. 13}$$

The volumes, V, of the ampoules are ~26.5 cm^3, while *T* is the temperature, *R* is the universal gas constant, and *n* is the number of moles in the gas phase.

Calculation of number of moles *n* in the gas phase for 0.017 g of NH_4Cl and 1g of ZnO:

In the gas phase NH_4Cl will dissociate to NH_3 and HCl. NH_3 will in turn dissociate to N_2 and H_2. The reaction follows the equation:

$$2NH_4Cl \leftrightarrow N_2 + 3H_2 + 2HCl \qquad \text{A. 14}$$

2 mole of NH_4Cl becomes 1 mole of N_2, 3 moles of H_2 and 2 moles of HCl. There is consequently a tripling in mole numbers in the reaction. The amount of moles NH_4Cl is found by the following equation, where M_{NH_4Cl} is the molar mass of NH_4Cl:

$$n = 3 \cdot \frac{m}{M_{NH_4Cl}} = 3 \cdot \frac{0.017\ \mathrm{g}}{53.5\ \mathrm{g/mole}} = 9.53 \cdot 10^{-4}\mathrm{mole} \qquad \text{A. 15}$$

At the temperature 1163K, at which the first transport experiment of ZnO and ZnS took place, and with a gas constant of *R* = 82.057 cm^3 atm/mol K, the pressure in the middle of the ampoule should according to Equation A. 13 be:

$$P = \frac{9.53 \cdot 10^{-4}\mathrm{mole}\ \cdot 82.057 \frac{\mathrm{cm^3 atm}}{\mathrm{mole\ K}} \cdot 1163\ \mathrm{K}}{26.5\ \mathrm{cm^3}} = 3.43\ \mathrm{atm.}$$

The second transport experiment of ZnO was done with at a middle temperature of 1218 K, which results in a pressure of 3.59 atm. The HSC diagrams were calculated for a pressure of 3.5 atm., as small changes in pressure showed no significant effect on the resulting diagrams at these temperatures.

Appendix III

Thermodynamic Data used by HSC Chemistry

	Molar Mass (g/mol)	ΔH (kcal/mol)	S (cal/mol K)
ZnO (s)	81.379	-83.762	10.430
ZnS (s)	97.440	-48.200	13.800
NH_4Cl (s)	53.491	-75.180	22.700
$ZnCl_2$ (g)	136.286	-63.500	66.126
NH_3 (g)	17.030	-10.0980	46.075
HCl (g)	36.461	-22.063	44.669
H_2O (g)	18.015	-68.315	16.718
H_2S	34.076	-4.900	49.176
Zn (g)	65.380	31.170	38.467

Appendix IV

Derivation of Mass Transport in Chemical Transport Reactions (*17*)

While diffusion is not the only means of transport, an estimate of the amount of transported material may be found by considering the transport to rely on diffusion only. The pressure in a sealed ampoule may be considered to be constant as the molecules in the ampoule will be distributed in such a way in order to keep the average pressure as low as possible. If the feed material is kept at one end of the ampoule, the total flux of this species will be directed to the other end of the ampoule as the concentration of the feed material will be lower there.

H. Schäfer derived an expression for the material transported by diffusion by considering an ampoule as shown in Figure 77.

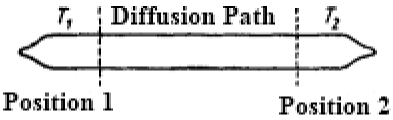

Figure 77: A sealed ampoule with two compartments separated by a diffusion path. The equilibrium of the given reaction should be different in Position 1 and Position 2.

The equilibrium positions of the reaction:

$$i\,A(s) + \,k(B)g \,\leftrightarrow j\,C(g), \qquad \text{A. 16}$$

must be different in Position 1 and 2. At any place in the ampoule, the total pressure P should be the same. This has the consequence that a reaction with a change in mole numbers in the gas phases ($i \neq j$), must have a net gas flow from one position to the other. The gas flow is a function of diffusion.

In order to understand the following derivation, the symbols in Table A.1 need to be explained.

Table A.1: Explanation of Symbols in Eq.	
$\boldsymbol{n_A, n_c}$	Number of moles of A or C that diffuse or flow through a cross section *q* during a time *t*
i,j	Coefficients in the reaction (Eq. 29)
$\boldsymbol{C_A, C_C}$	Concentrations of A and C in mole/cm^3
D	Diffusion coefficient in cm^2/sec for the gas mixture of A+C
$\boldsymbol{\Delta P_C}$	Change in partial pressure of species C (atm)
$\boldsymbol{\sum P}$	Total pressure in the ampoule (atm)
T	Average temperature in the ampoule in K
w	Linear gas flow velocity in cm/sec
q	Cross section of the ampoule in cm^2
t	Duration of the transport reaction in seconds
s	Diffusion path in cm
R	The universal gas constant

Under the previously stated conditions, the following applies:

$$-n_A : n_C = i : j; \quad n_C = -\frac{j}{i} n_A, \tag{A. 17}$$

$$\frac{dC_c}{ds} = -\frac{dC_A}{ds}, \tag{A. 18}$$

$$n_A = -Dqt\frac{dC_A}{ds} + qC_A wt, \tag{A. 19}$$

$$n_C = -Dqt\frac{dC_C}{ds} + qC_C wt. \qquad \text{A. 20}$$

By solving Equation A. 19 and A. 20 with respect to *w* and equating them, in addition to use Equation A. 17 and A. 18, the following expression is obtained:

$$n_A\left(\frac{1}{C_A} + \frac{j}{iC_C}\right) = -Dqt\frac{dC_A}{ds}\left(\frac{1}{C_A} + \frac{1}{C_C}\right), \qquad \text{A. 21}$$

$$n_A = -Dqt\frac{dC_A}{ds} \cdot \left[\frac{i(C_A + C_C)}{jC_A + kC_C}\right], \qquad \text{A. 22}$$

$$n_C = -Dqt\frac{dC_C}{ds} \cdot \left[\frac{j(C_A + C_C)}{jC_A + kC_C}\right]. \qquad \text{A. 23}$$

From Equation A. 19 and A. 22, the following expression may also be obtained:

$$w = \frac{1}{C_A} D \frac{dC_A}{ds}\left(1 - \frac{i(C_A + C_C)}{jC_A + kC_C}\right). \qquad \text{A. 24}$$

The expression in [ ] brackets in Equation A. 21 and A. 22 takes into account the gas flow resulting from a reaction with a change in mole numbers ($i \neq j$). For a reaction with no change in mole numbers (i = j), the expression equals 1. By changing the expressions from being dependant on concentrations to partial pressures, the following is obtained:

$$n_A = -\frac{Dqt}{sRT}\,\Delta P_A \cdot 10^{-3}\ (\text{mole}), \qquad \text{A. 25}$$

where the diffusion coefficient is given by:

$$D = D_0 \frac{\sum P_0}{\sum P}\left(\frac{T}{T_0}\right)^m. \qquad \text{A. 26}$$

$\sum P_0$ and T_0 are the conditions for which D_0 is known, typically ambient conditions. The exponent *m* is empirically found to be 1.8. Equation A. 25 may thus be reduced to:

$$n_A = \frac{i}{j}\frac{\sum P_0\,\Delta P_A}{\sum P}\frac{T^{0.8} D_0 qt}{sRT_0^{\,1.8}} \cdot 10^{-3}(\text{mole}) \qquad \text{A. 27}$$

Calculation of Mass Transport during CVT of ZnO and ZnS

For the transport experiments in this work, the change in partial pressure for $ZnCl_2$ is calculated to be 0.01 atm during the transport of ZnO, and 0.03 atm during the transport of ZnS as can be extracted from Figure 15 and Figure 16. In the case of ZnO, Figure 14 shows that the gradient of pure Zn opposed to $ZnCl_2$ is much higher, and the transport of both species need to be considered. The diffusion coefficient, D_0, for unknown systems is typically set to 0.1 cm^2/s, however for hydrogen containing systems, the diffusion coefficient is typically set to be 0.5-0.7 cm^2/s and consequently the selected diffusion coefficient is set to 0.6 cm^2/s for all the transport experiments. Given an average temperature of T = 1218 K in the ampoule, a cross-section of q = 1.77 cm^2, a diffusion path of $s \approx 15$ cm and a transport duration of 23 days. Using Equation A. 27 and considering the reaction:

$$ZnO(s) + 2HCl(g) \leftrightarrow ZnCl_2(g) + H_2O(g), \tag{A. 28}$$

where the coefficients of the reaction i and j are both equal 1, the mass of ZnO being transported via $ZnCl_2$ is estimated to be:

$$\begin{aligned} n_{ZnO} &= \frac{1}{1}\frac{1\ \mathrm{atm}\ \cdot 0.01\ \mathrm{atm}}{3.59\ \mathrm{atm}}\frac{\cdot\ 1218^{0.8}\ K \cdot\ 0.6\frac{\mathrm{cm}^2}{\mathrm{s}} \cdot 1.77\ \mathrm{cm}^2 \cdot 2 \cdot 10^6\mathrm{s}}{15\ \mathrm{cm} \cdot\ 82.057\frac{\mathrm{cm}^3\mathrm{atm}}{\mathrm{mole\ K}} \cdot 298^{1.8}\ \mathrm{K}} \cdot 10^{-3}\mathrm{mole} \\ &= 5.8 \cdot 10^{-4}\ \mathrm{mole} \end{aligned}$$

This corresponds to a transport of 0.05 g of ZnO being transported with $ZnCl_2$ as transport agent. The activity of elementary increases as the activity of $ZnCl_2$ decreases and the change in the temperature interval is similar. A similar calculation with H_2 acting as transport agent consequently also yields 0.05 g.

For ZnS the calculation results in a transport yield of 0.26 g, with $ZnCl_2$ as the only transport agent.

Appendix V

Diffraction – Theory and Derivations

The following is based on a handout on diffraction by Hugh Banks (*89*).

X-rays are electromagnetic waves and are characterized by their wavelength λ. The direction the wave propagates in is called the ***k*** direction and is perpendicular to both the oscillating electric field ***E*** and magnetic field ***H***. If the electric field oscillates in the *x* direction, while the magnetic field oscillates in the *y* direction, the *wavevector* ***k*** will point in the *z* direction (Figure 78).

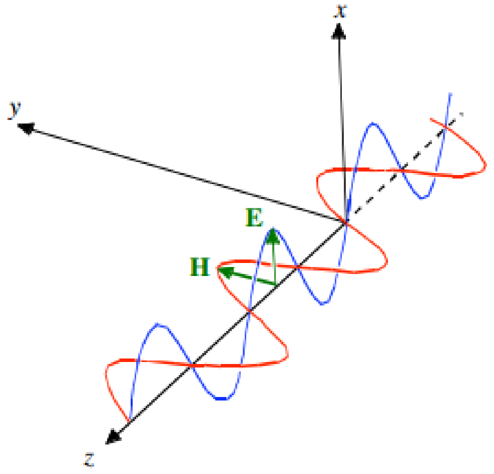

Figure 78: An electromagnetic wave traveling in the *z* direction. The direction a wave propagates in is generally denoted as the ***k*** direction, which in this case is the *z* direction (*89*).

The magnitude of the wavevector, $|\mathbf{k}| = k$, is related to the wavelength, λ, by the relation $k = 1/\lambda$. When an X-ray with wavevector ***k*** is elastically scattered by an atom, it will have the same wavelength, but the direction will be different and the wavevector is consequently denoted ***k'***. The scattered photon is emitted as a spherical wave, with an amplitude that decreases as the diffraction angle, denoted as 2θ, is increased. The intensity of the diffracted photons scale with the number of electrons around the atom or ion at which they are scattered and falls off with the scattering angle in a characteristic manner as a function of wavelength. If there is no angle dependence, the scattered X-rays would propagate outwards like a circular wave in a pond as shown to the left in Figure 79. If the angle dependence is included, there will be stronger scattering in the forward direction and would in two dimensions be analogous to the image on the right in Figure 79.

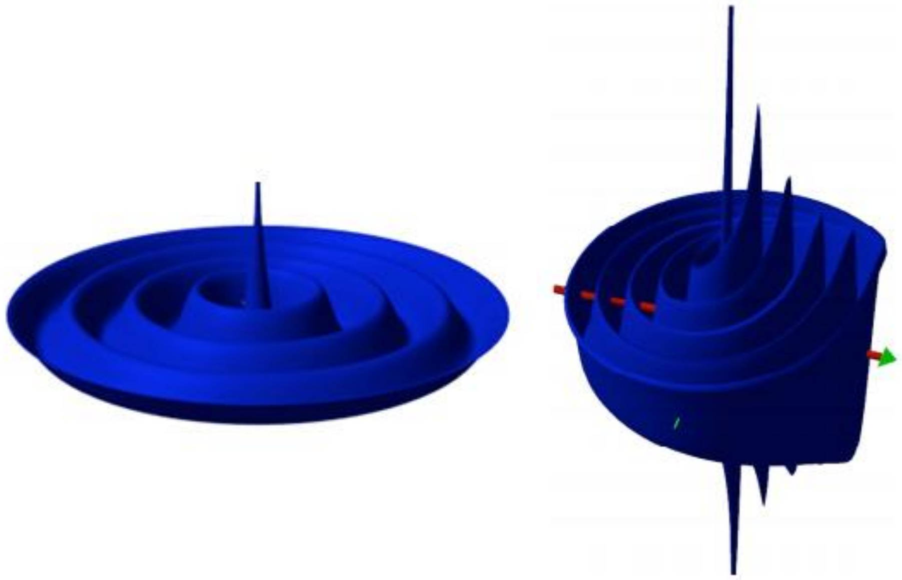

Figure 79: The left image shows how scattered X-rays propagate if there is no angle dependence, while the right shows how a 2θ dependence of the atomic scattering represented in two dimensions. The arrow represents the X-ray propagation directions (*89*).

It is the interference effects that occur when X-rays are scattered by a periodic lattice that are used in order to determine a structure by X-ray diffraction. By considering two atoms or ions separated by a distance, *d*, and a wave with wavevector, ***k***, which is scattered with a scattering wavevector, ***k’***, the intensity of the scattering vector may be found by considering the diagram in Figure 80.

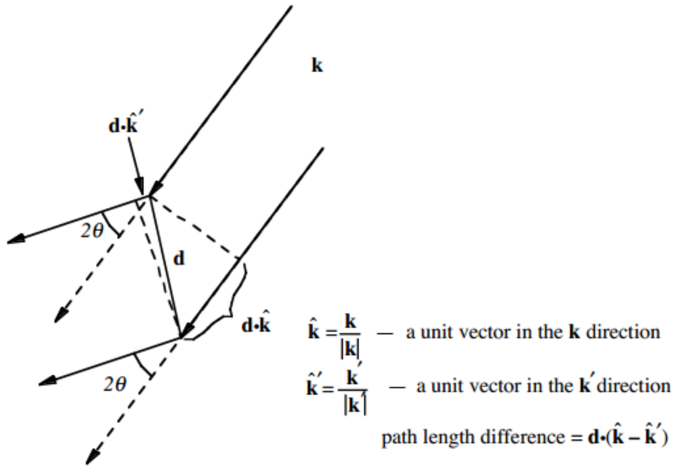

Figure 80: Diagram of a wave being diffracted by two atoms at a distance *d* from each other.

An expression for the amplitude of the scattered waves is $f_1(2\theta) + f_2(2\theta) \times$ (*phase shift factor*), where $f_1(2\theta) + f_2(2\theta)$ are the scattering amplitudes of atom 1 and 2 , respectively and are also called *atomic form factors* and depend on the electron density around each atom. The *phase shift factor* depends on the path length difference of the two scattered waves, given by $\boldsymbol{d} \cdot (\widehat{\boldsymbol{k}} - \widehat{\boldsymbol{k}}')$. In order for the two waves to constructively interfere with each other, the path length difference needs to be an integral multiple of wavelengths, i.e.

$$\boldsymbol{d} \cdot \left(\widehat{\boldsymbol{k}} - \widehat{\boldsymbol{k}}'\right) = n\boldsymbol{\lambda} \text{ where } n = 1,2,3, \ldots$$

$$\text{or } \boldsymbol{d} \cdot (\boldsymbol{k} - \boldsymbol{k}') = n \text{ since } k = \frac{1}{\lambda} \tag{A. 29}$$

The amplitude, $A(2\theta)$ can thus be written as:

$$A(2\theta) \propto f_1(2\theta) + f_2(2\theta) \times e^{(2\pi i(\widehat{\boldsymbol{k}} - \widehat{\boldsymbol{k}}') \cdot \boldsymbol{d})} =$$

$$f_1(2\theta) + f_2(2\theta) \times \begin{Bmatrix} 1 \text{ when } (\widehat{\boldsymbol{k}} - \widehat{\boldsymbol{k}}') \cdot \boldsymbol{d} = n \\ -1 \text{ when } \left(\widehat{\boldsymbol{k}} - \widehat{\boldsymbol{k}}'\right) \cdot \boldsymbol{d} = n + \frac{1}{2} \end{Bmatrix} \tag{A. 30}$$

The intensity is given by $I(2\theta) = |A(2\theta)|^2$. It should be noted that there can be no constructive interference if λ is larger than d, and λ should be of the same order or lower to get significant interference. This is the reason why X-rays are commonly used to for characterization of crystals, although thermal neutrons or high energy electrons also have suitable wavelengths and can be used to obtain complimentary data.

By using the translational symmetry of a crystal it is possible to generalize the results. As the position of every atom in a perfect crystal is related to an equivalent atom in another unit cell via translation by a lattice vector $\boldsymbol{R} = u\boldsymbol{a} + v\boldsymbol{b} + w\boldsymbol{c}$, where $\boldsymbol{a}$, $\boldsymbol{b}$, and $\boldsymbol{c}$ are the primitive vectors of the crystal lattice, while u, v and w are integers, it is possible to specify a condition in which all of a set of a crystal's equivalent atoms will scatter X-rays with constructive interference.

$$\boldsymbol{R} \cdot (\boldsymbol{k} - \boldsymbol{k}') = n \text{ for all lattice vectors } \boldsymbol{R}$$

$$\text{or } e^{2\pi i(\boldsymbol{k} - \boldsymbol{k}')\boldsymbol{R}} = 1 \tag{A. 31}$$

The implications of this is that the vectors ***k* - *k'*** simply are the *reciprocal lattice vectors*. The condition for constructive interference in a crystal is thus that an X-ray must be scattered by a reciprocal lattice vector $\boldsymbol{G}_{hkl}$:

$$\boldsymbol{k} = \boldsymbol{k}' + \boldsymbol{G}_{hkl}. \qquad \text{A. 32}$$

This is the Laue diffraction condition. The reciprocal lattice vector is constructed from the reciprocal axis vectors $\boldsymbol{a}^*$, $\boldsymbol{b}^*$ and $\boldsymbol{c}^*$:

$$\boldsymbol{a}^* = \frac{\boldsymbol{b}\times\boldsymbol{c}}{\boldsymbol{a}(\boldsymbol{b}\times\boldsymbol{c})}; \qquad \boldsymbol{b}^* = \frac{\boldsymbol{a}\times\boldsymbol{c}}{\boldsymbol{a}(\boldsymbol{b}\times\boldsymbol{c})}; \qquad \boldsymbol{c}^* = \frac{\boldsymbol{a}\times\boldsymbol{b}}{\boldsymbol{a}(\boldsymbol{b}\times\boldsymbol{c})}. \qquad \text{A. 33}$$

The reciprocal lattice vector $\boldsymbol{G}_{hkl}$ can then be constructed:

$$\boldsymbol{G}_{hkl} = h\boldsymbol{a}^* + k\boldsymbol{b}^* + l\boldsymbol{c}^*, \qquad \text{A. 34}$$

where *h, k* and *l* are integers. The definition of the reciprocal axis vectors guarantee that the dot product between any direct lattice vector ***R*** and any reciprocal lattice vector $\boldsymbol{G}_{hkl}$, will be an integer. Using geometry it can be shown that the distance between planes d_{hkl} is given by:

$$d_{hkl} = \frac{1}{|\boldsymbol{G}_{hkl}|} \qquad \text{A. 35}$$

As the magnitudes *k* and *k'*are equal, **Error! Reference source not found.** may be squared, i. e. $k^2 = (\boldsymbol{k} + \boldsymbol{G}_{hkl})^2$ and rewritten as:

$$2\boldsymbol{k}\cdot\boldsymbol{G}_{hkl} = G_{hkl}^2. \qquad \text{A. 36}$$

By using A. 35, and that $\boldsymbol{k}\cdot\boldsymbol{G}_{hkl} = kG_{hkl}\sin\theta$, Equation A. 36 may be written as:

$$2\left(\frac{1}{\lambda}\right)\sin\theta = \frac{1}{d_{hkl}}, \qquad \text{A. 37}$$

The integers, *hkl*, that define $\boldsymbol{G}_{hkl}$ are not neccesarily the same as the indices of the crystal plane, as they can share a common factor as long as $\boldsymbol{G}_{hkl}$ is an arbitary reciprocal lattice vector. Actual *hkl* crystal planes are defined as the reciprocal of where they intercept the axes and then multiplied with the smallest common factor, which has the consequence that the common factor *n* is eliminated. Equation A. 37 may thus be written as:

$$2d\sin\theta = n\lambda, \tag{A. 38}$$

where d is the spacing between adjacent parallel planes with indices *h/n, k/n, l/n.* This is the well known Bragg's Law.

Most structures have more than one atom per unit cell, and for a crystal with N atoms in the unit cell, the scattering amplitude, which in this case is called the *geometric structure factor*, can be found by using $\mathbf{G}_{hkl}$, and Equation A. 30:

$$F_{hkl} \propto \sum_{j}^{N} f_j(2\theta) \times e^{(2\pi i \boldsymbol{G}_{hkl}\cdot \boldsymbol{d}_j)}, \tag{A. 39}$$

where $f_j(2\theta)$ is the form factor of the j^{th} atom and $\boldsymbol{d}_j$ specifies the position of the j^{th} atom.

A useful geomtric construction, called the *Ewald sphere* (Figure 81), can be made in order to understand how a crystal must be oriented in order for the diffraction condition, A. 32 or A. 38, to be satisified. The sphere is constructed by scaling k relative to the reciprocal lattice dimensions and positioning the origin of $\boldsymbol{k}$ on the origin of the reciprocal lattice. A sphere is constructed around the tip of the $\boldsymbol{k}$ vector, which guarantess that the origin lies on the sphere's surface. Only reflections lying on the sphere satisfy the diffraction condition for constructive interference and will be possible to detect. By rotating the crystal relative the the incoming beam, different reflections will be rotated in and out of the sphere and by scanning over a wide range of incident angles it is thus possible to obtain all the allowed reflections for the desired crystal.

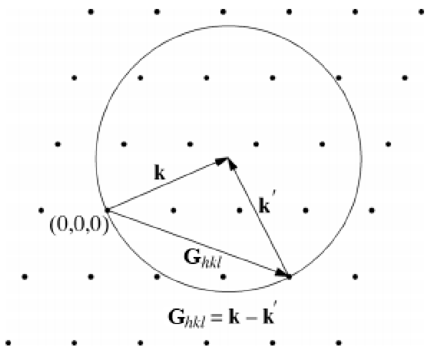

Figure 81: The *Ewald sphere*. By creating a sphere with radius k and positioning the origin of the vector $\boldsymbol{k}$ so its tip is in the center of the sphere, it is possible to see when the diffraction conditions are fulfilled. The points are reflections of reciprocal lattice points of the crystal. Only reflections that lie on the sphere satisfy the condition (*89*).